AN INVESTIGATION OF THE GEOLOGY, GEOCHEMISTRY, AND TIMING OF GOLD MINERALIZATION AT THE VIKING GOLD DEPOSIT, WHITE BAY, NEWFOUNDLAND

MATTHEW MINNETT

An Investigation of the Geology, Geochemistry, and Timing of Gold Mineralization at the Viking Gold Deposit, White Bay, Newfoundland

By
© Matthew Minnett, B.Sc. (Hons)

A Thesis submitted to the School of Graduate Studies
in partial fulfillment of the requirements for the degree of
Master of Science

Department of Earth Sciences
Memorial University of Newfoundland

October, 2012

St. John's Newfoundland

ABSTRACT

Silurian-Devonian orogenic gold deposits in Newfoundland are typically situated proximal to major regional scale structural lineaments. Such deposits are formed in accretionary settings, late in the orogenic process with nearby intrusions of similar age, by low-salinity, H_2O-CO_2 ± CH_4 fluids at temperatures ranging from 250-350°C. The White Bay area of western Newfoundland contains at least 3 styles of mineralization including structurally controlled orogenic gold–base-metal mineralization (Type 1), stratabound galena mineralization (Type 2), and minor fluorite and molybdenite occurrences (Type 3). These deposits are proximal to the Doucer's Valley fault system, an interpreted Taconic thrust surface which offsets Carboniferous strata. This fault system may have been episodically active for *ca.* 150 m.y. providing conduits for mineralizing hydrothermal fluids on a regional scale.

The Viking gold property, located 10 kilometers south of the community of Pollards Point, contains Type 1 orogenic-style gold mineralization west of the Doucer's Valley fault system in the Humber Zone. High-grade mineralization consists of coarse (50 to >140 micron) blebby gold and argentiferous electrum hosted both within quartz veinlets and as inclusions in the sulfide assemblage (pyrite, galena, sphalerite, and chalcopyrite) of these veinlets. Lithogeochemistry and previous U-Pb geochronology demonstrate that the hosts to this mineralization/alteration are *ca.* 1030 Ma, Grenvillian A-type anorogenic granitoids, *ca.* 615 Ma continental tholeiitic dykes and inclined sheets of the Long Range dyke swarm and calc-alkaline lamprophyric dykes of unknown affiliation. ^{40}Ar-^{39}Ar thermochronology on late-syn-kinematic biotite porphyroblasts constrains the age of the last peak (*ca.* 250° C) metamorphism to the latest Silurian at *ca.* 419 Ma. Hydrothermal sericite from the alteration assemblage yields plateau and pseudo-plateau ages ranging from 409 ± 12 Ma to 377 ± 1.5 Ma. Fluid inclusion assemblages have homogenization temperatures that range from 240-320°C and are low salinity. Sulfur isotope results indicate that $\delta^{34}S$ values are heavier than sulfur from magmatic origins and Pb model ages suggest that Pb was scavenged from multiple sources. These observations collectively suggest that the Viking gold mineralization represents a unique silver-bearing, granite-hosted, orogenic gold deposit in the Humber Zone formed in the Lower Devonian after orogenic collapse, from auriferous fluids fluxed along the Doucer's Valley fault system.

ACKNOWLEDGMENTS

Many individuals require acknowledgement for their contributions and guidance throughout the course of this project. Dr. Hamish Sandeman is much obliged for providing this project and for having copious patience and understanding. His direction and often in-depth conversations sparked geological curiosities unbeknown to me. Dr. Derek Wilton is thanked for being co-supervisor along with Dr. Sandeman and for providing encouraging words of wisdom for keeping me on track. Dr. Steve Piercey is thanked for taking on the role of committee member for this project and for "keeping it real." Sharing a neighbouring office with Dr. Piercey is an experience which comes highly recommended for any graduate student who needs someone that tells it how it is.

This study would not have been possible without financial and technical support from the Geological Survey Branch of the Department of Natural Resources, Government of Newfoundland and Labrador. Funding was also provided through an NSERC grant to Dr. Wilton and from the School of Graduate Studies Fellowship, MUN. Dr. Shane Ebert, President of Northern Abitibi Mining Corporation, is thanked for access to company data and for the employment opportunity at the Viking Property during the summers of 2009 and 2010.

D. Archibald at Queen's University is thanked for acquisition of ^{40}Ar-^{39}Ar thermochronological data used in this study. Dr. Graham Layne and Dr. Glenn Piercey are thanked for assistance with collecting stable and radiogenic isotope data. Appreciation goes to Dr. James Conliffe for help with setting up and collecting fluid inclusion data. A big thanks to Pam King who allowed "free rein" access to labs necessary to prepare samples and for answering any and all questions related to lab equipment.

Fellow graduate students D. Courage, C. McKinley, S. Brueckner, S. Lode, N. Szponar, M. Johnston, H. Mills, M. Hindmith, T. Miller, C. Boyd, J. Glasgow, A. Ritze, A. Chafe, A. Buchanan, P. Nyade, and M. Kelvin made graduate life more than enjoyable and are thanked for all of the good times.

I would like to thank my family for their constant support, guidance and love throughout the years.

Finally, I would like to thank Mary Leaman for her love, patience, support, encouragement and understanding throughout the course of this project.

TABLE OF CONTENTS

LIST OF FIGURES

LIST OF TABLES

LIST OF PLATES

CHAPTER 1

INTRODUCTION

1.1 INTRODUCTION

Orogenic gold deposits constitute an important class of mineral resource and have been the subject of enduring scientific interest for the past 30 years. The characteristics of orogenic gold deposits have been summarized by a number of authors including Groves *et. al.* (1998), Goldfarb *et. al.* (2005), Groves *et. al.* (2003), and references therein. The gold mineralization at the Viking deposit is interpreted to belong to this deposit type.

The Viking deposit is located within a block of 36 claims known as the Viking Property. The Viking Property is located 50 km northeast of Deer Lake and 12 km west of White Bay on NTS map sheet 12/H/10-11 situated along the eastern margin of the Great Northern Peninsula in western Newfoundland (Figure 1.1). Access to the property is provided by logging roads that link to Newfoundland provincial highway 420. The dominant physiographic features of the area include rugged topography with a total relief of over 500 m, coupled with extensive, thick forest cover.

Mineralization at the Viking deposit (see Section 2.4) is hosted within quartz-sulfide veins, with varying amounts of calcite. Quartz-sulfide veins, which range in width from millimeter to meter scale, occur in complex networks, are locally folded and steeply dipping, and are associated with brittle-ductile shear zones (e.g. Thor trend). The best example of high-grade gold mineralization is the Thor vein that has assayed up to 218 g/t Au over 0.5 m with lower-grade intercepts of 8.7 g/t Au over 1.3 m (Ebert, 2008-2011).

This chapter summarizes the previous geological investigations and the exploration history proximal to the Viking deposit, the regional geological setting, the purpose and scope of this study and the analytical methods used herein. Its location to the west of the Doucer's Valley fault system in older basement rocks makes it unique with respect to gold deposits in the Humber Zone. Classification of the Viking deposit gold mineralization will help place it into a regional, temporal context with other examples of gold mineralization in the White Bay area, in other parts of Newfoundland and elsewhere in the Appalachian Orogen.

1.2 PREVIOUS INVESTIGATIONS

The geology of the western White Bay area has been studied for more than a century with the first geological investigations conducted by Alexander Murray (1881). The first attempt at gold mining on the island of Newfoundland is documented to have begun in 1903 at the Browning Mine, 5 km to the northeast of the Viking deposit (Snelgrove, 1935). Previous gold production from the island was restricted to the by-products of copper ore mining prior to this date (e.g. Tilt Cove Mine, Notre Dame Bay; Snelgrove, 1935). Before 1933, all of the known gold showings in White Bay were situated proximal to Sops Arm were studied by Snelgrove (1935), Heyl (1937), and Betz (1948).

The gold mineralization near Sops Arm has been the focus of a number of more recent studies including Tuach (1987) and Kerr (2006a). gold mineralization was discovered by prospector Clyde Childs in 1983 within the Late Grenvillian Apsy Granite (informally known as the French-Childs granodiorite) of the Jackson's Arm area (Tuach

and French, 1986). This was the first "significant" gold prospect located within the Grenvillian rocks of Newfoundland and Labrador and was studied by Tuach and French (1986), Saunders and Tuach (1988), and Kerr and van Breemen (2007).

Saunders (1991) completed a detailed compilation of the western White Bay area documenting three broad styles of mineralization and noted the close spatial relationship with the Doucer's Valley Fault System (DVFS). The DVFS and its secondary structures may have acted as conduits allowing large-scale, deep-seated, circulation of hydrothermal fluids on a regional scale implying the possibility that gold mineralization may have formed during a single widespread mineralizing event (Saunders, 1991).

The Geological Survey of Newfoundland and Labrador (GSNL) conducted numerous regional mapping projects in the area. Smyth and Schillereff (1982) published 1:25 000 scale maps and summarized the regional geology. A 1:250 000 scale geological map, compiled by Owen (1991), concentrated on rocks of the Long Range Inlier. The stratigraphy and structure of the Cambrian and Ordovician rocks in the Coney Arm and Jackson's Arm areas was documented by Kerr and Knight (2004). The geochemical and metallogenic characteristics of the Devonian Gull Lake Intrusive Suite (GLIS), and related Devils Room Granite (DRG), were studied by Saunders and Smyth (1990). These authors concluded that both the GLIS and the DRG have low potential for significant granophile mineralization. The GLIS, which is inferred to be cogenetic with the Sops Arm Group, was suggested as a priority exploration target for gold by Saunders and Smyth (1990).

1.3 EXPLORATION HISTORY OF THE VIKING PROPERTY

Prior to 1987, there is no record of industry-supported mineral exploration in the area of the Viking deposit. The property consisted of 36 claims under three license numbers (12734M, 010935M, and 08878M) that were amalgamated to form license 014079M through the changing of property ownership. The following summary of the exploration activity in the area is modified from Churchill and Voordouw (2006)

Noranda Exploration Company Limited (Noranda) staked two claim blocks in 1986 that were immediately adjacent to BP Resources Canada Limited (BP) claims. The Noranda claims eventually became known as the "Viking Property" named after the gold showing discovered therein. Noranda's 1987 work program included a total of 220 km of reconnaissance grid work comprising prospecting, mapping, soil sampling, and mag/VLF-EM surveys carried out under contract by Shear Exploration Limited. The result of this work identified a series of high priority gold anomalies that are now known as the "Viking Trend". This is a 6.5 km long zone with widths of up to 100 m that follows a prominent northeast-trending topographic linear. Grab samples along the trend returned values of 5.15 grams per tonne (g/t) Au, 21 g/t Ag, 0.74% Pb, and 0.62% Zn. Soil sampling identified several target areas with values of greater than 1000 ppb Au.

In 1988, a series of detailed follow-up surveys were completed by Noranda. A grid totalling 46.4km in length with a four kilometer baseline was cut along the trend of the main gold anomaly. B-horizon soil samples collected from this grid defined four separate Gold anomalies. Lake-bottom sampling proved more successful and resulted in a maximum assay value of 55 ppb Au. Diamond-drilling was completed during 1989 and returned 0.56 g/t Au over 5.3 m within variably altered granite. Results from outcrop,

float, and inferred subcrop sampling yielded a maximum of 6.95 g/t Au. A total of 218 B-horizon soil samples were collected yielding a maximum of 500 ppb Au. In 1990, another series of sampling surveys returned less than expected results and a recommendation for no further work on these claims was made.

BP Resources Canada Ltd. (BP) completed exploration work in the area during the same period as Noranda. A line cutting and soil sampling program in 1987 in the area directly west of White Bottom Pond yielded a broad gold-in-soil anomaly. In 1988, BP undertook a soil sampling program, along with grid mapping and prospecting, and 267 samples were collected that coincided with a helicopter-borne magnetic and VLF-EM survey. The results of these efforts included the definitions of a 200 by 500 m gold-in-soil anomaly with elevated Pb–Mo concentrations.

Deep Reach Exploration Inc. (DREX) staked portions of the north-eastern part of the Viking Trend in 2002. These were subsequently optioned to Messina Minerals in 2002 who surveyed and collected 24 samples on the northeast end of the Viking grid. Assay results from this survey included values of up to 18.4 g/t Au in stockwork veined, argillic-altered granite. Messina returned one of the three licenses to DREX and subsequently acquired an additional 16 claims before optioning the current Viking Property to Altius Resources Inc. in 2006. Northern Abitibi Mining Corporation (NAMINCO) entered into an option agreement with Altius Resources Inc. in July 2007 to acquire an interest in the Viking Property. NAMINCO, through 2007 to 2012, has completed trenching, diamond drilling, and systematic assay sampling in order to delineate and define the economic potential of the Viking deposit. The property is currently under the ownership of Spruce Ridge Resources.

1.4 REGIONAL GEOLOGY

1.4.1 The Appalachian Orogen in Newfoundland

The Paleozoic Appalachian Orogen in Newfoundland records the effects of orogenesis associated with the protracted development and destruction of the Iapetus and Rheic Ocean (Williams, 1995a). Rocks of the Appalachian Orogen are divided into four broad temporal categories: early Paleozoic and older, middle Paleozoic, late Paleozoic, and Mesozoic (Williams, 1979). Figure 2.1A illustrates Williams (1979) zonal divisions for the lower Paleozoic and older rocks (from west to east): the Humber, Dunnage, Gander, and Avalon zones (Williams, 1979). The Viking deposit is located within the Humber Zone of the Appalachian Orogen. The Humber Zone is separated into external and internal parts based on structural and metamorphic styles. The western margin of the Humber Zone is defined as the limit of Appalachian deformation (*i.e.*, the Appalachian Structural Front) and the eastern margin is delineated at the Baie Verte–Brompton Line (Williams, 1995b). The structural style of the Humber Zone is that of a foreland fold-and-thrust belt, with more deformed and metamorphosed rocks of the internal Humber Zone thrust over the largely undeformed rocks of the external Humber Zone (Williams, 1995a)

1.4.2 Regional Geology of Southern White Bay

The Humber Zone represents the ancient margin of Laurentia that has been extensively reworked during Appalachian orogenesis (Williams, 1979). The Long Range Inlier (LRI) is the largest exposure of basement rocks in western Newfoundland (Heaman, *et al.*, 2002) and consists of mid-Proterozoic Grenvillian rocks (Owen and Erdmer, 1988). Rocks of the inlier comprise a series of *ca.* 1500 Ma granitoid gneisses

that have been intruded by granitoid plutons at *ca.* 1025 and *ca.* 1000 Ma (Heaman *et al.*, 2002). These granitoid plutons preserve three distinct metamorphic events, the latter two of which correspond to the two intervals of magmatism (Heaman *et al.*, 2002). All rocks of the inlier are crosscut by the late Precambrian (~615 Ma) Long Range Dykes (Kamo, *et al.*, 1989) that are interpreted to have formed in response to uplift and rifting of the LRI (Hinchey and Knight, 2011). The eastern margin of the inlier was intruded by the Silurian Devils Room Granite (425 ± 10 Ma), and also by the Silurian Taylors Brook gabbro complex (430.5 ± 2.5 Ma; Heaman *et al.*, 2002), causing contact metamorphism of the adjacent units.

Immediately east of the Long Range Inlier is a deformed, autochthonous, Cambrian to Ordovician shelf sequence composed of the Labrador, Port au Port, and the St. George groups (Kerr and Knight, 2004). The Bradore and Forteau formations comprise the lower Cambrian rocks of the Labrador Group and are dominated by sandstone, quartzite, and phyllite, with thin lenses of dark limestone, dolostones and siltstone. These rocks are east-dipping and exhibit tight, isoclinal folding with both "S" and "Z" asymmetry. Conformably overlying the Forteau Formation is the Hawke Bay Formation, consisting of well preserved, mixed siliciclastic and carbonate rocks. The Port au Port and the St. George groups comprise late Middle Cambrian to early Middle Ordovician carbonate rocks that overly the Labrador Group (Kerr and Knight, 2004).

To the east of the DVFS is the Southern White Bay allochthon (Smyth and Schillereff, 1982). This Cambrian to Ordovician allochthon includes the Taylor's Pond Formation, Maiden Point Formation, Murray's Cove Schist, and the Coney Head Complex. The Taylor's Pond Formation is a narrow belt of dark coloured, graphitic and

pyritic slate and phyllite which is characterized by laminated limy argillite and abundant quartz veins and pods (Smyth and Schillereff, 1982). Fine- to medium-grained, green, schistose greywacke and slate make up the Maiden Point Formation which is overlain by the Murray's Cove Schist. The Murray's Cove Schist consists of polydeformed and metamorphosed mafic tuff and breccia with rare thin calcareous tuff, red chert and metagabbro pods. These rocks are locally intruded by pre-tectonic grey feldspar porphyritic felsic dykes (Smyth and Schillereff, 1982). Lastly, the Coney Head Complex is a dominantly trondhjemite and tonalite intrusive suite that also includes gabbro, biotite microgranite and minor muscovite leucogranite. This package is interpreted to structurally overly the autochthonous clastic carbonate rocks described above (Kerr and Knight, 2004) and represents vestiges of the Iapetus Ocean that were obducted westward across the ancient continental margin of North America during the Ordovician Taconian Orogeny (Williams and Stevens, 1974).

The eastern White Bay area is dominated by the Silurian Sops Arm Group. The western sequence comprises the Pollards Point, Jackson's Arm, and Frenchman's Cove formations. These consist of a lower package of felsic volcanic and pyroclastic rocks with lesser mafic volcanic rocks and conglomerates that are overlain by a fining-upward sequence of terrestrial to fluviatile sedimentary rocks (Kerr, 2006b). The eastern sequence is composed of the Simms Ridge and the Natlins Cove formations which are thought to be in stratigraphic continuity (Kerr, 2006b). The western and the eastern sequences are separated by the Long Steady Fault which is a reverse fault characterized by highly schistose zones (Kerr, 2006b). The present architecture of the Sops Arm Group mainly records Salinic and/or Acadian deformation of Silurian to Devonian age (Heyl, 1937;

Kerr, 2006b). These rocks host numerous Gold occurrences (*e.g.*, the Browning Mine) and stratabound lead mineralization in brecciated dolostones (Currie, 2004; Saunders, 1991).

1.5 AIM OF STUDY

The aim of this study is to provide a detailed examination of the geology, geochemistry, and timing of formation of gold mineralization at the Viking deposit. This will help to better understand the geological metallogenic context of the mineralization on a local and regional scale and to apply a genetic model for the type of gold mineralization. Data collected from field and experimental techniques will be compared to similar data from other gold showings in the White Bay area. The specific questions investigated in each chapter of this thesis are outlined below:

Chapter 2:

1. What are the host rocks to the gold mineralization observed at the Viking deposit and what are their lithogeochemical signatures?
2. What are the structural controls on mineralization from a regional and local perspective?
3. What alteration and ore minerals are associated with mineralized and barren quartz veins? What are their relationships and textures? What are the geochemical signatures of the gold mineralization
4. What is the timing of gold deposition at the Viking deposit and how does it fit with the timing of the formation of gold mineralization elsewhere in the White Bay area?

Chapter 3:

1. What are the characteristics of the fluid(s) responsible for precipitating gold mineralization at the Viking deposit? What were the pressure and temperature conditions at the site of both mineralized and barren veins?
2. Can a source for the sulfur within the sulfide assemblage be inferred? On a regional scale, are there different sulfur sources?
3. Can potential sources of metals be pinpointed from the Viking ores and how does it compare to sources of metals from similar deposits in the White Bay area?

1.6 METHODS

The initial stages of this project involved one month of planning and logistical work during May 2009, followed by three months of field work from June to August, 2009. Field mapping was primarily completed at the trench scale and included collection of samples for petrography, geochemistry, and geochronology. Field work completed during 2009 and 2010 resulted in the collection of 107 lithological samples. Detailed analytical methods are presented in (Appendix A). The above questions are addressed in each chapter using the following analytical methods:

Chapter 2:

1. Observation of host lithologies in drill core and outcrop were followed by petrographic study. Polished thin sections were prepared by S & T Lapidary Limited, St. John's, NL. The thin sections were viewed under a polarizing microscope and descriptions of mineral occurrences and textures were noted. Whole rock lithogeochemistry was completed on "fresh" and altered host rocks to elucidate

their geochemical signatures and to permit regional comparison with other granitoid plutons in the White Bay area (including the Devil's Room Granite, Apsy Granite and the Gull Lake Intrusive Suite).

2. Outcrop and trench mapping (1:200 scale) was conducted to map and observe stratigraphic and structural relationships between lithologies and mineralization.
3. A scanning electron microscope (SEM) was used to verify the presence and interrelationships of gold and other sulfides, provide essential information on textural relationships between ore and gangue minerals, and to identify any unknown minerals.
4. Argon-argon thermochronology on biotite and muscovite mineral separates was used to determine the timing of the formation of these minerals. It will be shown that a textural link exists between the alteration assemblage (quartz+pyrite+sericite) and gold. Dating of muscovite (i.e. the timing of the formation of the sericitic alteration halo) provides constraint on the timing of gold mineralization at the Viking deposit. Biotite provides the timing of metamorphism in the area.

Chapter 3:

1. Microthermometric fluid inclusion analyses on a Linkam THMSG600 were completed on selected quartz-sulfide veins, including both gold mineralized and barren veins, in order to determine the pressure and temperature regime of the formation for these veins.
2. *In-situ* sulfur isotope analysis using secondary ion mass spectroscopy (SIMS), of pyrite, chalcopyrite and galena were performed to characterize the sources of sulfur in the mineralizing fluid.

3. *In-situ* lead isotope analysis using SIMS of galena within mineralized veins was undertaken to identify potential Pb sources. Using ISOPLOT (Ludwig, 2003), model ages were calculated and compared to model ages of similar samples taken in the Silver Mountain area (Currie, 2004).

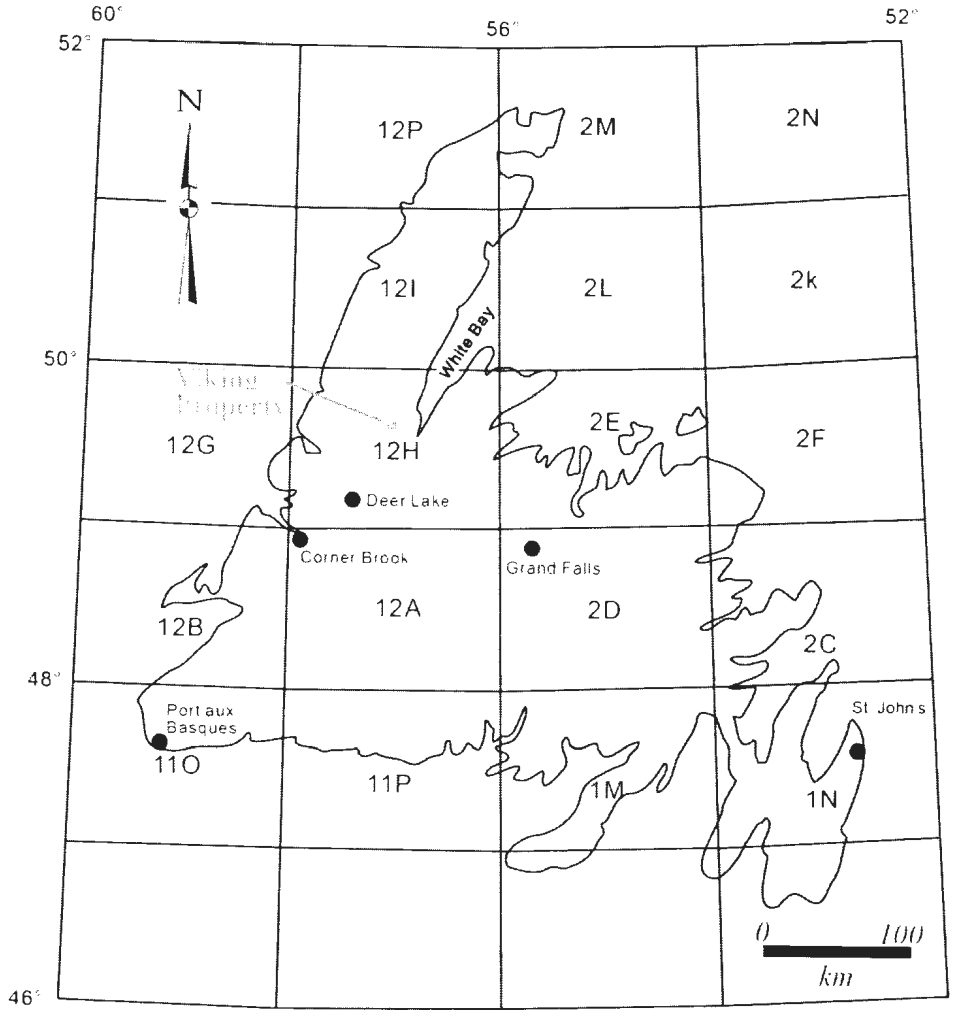

Figure 1.1: Location of the Viking Property along the eastern margin of the Northern Peninsula of the island of Newfoundland.

CHAPTER 2

GEOCHEMISTRY OF THE HOST ROCKS AND TIMING OF GOLD-ELECTRUM MINERALIZATION AT THE VIKING PROPERTY, NEWFOUNDLAND

2.1 INTRODUCTION

Gold mineralization at the Viking deposit in the White Bay area, western Newfoundland, has been recognized for over 20 years (Deering, 1989). Much of the exploration history of the property is summarized in Churchill and Voordouw (2006) and Minnett *et al.* (2010). Recent diamond drilling (Ebert, 2008-2011) has discovered the Thor trend gold occurrences hosted by the Main River Pluton (interpreted as a Grenvillian granitic pluton) situated at the eastern margin of the Long Range Inlier (Figure 2.1). The Thor trend contains the Thor vein, a 30- to 100-cm thick gold-bearing quartz-sulfide vein array that is the focus of this study.

Known gold mineralization in the greater White Bay area is hosted by potassic-altered Grenvillian granite and also occurs in younger Paleozoic cover rocks of the Sop's Arm Group (Kerr, 2006a, b). Saunders (1991) described three broad styles of mineralization in the White Bay region in close spatial relationship with the DVFS including: 1) structurally controlled orogenic gold–base-metal mineralization (Type 1); 2) stratabound galena mineralization (Type 2); and, 3) minor fluorite and molybdenite occurrences in the Gull Lake Intrusive Suite and Devil's Room Granite (Type 3). Because the DVFS is likely a Taconic thrust surface (Hinchey and Knight, 2011; Smyth and Schillereff, 1982) that also offsets Carboniferous strata, it may have been episodically active for over *ca.* 150 m.y. This relationship was interpreted by Tuach (1987) to indicate

that the fault system provided conduits for mineralizing hydrothermal fluids on a regional scale, likely over a protracted period of episodic fault movements. These conduits were responsible for precipitating structurally controlled orogenic gold–base-metal mineralization in the volcanic and sedimentary rocks of the Silurian Sop's Arm Group (e.g. Browning Mine and Unknown Brook; Currie, 2004; Kerr, 2006a), and in Neoproterozoic granitic rocks and structurally overlying Cambrian sedimentary rocks (e.g. Rattling Brook and Viking deposits; Kerr, 2005; Minnett *et al.*, 2010). Soil and assay sampling have been completed over the Viking deposit (French, 1987) that indicate gold-in-soil anomalies are coincident with fault zones.

Numerous Grenvillian granitic plutons intruded the LRI during two distinct intervals and their geochemistry and geochronology have been previously studied by Owen (1991) and Heaman *et al.* (2002), respectively. Until this study, whole-rock geochemical data were not available for the Main River Pluton.

Based on geochronological data a temporal range of gold deposition on the island of Newfoundland is defined. How the timing of the formation of the gold mineralization at the Viking deposit fits into this temporal range is unknown. The ^{40}Ar-^{39}Ar incremental step-heating analysis of pre- and post-mineralization dykes at the Rattling Brook gold deposit constrained the timing of mineralization to the interval *ca.* 415 to 409 Ma, during the latest Silurian or earliest Devonian (Kerr and van Breemen, 2007). Geochronological data on the timing of gold mineralization at the Viking deposit will help to facilitate correlation with regional, tectonic and igneous events.

This chapter aims to document the stratigraphic and structural controls on alteration and gold mineralization within the Thor trend, the geochemical characteristics

of the altered and fresh host rocks, and the timing of the formation of the alteration and by inference, associated gold deposition. This study was supported by an integrated drillcore logging and trench mapping program.

2.2 HOST ROCKS TO GOLD MINERALIZATION

The main host to the gold mineralization is a potassium feldspar megacrystic granodiorite that is cut by sheets of variably textured monzogranite. These granitic rocks are crosscut by meter scale mafic to intermediate diorite to amphibolite dykes interpreted to be part of the Long Range Dyke swarm. The Thor Vein is associated with fine-grained, sericite and carbonate altered, lamprophyre dykes. Both the Bradore and Forteau Formation are locally hydrothermally altered and mineralized adjacent to the Thor trend.

2.2.1 Potassium-Feldspar Megacrystic Granodiorite

Mineralization and alteration in the Thor trend are mainly developed in potassium-feldspar megacrystic to augen granodiorite (Plate 2.1) of the Main River Pluton. This porphyritic phase of the pluton has been correlated with the *ca.* 1036 Ma Apsy Granite to the north which hosts the Rattling Brook gold prospect (Kerr, 2005). The Main River Pluton granodiorites are characterized by fine-grained, typically chlorite-altered, biotite crystals that define a fabric surrounding medium- to coarse-grained orthoclase megacrysts (Plate 2.1). The potassium feldspar megacrysts often show internal strain fabric and matrix quartz typically exhibits sutured grain boundaries, consistent with them being deformed and metamorphosed to lower greenschist grade. Hydrothermal alteration associated with gold mineralization typically overprints both the megacrystic feldspars and matrix minerals with sericite, and can range in intensity from weak (10-15%

total replacement) to intense (80% total replacement; Plate 2.2). Pyrite and local trace amounts of chalcopyrite, galena, and fine-grained titanite are disseminated in the groundmass.

2.2.2 Monzogranite

The structural fabrics developed in the megacrystic granodiorite are locally crosscut by metre-scale sills of variably textured, massive to weakly foliated leucocratic monzogranite (Plate 2.3). The sheets of monzogranite are typically salmon-pink to beige coloured and are texturally heterogeneous. They range from fine-grained and moderately foliated (Plate 2.3) to massive and coarser-grained. This unit hosts fine- to medium-grained plagioclase and K-feldspar, and over 20% fine- to medium-grained anhedral quartz crystals commonly with sutured grain boundaries (Plate 2.4); microcline typically contains plagioclase exsolution lamellae. The feldspars are variably replaced by sericite in zones proximal to mineralized quartz veins. Biotite concentration ranges from approximately 10% to absent. Epidote is present in minor amounts and fractures contain limonite. Trace to 1% disseminated magnetite and pyrite are found throughout unit.

2.2.3 Metadykes

Dioritic to gabbroic dykes, with shallow to moderate dip, crosscut both the granodiorite and the monzogranite and locally host gold mineralization and alteration at its margins (Plate 2.5). It is therefore less significant as a host to gold mineralization compared to the granodiorite and monzogranite. These metamorphosed chloritic gabbroic rocks (termed metadykes in subsequent discussion) are typically massive, northeast-trending, and preserve moderately foliated, finer-grained chilled margins.

These mafic to intermediate intrusions are melanocratic, medium-grained, massive diorite to gabbro. They have abundant plagioclase feldspars (>40 modal %) that are fine-grained and sericitized. Together with pleochroic, green to beige, fine- to medium-grained, hornblende, they produce a local salt and pepper mottled appearance (Plate 2.5). Up to approximately 10% recrystallized quartz is present in the groundmass of the diorite phase. Accessory phases include very fine-grained apatite, epidote locally as veinlets (Plate 2.6), and magnetite. Chlorite alteration is commonly present with sericite alteration typically reserved to contact and shear zones proximal to mineralization. Trace, very fine- to fine-grained chalcopyrite is associated with disseminated pyrite and magnetite.

2.2.4 Lamprophyre Dykes

In the vicinity of the Thor vein, mesocratic, fine-grained dykes (Figure 2.3) are typically associated with the mineralized veins (Plate 2.7). They are east-west trending, dipping moderately to the south (~50°), with a thickness of 1-2m. These dykes crosscut the granodiorite, monzogranite sheets and the metadykes, but are interpreted to be older than quartz vein emplacement, alteration, and gold mineralization. The presence of mineralized quartz veins and brecciated fragments of the mesocratic dykes within the mineralized Thor vein provides clear evidence for their pre-mineralization emplacement. These dykes are biotite porphyritic and have a matrix of quartz, potassium feldspar, and minor titanite and pyrite (Plate 2.8). Amphibole and pyroxene are strongly (>70%) altered to sericite and carbonate. These dykes are assumed either to comprise part of the Precambrian Long Range Dyke Complex or to be associated with a younger, possibly Silurian-Devonian, intrusive event.

2.2.5 Quartzite

To the east of the Viking deposit are a series of metamorphosed and deformed Cambrian to Ordovician clastic and carbonate rocks interpreted to be part of the Labrador Group. Bradore Formation quartzites has an unconformable relationship with the Grenvillian basement (Plate 2.9A). The conglomerate is composed of subrounded to rounded, fine- to medium-grained, moderately sorted, weakly deformed quartz clasts in a matrix of fine-grained sericite, weakly chloritized biotite, recrystallized quartz, and pyrite (Plate 2.9B).

2.2.6 Phyllites

The phyllites of the Forteau Formation contain 1-2 mm biotite porphyroblasts that are typically euhedral and are set in a strongly foliated matrix of fine- to very fine-grained sericite, recrystallized quartz, and pyrite. A number of the biotite porphyroblasts preserve an internal fabric defined by matrix inclusion trails. Outcrop and petrographic observations indicate that these porphyroblasts record east side down, dextral rotation relative to the surrounding matrix. Locally, other biotite porphyroblasts completely overgrow the foliation. The crenulation cleavage in outcrop is smooth and anastomosing composed of sericite and quartz. Pyrite is associated with many mineral phases in the phyllite including the biotite porphyroblasts and sericite alteration.

2.3 LOCAL STRUCTURAL CONTROLS ON MINERALIZATION

Figure 2.2 presents the simplified geology of the Viking property overlain by both interpreted and observed structural features. The DVFS has an orientation of 030° NNE and dips steeply to the east. Topographic linears, which are inferred as faults, strike

approximately 056° and 062° and intersect the DVFS (dashed black lines in Figure 2.2). Narrow fault zones with variable displacements and mineralized fracture zones have an orientation of 088° to 091° (blue dashed lines on Figure 2.2). A penetrative foliation is developed within the megacrystic granodiorites and monzogranites which trends NE (dipping steeply east) unless disrupted by local structures. The metadykes are typically shallow to moderately dipping (Figure 2.4) and are not a receptive host for gold veins and mineralization. This unit is a critical structural aspect of the geological system in that it acts as a potential aquifer, trapping mineralizing fluids.

A brittle dextral Riedel shear model is envisaged for the structures observed at the Viking deposit (Figures 1.13 and 1.14 in Bursnall, 1989; and Figures 6.16a and 6.19a in McClay, 1987). NE-trending linears correspond to the orientation of R1 shears in the Riedel model while E-trending narrow fault zones represent R2 shears (Figure 2.2). These narrow R2 fault zones host the best examples of gold mineralization, including the Thor Vein.

2.4 THOR TREND MINERALIZATION

An independent resource estimate for the gold mineralization (cut-off grade of 0.20 g/t gold) in the Thor trend reported an indicated resource of 98 000 ounces (3,232,000 tonnes at an average grade of 0.95 g/t) and an inferred resource of 45 000 ounces (2,123,000 tonnes at an average grade of 0.66 g/t; Ebert, 2011). The Thor trend is a tabular, 30 to 80 m wide, zone of strong sericite–quartz–pyrite alteration with gold, and minor base metal, mineralization. The surface expression of the Thor trend is

demonstrated in Figure 2.3. The Thor trend has an open strike length, its lateral extent is currently constrained at *ca.* 1500 m, and the mineralized zone dips to the west. The deposit's vertical extent, as defined by diamond drilling, is 100-200 m (red and yellow outlines on Figure 2.4).

Numerous mineralized quartz sulfide veins of varying thickness (millimeter to decimeter scale) have been exposed at surface and intersected in drill core within the Thor trend. The Thor vein is an array of asymmetrical, 30- to 100-cm thick, openly folded veins with a surface extent of 30 m (Figure 2.3). The veins strike east–west, dip to the south, and continue down dip for at least 100 m. The subsurface geometry of the Thor vein is represented schematically in (Figure 2.5). It is a series of networking gold mineralized veins which crosscut the lamprophyre dykes, monzogranite, and the granodiorite.

Native gold forms irregular blebs in the quartz-sulfide veins variably sericite-altered host rocks. Gold occurs in the Thor vein in two settings: 1) as dispersed blebs in the quartz and; 2) as micro-inclusions in sulfides that are also hosted by quartz veining. The gold is typically fine- to coarse-grained, forming anhedral, rounded or elongate masses ranging from less than 50 μm to over 140 μm in diameter. Gold occurs locally along fractures in the vein quartz and is spatially associated with sulfide assemblage. The sulfide assemblage in the veins consists of euhedral, fine- to medium-grained pyrite (2–3%), anhedral, fine-grained sphalerite and galena (1–2%), and lesser amounts of anhedral blebby chalcopyrite (typically $\leq 0.5\%$).

2.4.1 Scanning Electron Microscope

Samples from the Thor vein array were selected for scanning electron microscopy (SEM) to examine the gold and its relationships to both sulfide and silicate minerals. Analytical methods are given in Appendix A.1. Plate 2.10 A-C clearly shows that gold occurs as inclusions in pyrite and quartz. Gold is also present as inclusions in sphalerite (Plate 2.10 D) and is locally associated with galena. The gold grains are silver-bearing and locally occur proximal to examples of what is interpreted to be native silver (Plate 2.10 D) Sericite, calcite and pyrite are intergrown with quartz and are spatially and texturally associated with gold (Plate 2.10 E). This textural evidence suggests a genetic relationship between the quartz veins, alteration minerals, gold mineralization, and base metal sulfides.

2.5 LITHOGEOCHEMISTRY

2.5.1 Element Mobility

Sericite-calcite-pyrite alteration is intense surrounding the mineralized quartz veins at the Viking deposit, a common characteristic of orogenic gold deposits (Kerrich, 1993; McCuaig and Kerrich, 1998). The mineral assemblages produced during alteration in these deposits are dependent on host rock types, pressure–temperature conditions, and fluid/rock ratios, and typically display enrichments in CO_2, LILE, S, gold and other pathfinder elements (Cassidy, *et al.*, 1998). Relative elemental gains and losses were calculated, using the technique from Grant (1986), for the most common host rock type, the granodiorite, and the results are presented in Figure 2.6. The actual mass gain and loss

calculations are located in Table B.3. The most altered sample used in the calculation was 09MM058 and the least altered was 09MM042 (Table B.1).

Relative gains in the major elements were observed for SiO_2, Al_2O_3, and CaO. The relative increase in CO_2 and a gain in CaO correlate with the presence of calcite within the alteration assemblage. The base metals, Ag, and gold display relative enrichments compared to the least-altered sample and pathfinder elements such as Sb, As, W, and Sc are also enriched. Large-ion-lithophile elements display variable depletion, with enrichment in Cs and Th, HFSE and REE appear to be depleted within the alteration halo.

The results suggest that certain elements are mobile, including elements that are traditionally considered immobile such as the HFSE, some of the REEs, and Al_2O_3. The presence of carbonic fluids can mobilize such elements as TiO_2, Zr, and some of the REEs: however, Al_2O_3 should be immobile in high pH fluids. Based on the presence of high LOI , Al_2O_3/Na_2O ratios, and CO_2 contents, there is mobility of certain elements (e.g. alkalis and LFSE) and there is evidence to suggest that some HFSE and REEs are also being mobilized. The "least altered" sample may not represent the perfect control sample (i.e. the protolith) since hydrothermal sericite-calcite-pyrite alteration and natural variation in the geochemical composition of the Main River granodiorite may be causing these traditionally immobile elements to appear mobile.

2.5.2 Major Element Chemistry

The rock types from the Viking property have variable major-element chemistries, influenced to a large extent by post-crystallization hydrothermal alteration. As such,

classification and interpretations of their primary chemistries and petrology using mobile elements is very suspect. The potassium-feldspar megacrystic biotite granodiorite of the Main River Pluton exhibits major-element composition that is not strongly fractionated and is characterized by intermediate SiO_2 (59.25–70.74 wt. %) and Mg# values (*ca.* 22–35; Table B.1). The monzogranite has the lowest Mg#s (average = 30) and highest SiO_2 concentrations. With decreasing silica content there is a correlative decrease in Al_2O_3, FeO, MgO, CaO, Na_2O, K_2O, TiO_2, MnO, and P_2O_5. The metadykes that crosscut the granitoid rocks are the geochemically most primitive samples, characterized by low SiO_2 and moderate Mg#s ranging from 31.2 to 55. They have a wide range of K_2O and exhibit FeO* and TiO_2 enrichment with differentiation. The lamprophyre dykes have intermediate SiO_2, Cr, Ni, Sc, and Co, and high K_2O, are strongly sericite and carbonate-altered as reflected by enriched CO_2, LOI and K_2O, and have Mg#s that overlap with those of the metadykes.

2.5.3 Trace Element Chemistry

Owing to the variably altered nature of the host rocks, trace elements that are considered to remain immobile during hydrothermal processes were used for further interpretations. The granodiorite has Zr/TiO_2 and Nb/Y ratios which characterize it as transitional from Andesite/Basalt to Rhyolite-Dacite on a revised Winchester and Floyd (1977) plot (Figure 2.7 A). It contains high Ga/Al ratios (*ca.* >2.5) indicating an A-type geochemistry (Figure 2.7 B) (Whalen, *et al.*, 1987).

Figure 2.8 A shows a NMORB-normalized multi-element plot for the granodiorite along with plots for the correlative Apsy Granite and Potato Hill Pluton (Owen, *et al.*,

1992). This is underscored by a strong enrichment in LIL elements and LREE [$(La/Sm)_{CN}$ = 3.05-4.25] relative to HREE [$(Gd/Yb)_{CN}$ = 1.84-2.58], Rb and Ba enrichment relative to Sr and Ce and, distinct troughs in the patterns at Ta-Nb, P and Ti. The granodiorite and Apsy Granite have depleted HFSE and HREE relative to the Potato Hill Pluton. The pattern exhibited by the granodiorite is comparable to those of shoshonitic rocks (e.g. Macdonald, *et al.*, 1985; Mauger, 1988; Wyman and Kerrich, 1989) and similar to that of the Apsy Granite and the Potato Hill Pluton (Figure 2.7 A)

The monzogranites have I-type chemistry (Figure 2.7 B) and have the most depleted REE patterns compared to all other rock types at the Viking deposit. Akin to the granodiorite, the monzogranite exhibits enrichment in the LILE compared to Sr and Ce and has distinct troughs at Ta-Nb, P, and Ti (Figure 2.8 B). The monzogranite sheets exhibit a wide range in LREE enrichment [$(La/Yb)_{CN}$ = 2.44-81.08] with less variable HREE ratios [$(Gd/Yb)_{CN}$ = 1.06-5.43]. The most LREE-enriched sample contains the most depleted HREE concentrations. A number of samples show a concave upward REE pattern with a positive Eu anomaly, suggesting feldspar accumulation. The REE patterns for the monzogranite sheets are similar to these for the equigranular granite of Owen *et al.* (1992).

The lamprophyre dykes are subalkaline (Nb/Y < 0.8; Pearce, 1996). They have compositions similar to calc-alkaline lamprophyres, characterized by low Nb/Pb and high V/Cr ratios (Figure 2.7 C). Figure 2.8 B displays a NMORB normalized plot for the lamprophyre dykes. They show a strong enrichment in the more incompatible elements and display strong LREE-enriched [$(La/Sm)_{CN}$ = 2.01-6.02] negatively sloped patterns. MORB-like concentrations are observed for Y, Ti, and HREEs. Lamprophyres typically

exhibit H_2O, CO_2, F, Cl, LILE, P, Rb, Ba, LREE and Th concentrations at levels two to three orders of magnitude higher than MORB, but MORB-like levels of Y, Ti, HREE, and Sc (Rock, 1991).

The metadykes contain substantial Cr (30–130 ppm) and Ni (30–80 ppm) and are classified as subalkaline and tholeiitic based on their mobile major element and immobile trace-element chemistry (Irvine and Baragar, 1971; Pearce, 1996; Winchester and Floyd, 1977). The metadykes have the most diverse multi-element plots of the rock types studied. There are four types of dykes that can be distinguished by their LREE, Nb, and HFSE abundances (Figure 2.8 C). Type 1 metadykes have consistent, mutually parallel patterns with a shallow negative slope indicating only slight LREE enrichment relative to the HREE. A second variety (Type 2; n=2) have more fractionated patterns with significant LREE enrichment relative to Th and Nb. This type also shows a distinct negative Ti anomaly and depleted HREE abundances relative to Type 1 and 3 metadykes. Type 3 metadykes (n=1) have a similar pattern to Type 2, however, they display a positive Nb anomaly. Type 4 metadykes (n=1) have depleted LREE compared to the other types and have a weakly negative sloped pattern with depleted HREE. Differences in REE abundances, Nb concentrations, and overall patterns suggest variable continental crust contamination.

2.6 ASSAY RESULTS

Fourteen analyses of gold-bearing quartz sulfide Thor vein array samples were added from the Northern Abitibi Mining Corporation assay database to complement the lithogeochemical dataset presented in this study. Gold values range from 589 to 222950

ppb (mean=57220 ppb) with higher assay results ascribed to the 'nugget effect' of gold. Gold concentrations correlate well with the base metals (Cu, Zn, Pb), and Ag (Figure 2.9) and correlate weakly with Cr, Co, Ni, Sr and Ce. As is not meaningfully correlated with gold. Gold-bearing veins exhibit variable enrichments in Cu, Zn, and Pb. Au/Ag ratios range from 0.6 to 14 (average = 5; Table 2.1) indicating that gold is enriched relative to silver. These ratios are generally greater than 5/1 (Au/Ag) typical in most orogenic gold systems (Groves *et al.*, 2003).

2.7 ^{40}AR-^{39}AR THERMOCHRONOLGY

Four samples were collected for ^{40}Ar-^{39}Ar thermochronological analysis; three strongly sericitized granitoids (two monzogranites and one granodiorite) from the Main River Pluton within the alteration envelope of the Thor trend, and a strongly foliated phyllite belonging to the Forteau Formation of the Labrador Group. Argon-argon analysis of euhedral biotite porphyroblasts was designed to address the age of metamorphism and deformation and constraints on fine-grained pervasive muscovite formation and therefore the inferred timing of gold deposition. Brief descriptions of the samples and their UTM co-ordinates are presented in Table 2.2.

The two monzogranite samples are heavily fractured and contain 1% disseminated pyrite accompanied by strong pervasive sericite alteration (Plate 2.11 A, B). Sample 09MM099 was collected 10 meters north of the Thor vein (Figure 2.3) and sample 09MM113 was taken two hundred metres south of the Thor vein, at surface. The sericite-altered granodiorite sample is located 15 m northwest of the Thor vein and also contains

disseminated pyrite. The phyllite of the Labrador Group is located along the eastern property boundary and was exposed through trenching.

In the monzogranite (09MM113 and 09MM099), pervasively sericitized potassium feldspar and plagioclase (Plate 2.11 B) are intergrown with polycrystalline aggregates of fine-grained quartz. Fine-grained disseminated pyrite is commonly rimmed by magnetite and hematite and associated with the altered feldspars and locally quartz. The granodiorite exhibits similar alteration mineralogy, however, it also locally contains biotite that encloses megacrystic potassium feldspar. The phyllite (09MM024) is characterized by a very strong vertical dominant foliation defined by aligned, fine-grained sericite, biotite, and quartz (Plate 2.11 C, D). An asymmetric crenulation cleavage and 1-2 mm-scale biotite porphyroblasts can be observed on broken foliation surfaces.

2.8 STEP-HEATING RESULTS

An aliquot of biotite from the deformed phyllite (09MM024) yielded a very well-defined, consistently flat gas-release spectrum (Figure 2.10A). This analysis produced a total gas, integrated age of 418 ± 2 Ma. Eleven of 14 steps, representing 99.12 % of the total ^{39}Ar released, gave a plateau age of 419 ± 2 Ma [(MSWD) = 0.84; probability of fit (POF) = 0.62] overlapping within error of the integrated age. The corresponding inverse-correlation age (^{36}Ar-^{40}Ar *versus* ^{39}Ar-^{40}Ar) of 418 ± 1.5 Ma (MSWD = 0.84) also overlaps within error with the plateau and integrated ages. These data collectively indicate that an age of 419 ± 1.5 Ma represents a robust cooling age for this biotite and therefore represents the time at which the sample cooled through *ca.* 280°C (McDougall

and Harrison, 1988). A simple thermal history is inferred for this sample because of close agreement of integrated, plateau and isotope correlation ages.

A single aliquot of fine-grained sericite concentrate from monzogranite sample 09MM113 produced a well-defined argon release spectrum with young ages recorded in the low-power gas steps, a series of mutually consistent steps in the middle, and significantly older ages produced at higher power (Figure 2.10B). Five of 13 gas steps, representing 61.7 % of the ^{39}Ar released yielded a plateau age of 384 ± 2 Ma (MSWD = 1.2: POF = 0.30). An inverse isotope correlation age for the same five steps of 364 ± 21 Ma is significantly younger than, but overlaps within error, the plateau age. The plateau age is therefore interpreted as a reasonable estimate of the cooling age when the sericite passed through *ca.* 350° C (McDougall and Harrison, 1988; Singer and Pringle, 1996; Snee, *et al.*, 1988).

Sericite from another monzogranite sample (09MM099) yielded a poorly defined argon release spectrum (Figure 2.10C). The pattern for this sample is comparable to that of sample 09MM113 with young ages at low power, a pseudo-plateau through the middle, and an older pseudo-plateau segment at higher power. The pseudo-plateau age of 399 ± 2 Ma for the central segment represents 57.9 % of the ^{39}Ar released during four steps (MSWD = 0. 68, POF = 0.51). The higher power pseudo-plateau segment representing only 17.3 % of the ^{39}Ar released (MSWD= 0.034: POF= 0.992), yielded an age of 409 ± 12 Ma. The incrementally ascending spectrum for this specimen suggests that the higher power gas steps may represent a maximum age of gold deposition. This age overlaps within error the age constraints on the mineralization at the Rattling Brook deposit (Kerr and van Breemen, 2007). The younger, lower power, gas release steps suggest partial

resetting of the ^{40}Ar-^{39}Ar systematics during a younger hydrothermal (or tectonothermal) event at *ca.* 380 Ma.

A sample of a sericite-altered granodiorite (09MM098) produced a gas release spectrum very similar to that of 09MM099 in having incrementally increasing ages for higher power gas release steps. The high power pseudo-plateau consisting of five of eighteen steps and representing 25.7 % of the ^{39}Ar released gave an age of 386 ± 2 Ma (MSWD = 0.68, POF = 0.60). The lower power pseudo-plateau, comprising six of eighteen steps and representing only 37.9 % of the total ^{39}Ar released (MSWD = 0.38; POF = 0.86: Figure 2.10D) yielded an age of 377 ± 2 Ma. This spectrum suggests a *ca.* 388 Ma primary cooling age for the sericite, but that this has been partially reset during later, *ca.* 377 Ma hydrothermal activity.

2.9 DISCUSSION

2.9.1 Ore Mineralogy

Orogenic gold deposits are characterized by quartz-dominant vein systems with ≤3-5 % sulfide minerals (typically Fe-sulfides) and ≤5-15 % carbonate minerals (Groves *et al.*, 1998). Pyrite (and/or pyrrhotite) is the most common sulfide in deposits hosted by metamorphosed igneous rocks. Gold-bearing veins exhibit variable enrichments in As, B, Bi, Hg, Sb, Te, and W; Cu, Pb, and Zn concentrations are generally only slightly elevated above regional backgrounds (Groves *et al.*, 1998). The gold-silver veins within the Thor trend contain Cu, Pb, Zn, and Cr concentrations above regional background with Au/Ag overlapping the typical range for these deposit types. Silver-bearing gold grains are present throughout the mineralized veins, but the absence of arsenopyrite is striking

considering its abundance in the Rattling Brook deposit to the north (Kerr, 2005; Saunders and Tuach, 1988, 1991). Also, the presence of base metals within the high-grade veins at the Viking deposit is also a notable difference from what is observed at Rattling Brook. This sulfide assemblage at Viking suggests similarities to mineralization present in the Browning Mine and Unknown Brook deposits (Figure 2.1B).

Gold mineralization observed at the Rattling Brook deposit (Figure 2.1B) is hosted by potassic-altered Apsy Granite and, primarily by, silicified carbonates of the Lower Cambrian Labrador Group (Kerr, 2005). It is a large, low-grade deposit that lacks the larger and more continuous quartz veins so common in orogenic systems, and like those present at the Viking deposit. The gold at Rattling Brook is refractory (i.e., is in solid solution with the host arsenopyrite and pyrite), and there is very little associated Ag, Cu, Zn, Pb, Co, or Ni (and their sulfide minerals) in the mineralized rocks. Mineralization at the Viking deposit, in contrast, does contain associated Ag, and Cu, Zn, and Pb sulfides. Furthermore, the mineralization is not refractory based upon metallurgical studies (Ebert, 2010).

The West Corner Brook Prospect, the Browning Mine, and the Sims Ridge Prospect are examples of auriferous mineralization hosted within the Silurian Sops Arm Group that have been described as being orogenic (Currie, 2004; Kerr, 2006b). The mineralization at these prospects is associated with syn- to post-deformational quartz and quartz-carbonate veins that contain pyrite, chalcopyrite, galena, and sphalerite; Au-Ag correlations are noted at all prospects. The Thor Trend mineralization at the Viking deposit is epigenetic and is hosted by quartz-carbonate veins with similar sulfides as these

deposits. These similarities suggest a possible genetic link between the Thor Trend and the Sops Arm Group gold mineralization.

2.9.2 Lithogeochemistry

The Main River granodiorite has an arc-like, A-type geochemical signature. Halogen enrichments (e.g., F >1000 ppm), a ferroan composition along with high Ga/Al, and Zr, are characteristic of relatively anhydrous, lower crustal, within plate, A-type granitic magmas typical of deep crustal anorogenic extensional environments (Frost, *et al.*, 2001; Pearce, *et al.*, 1984). Other Grenvillian granitoid plutons of the LRI, such as the Apsy Granite and the Lake Michael Intrusive Suite (Owen, 1991), were emplaced contemporaneously with, and have geochemical features similar to, the Main River Pluton. These plutons were emplaced over a period of *ca.* 50 my, between 1032 and 985 Ma, and are termed Group 1 and Group 2 granitoids, respectively (Heaman *et al.*, 2002). The A-type nature of all of these roughly synchronous granite suites suggests an interval of deep crustal anatectic granitoid plutonism during the emplacement of Group 1 granitoids into the LRI.

The monzogranite sheets have calc-alkaline affinities with LILE enrichment. They are volcanic-arc granitoids and straddle the divide with syn-collisional granites (Figure 2.11). As the monzogranite sheets locally crosscut fabrics observed in the granodiorite, they may be contemporaneous with the younger, *ca.* 1000 Ma, Group 2 granitic rocks of the LRI (Heaman *et al.*, 2002).

The metadykes exposed at the Viking deposit are within-plate, continental tholeiitic basalts with variably developed negative HFSE anomalies (Figure 2.7 C).

Variable LREE, Nb, and HFSE abundances suggest that crustal contamination may have produced the heterogeneity in these elements. Their general northeast-trending orientation and overall geochemical signature suggests correlation with the *ca.* 615 Ma Long Range Dykes (Kamo *et al.*, 1989). The Long Range Dykes are interpreted to represent the products of rifting of the Grenvillian continental crust during the opening of the proto-Atlantic Ocean (Strong and Williams, 1972).

Globally, calc-alkaline lamprophyres are thought to overlap gold mineralization in both space and time (e.g. Wyman and Kerrich, 1989). Rock (1991) suggested that because of their unusual mineralogy and bulk chemistry (*e.g.*, high LIL elements, CO_2, Ba, and moderate S), lamprophyric melts are similar to mineralizing fluids and they may easily transport gold. Although the absolute timing of the crystallization of the calc-alkaline mesocratic lamprophyres associated with the mineralized Thor vein array has not been constrained, field and textural evidence suggest they were emplaced either pre- or syn-vein formation and gold deposition.

2.9.3 Timing of Gold Deposition at the Viking Deposit

Conformable deposition of the Forteau Formation above the Bradore Formation is constrained to the late Early Cambrian (Williams and Stevens, 1974). The minimum age of last, peak low-grade metamorphism has thus been constrained through analysis of syn- to late-kinematic biotite porphyroblasts in a late Early Cambrian phyllitic schist located at the western edge of the contact between the Bradore and Forteau formations. The biotite cooled through *ca.* 280°C in the Late Silurian at 419 ± 1.4 Ma. This determination overlaps, within error, the *ca.* 425 ± 10 Ma age of emplacement of the Devil's Room

Granite to the north (Figure 2.12). The syn- to post-kinematic nature of the biotite porphyroblasts suggests that peak metamorphism likely occurred during emplacement of the Devil's Room Granite and the region then rapidly cooled through *ca.* 280° C. Latest high temperature deformation along this segment of the DVFS therefore occurred during the Late Silurian, corresponding to the Salinic Orogeny (van Staal, 2007).

Textural evidence indicates that gold-electrum mineralization is intergrown with hydrothermal sericite. The ^{40}Ar-^{39}Ar thermochronological analysis of sericite from altered rocks in the Thor trend produced a range of cooling ages. Their Late Silurian to Early Devonian pseudo-plateau age of 409 ± 12 Ma overlaps, within error, with both the minimum age of peak low-grade metamorphism (*ca.* 419 Ma, sample 09MM024), and the emplacement age for the Devil's Room Granite, and correlates with the inferred timing of gold mineralization at the Rattling Brook deposit (415-409 Ma; Kerr and van Breemen, 2007). This *ca.* 409 Ma sericite age thus provides a minimum age, and may best approximate the age of gold deposition at the Viking deposit.

The well-defined Early to Middle Devonian pseudo-plateau ages of sericite (Figure 2.10C, D) represent reliable estimates for possible later episodes of fluid flow, alteration and gold deposition in the Thor trend at *ca.* 350° C. Fluid inclusion analysis on the Viking gold occurrences (Chapter 3) suggests that the fluids responsible for deposition of gold were at *ca.* 240–320° C at depths of 5–11 km. This temperature range and the uncertainties in the results (+/- 50°) overlap with the closure temperature for sericite–muscovite. These data therefore permit the proposal that the sericite and gold were initially deposited at *ca.*, 409 Ma (oldest high power steps in the three sericite

spectra) and that the sericite has been partially reset during later hydrothermal events (lower power steps).

On a regional scale throughout the northern Appalachian Orogen, the 409 Ma age of gold mineralization at the Viking deposit correlates with Lower Devonian Re-Os age determinations at the Stog'er Tight deposit (411 ± 7 Ma; Kerr and Selby, 2011) and at the Ovens deposit in Nova Scotia (Figure 2.11; 407 ± 4 and 409 ± 5 Ma; Morelli, *et al.*, 2005).

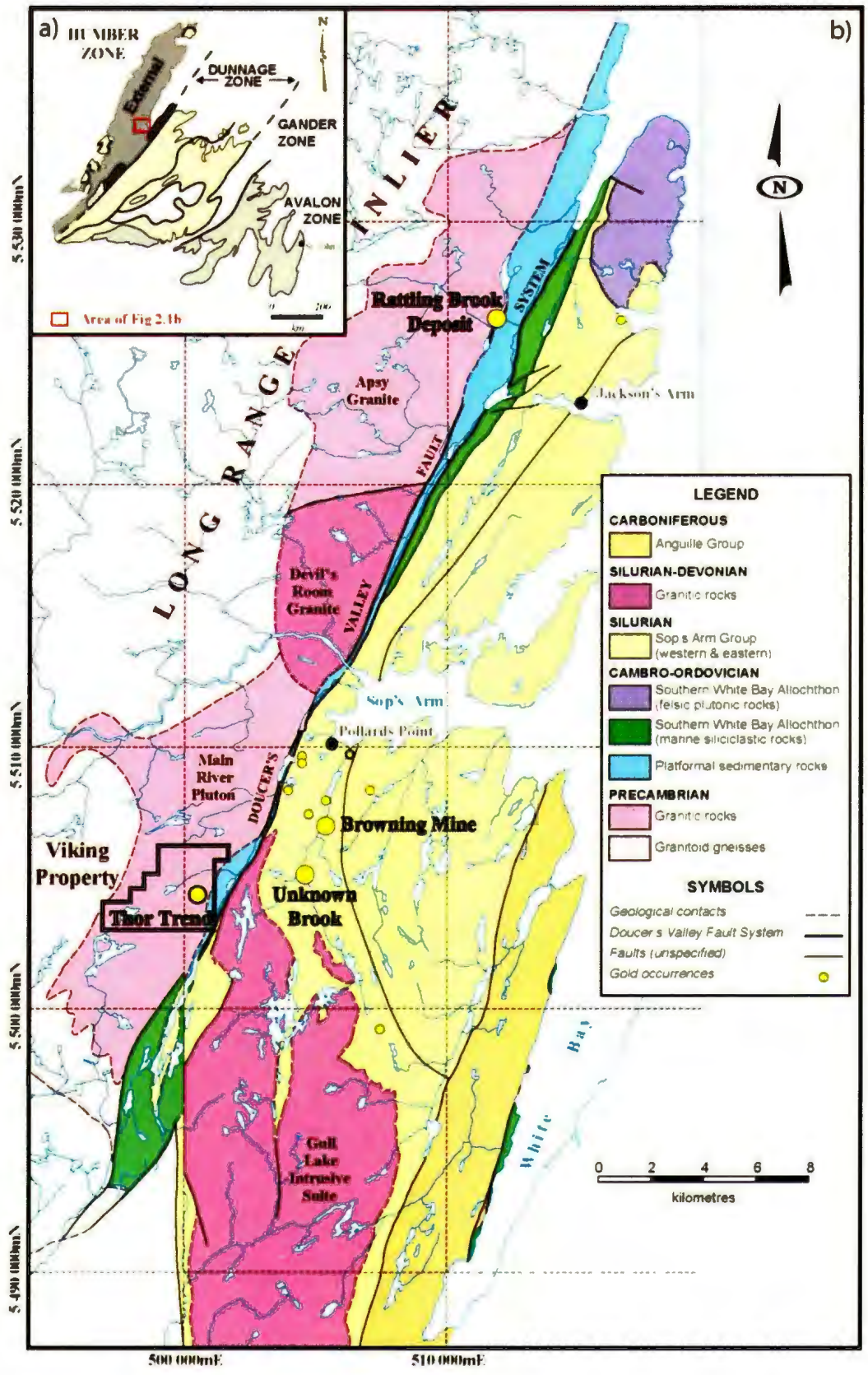
a)
HUMBER ZONE
External
DUNNAGE ZONE
GANDER ZONE
AVALON ZONE
Area of Fig 2.1b
b)
N
LONG RANGE INLIER
Rattling Brook Deposit
SYSTEM
Apsy Granite
FAULT
Jackson's Arm
Devil's Room Granite
VALLEY
Sop's Arm
Pollards Point
Main River Pluton
DOUCER'S
Browning Mine
Viking Property
Tuor Trend
Unknown Brook
Gull Lake Intrusive Suite
White Bay
LEGEND
CARBONIFEROUS
Anguille Group
SILURIAN-DEVONIAN
Granitic rocks
SILURIAN
Sop's Arm Group (western & eastern)
CAMBRO-ORDOVICIAN
Southern White Bay Allochthon (felsic plutonic rocks)
Southern White Bay Allochthon (marine siliciclastic rocks)
Platformal sedimentary rocks
PRECAMBRIAN
Granitic rocks
Granitoid gneisses
SYMBOLS
Geological contacts
Doucer's Valley Fault System
Faults (unspecified)
Gold occurrences
0 2 4 6 8
kilometres
5 530 000mN
5 520 000mN
5 510 000mN
5 500 000mN
5 490 000mN
500 000mE
510 000mE

Figure 2.1: (Previous page) (A) Tectonostratigraphic map of the island of Newfoundland showing the location of the study area (red box) within the external Humber Zone. (B) Simplified regional geology of the White Bay area, western Newfoundland, modified after Churchill and Voordouw (2006) (UTM NAD27 for Canada). The Thor trend is highlighted within the Viking Property. Large circles indicate gold deposits discussed in the thesis.

Plate 2.1: Typical, moderately foliated, mesocratic potassium feldspar megacrystic granodiorite displaying cm-scale potassium feldspar megacrysts or augen (pink) in a fine-grained sericite-altered matrix.

Plate 2.2: Photomicrograph of Plate 2.1 showing intense sericitization (80% replacement) of feldspars and groundmass (cross-polarized light).

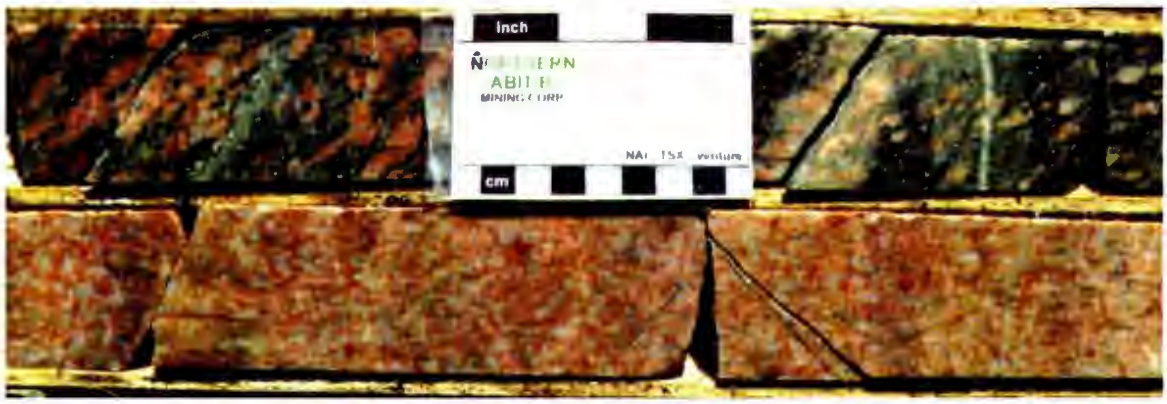

Plate 2.3: Drillcore photograph of a medium- to coarse-grained, salmon-pink colored monzogranite.

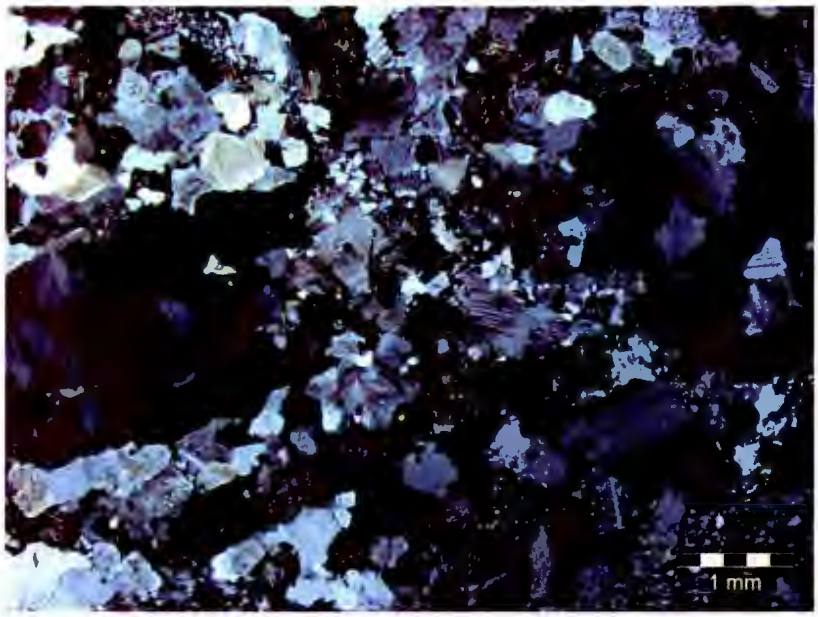

Plate 2.4: Photomicrograph of the monzogranite displaying sutured grain boundaries and granophyric textures (cross-polarized light).

Plate 2.5: Close-up, outcrop photograph of typical metadyke exhibiting a salt and pepper mottled texture.

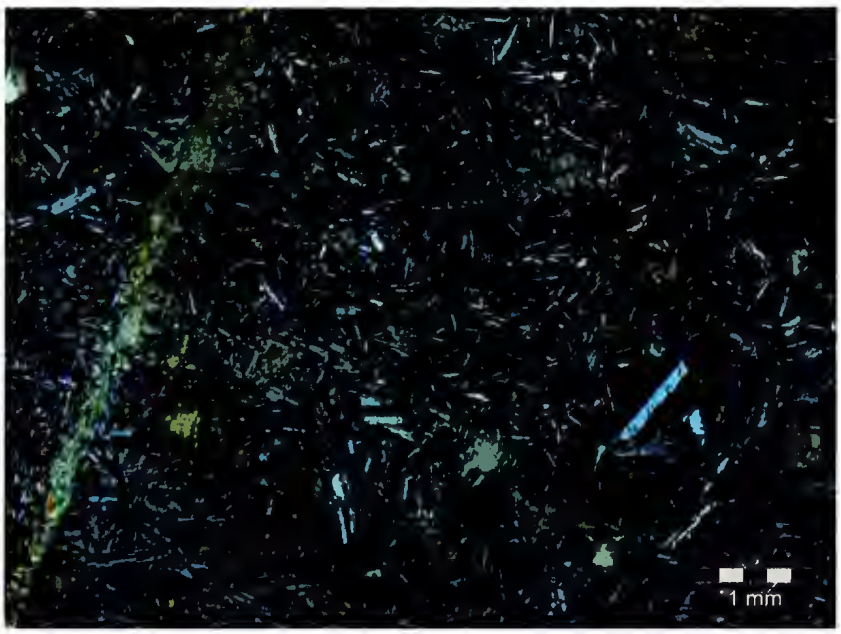

Plate 2.6: Photomicrograph of the mafic dyke showing plagioclase laths comprising the matrix with porphyritic texture and a sericite-chlorite-epidote veinlet (left) (cross – polarized light).

Plate 2.7: Bleached carbonate-altered lamprophyre dyke from hole 08-VK-03 (18.2 to 18.5 m depth) which is cut by mm to cm scale quartz sulfide veinlets.

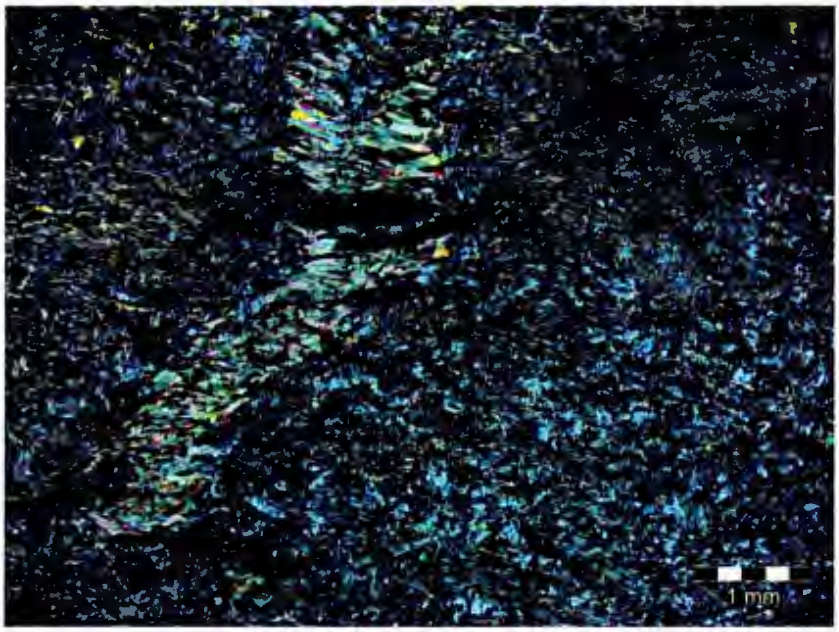

Plate 2.8: Carbonate- and sericite-altered matrix of a lamprophyre dyke which is crosscut by the Thor Vein (Figure 2.3) (cross-polarized light).

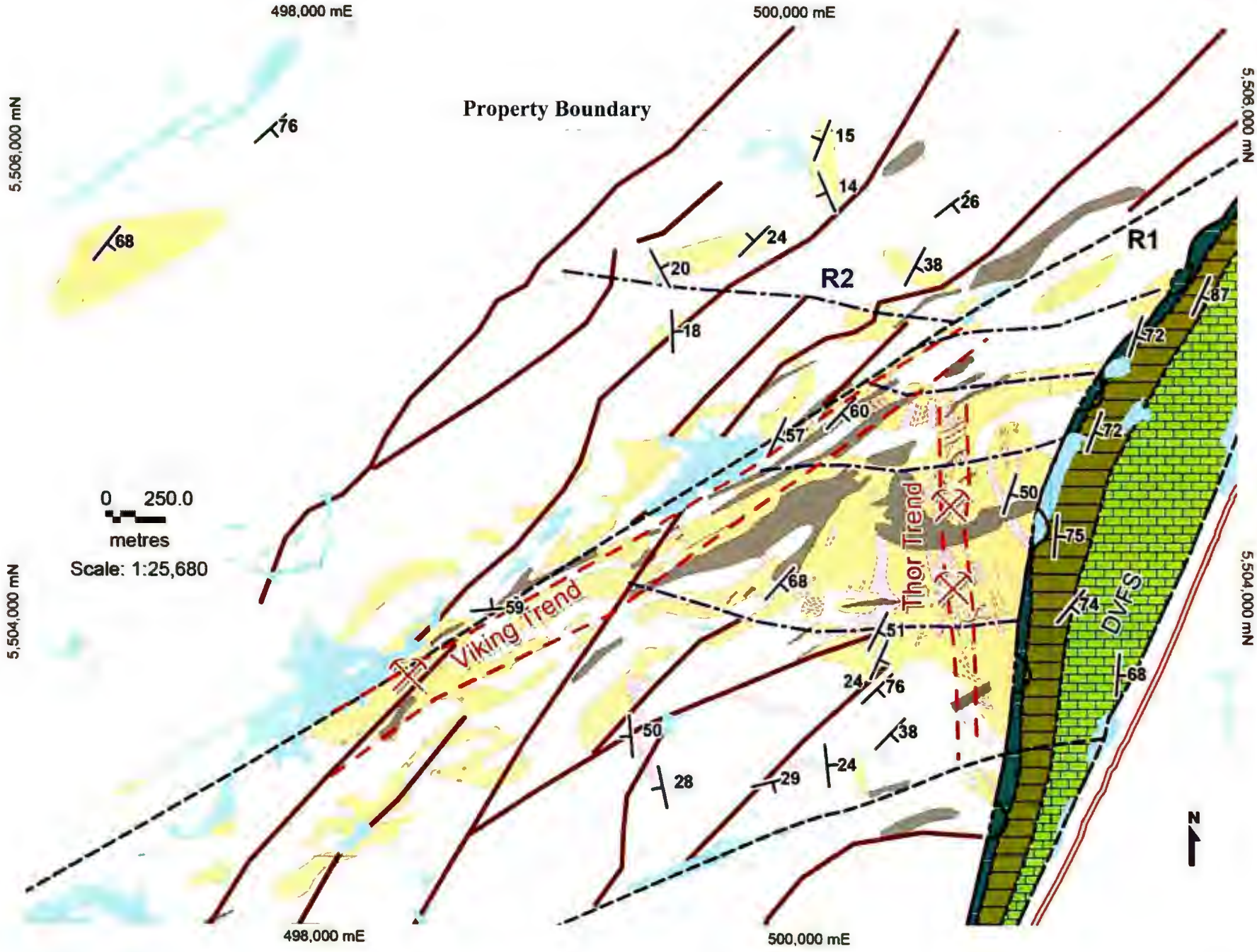
498,000 mE
500,000 mE
5,506,000 mN
5,504,000 mN
Property Boundary
R1
R2
Viking Trend
Thor Trend
DVFS
0 250.0
metres
Scale: 1:25,680
N

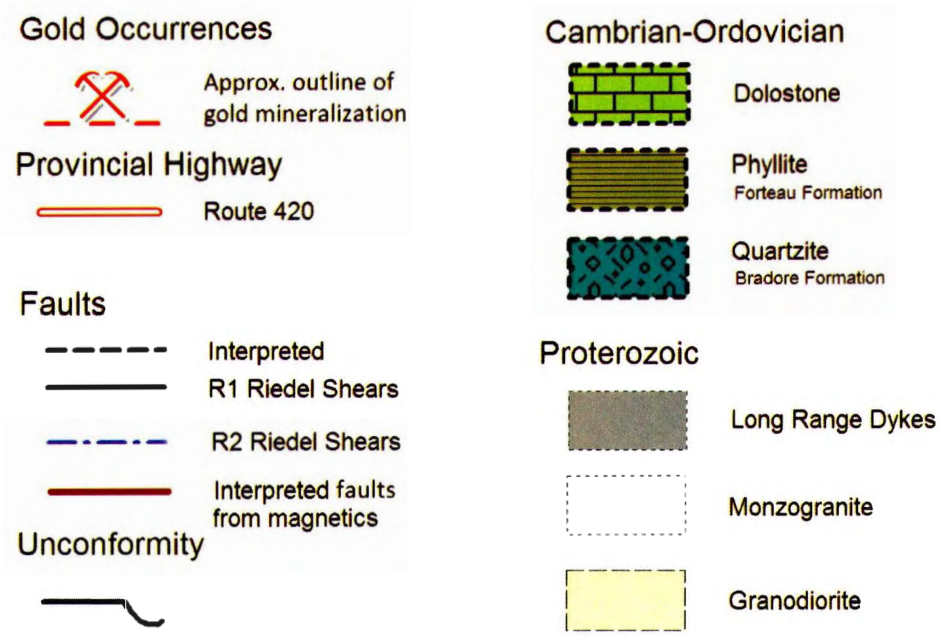

Figure 2.2: Simplified geologic map of the Viking Property (previous page) with corresponding legend (this page). The Thor vein is the northern most gold occurrence in the Thor trend. The location of the Viking trend occurrence is outlined along a prominent R1 shear.

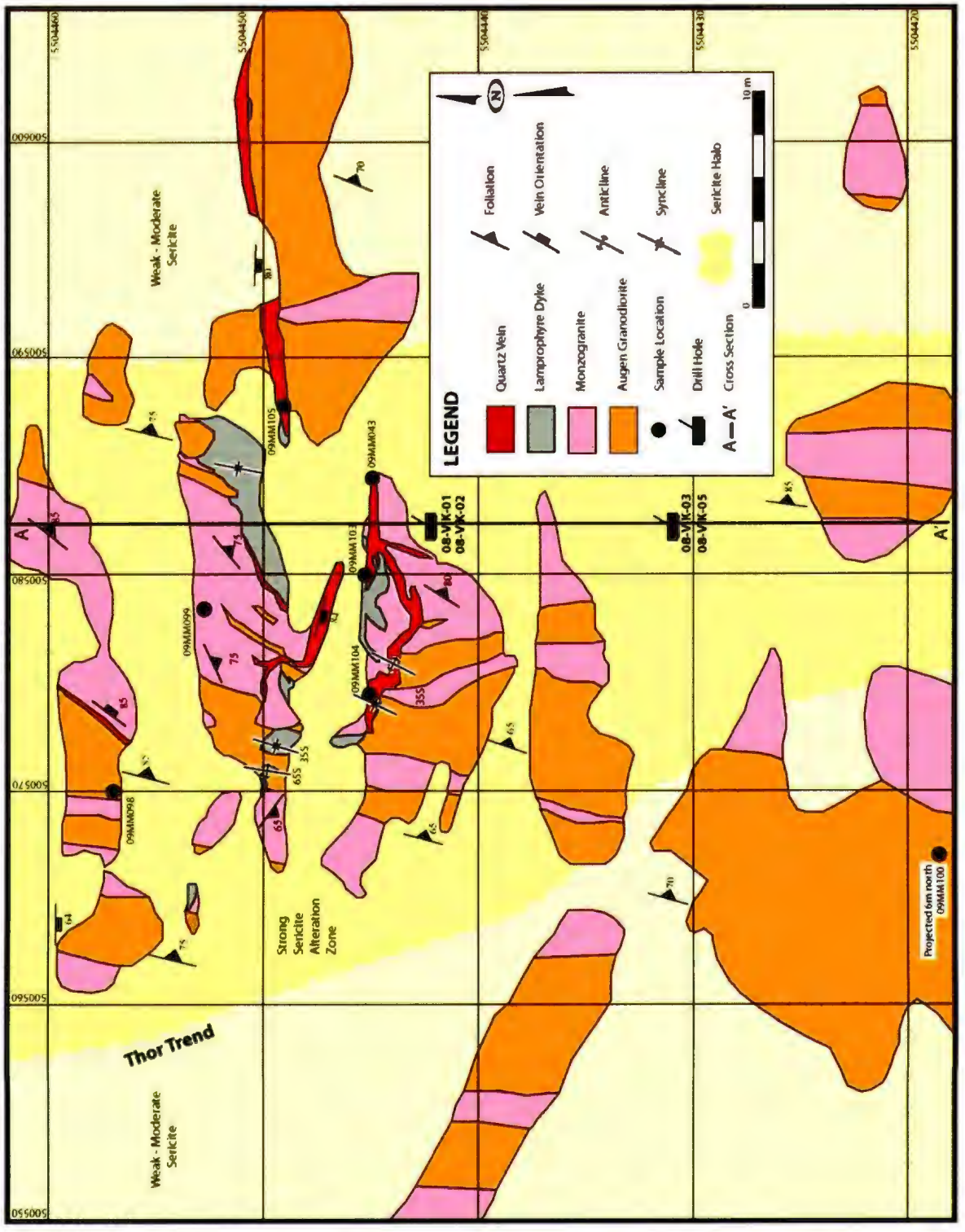

Figure 2.3: Simplified geological map of the Thor vein trench exposures. A well-developed sericitic alteration halo surrounds the east–west trending vein array which dips to the south. Metadykes do not outcrop in this map area.

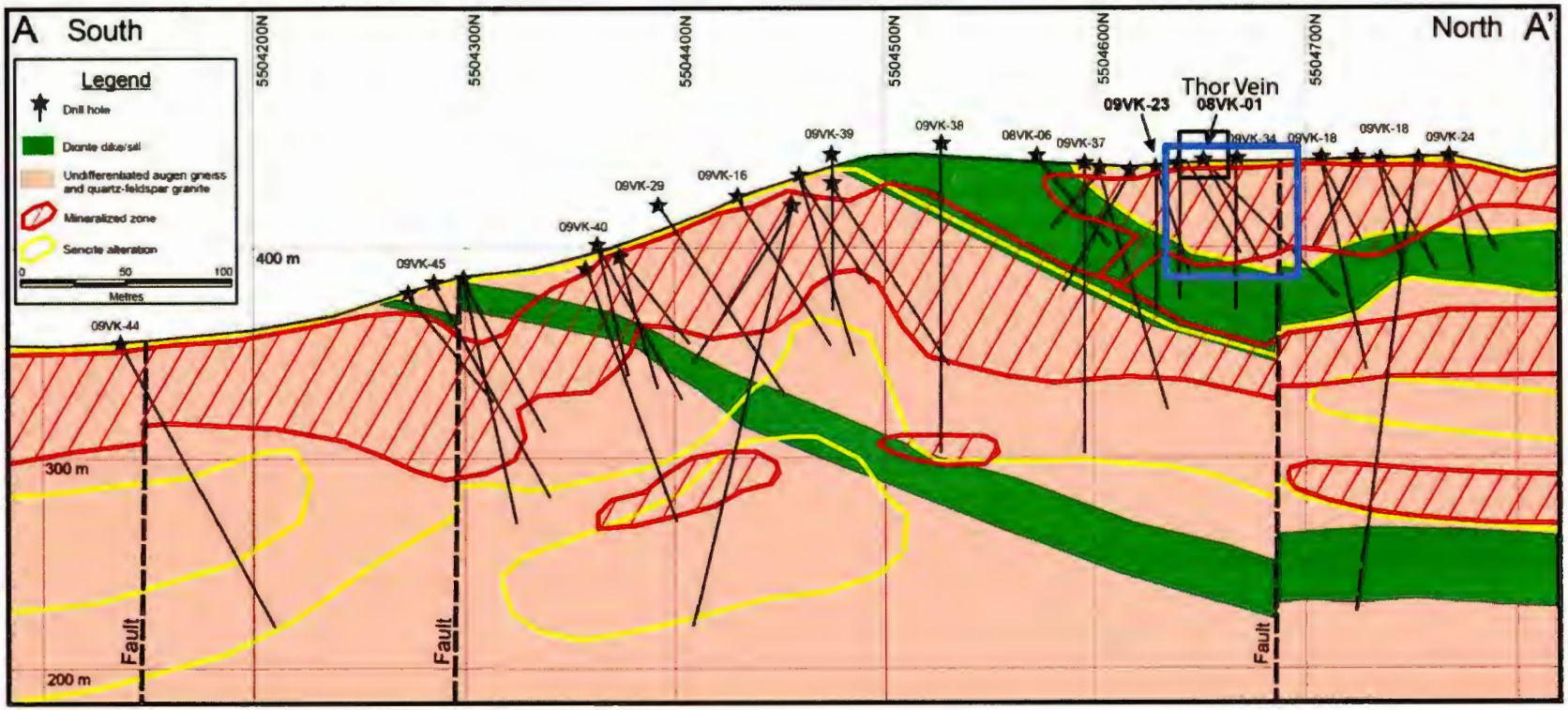

Figure 2.4: Simplified geological long section of the Thor trend gold mineralization. Black box in the Thor vein area indicates extent of Figure 2-3 and blue box indicates extent of Figure 2-5. Modified from NAMINCO's online map gallery (http://www.naminco.ca/mapgallery.php).

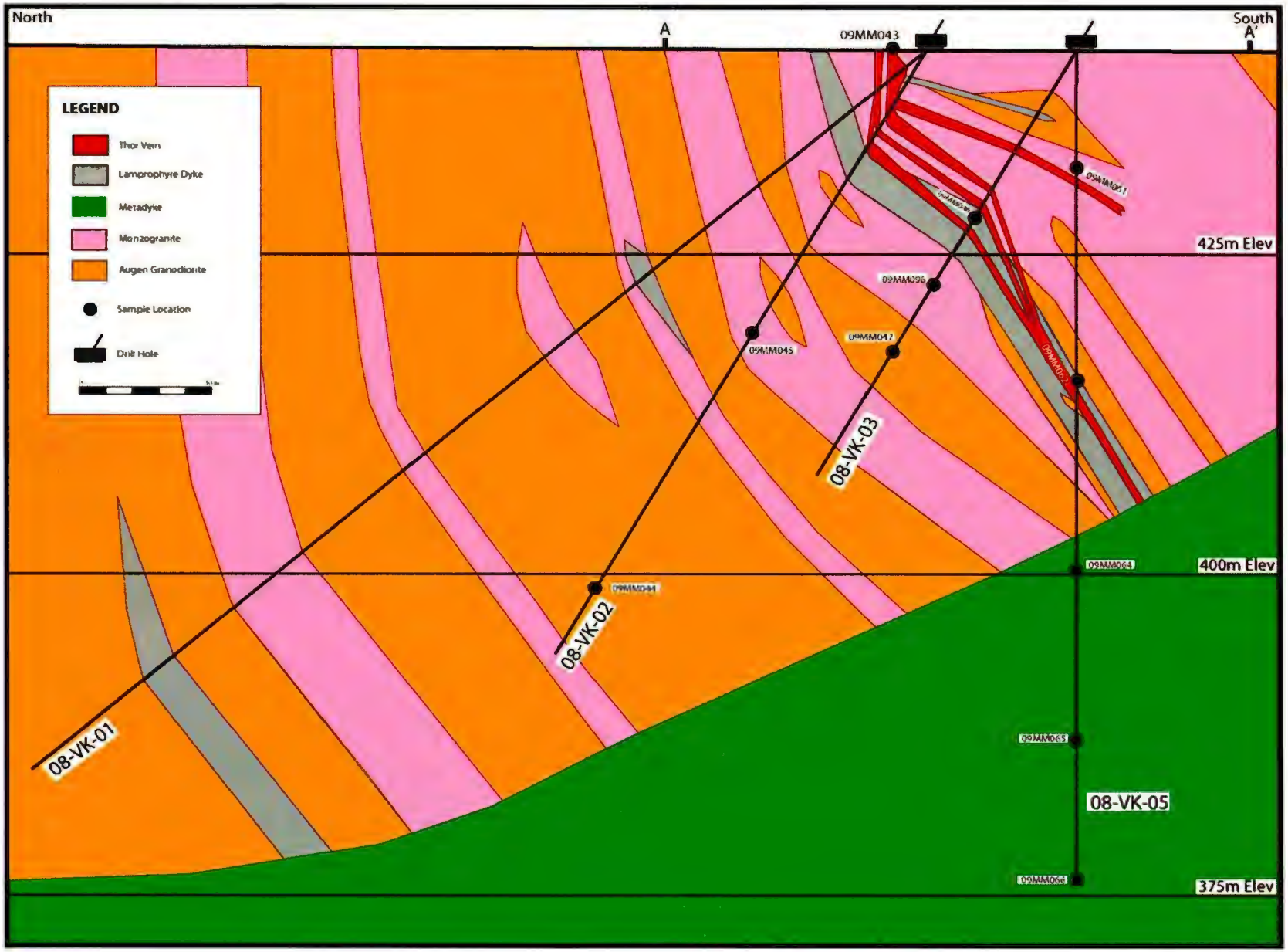
North
A
09MM043
South
A'
LEGEND
Thor Vein
Lamprophyre Dyke
Metadyke
Monzogranite
Augen Granodiorite
Sample Location
Drill Hole
425m Elev
09MM061
09MM096
09MM045
09MM047
08-VK-03
09MM064
400m Elev
08-VK-02
08-VK-01
09MM065
08-VK-05
375m Elev

Figure 2.5: (Previous page). Interpreted geological cross section through the Thor vein using drill holes 08-VK-01, 02, 03, and 05 from Figure 2-3 (A-A'). The Thor vein (red) dips steeply to the south and crosscuts the lamprophyre dyke (grey). The lithologies of this section, excluding the metadykes, are strongly sericite-altered.

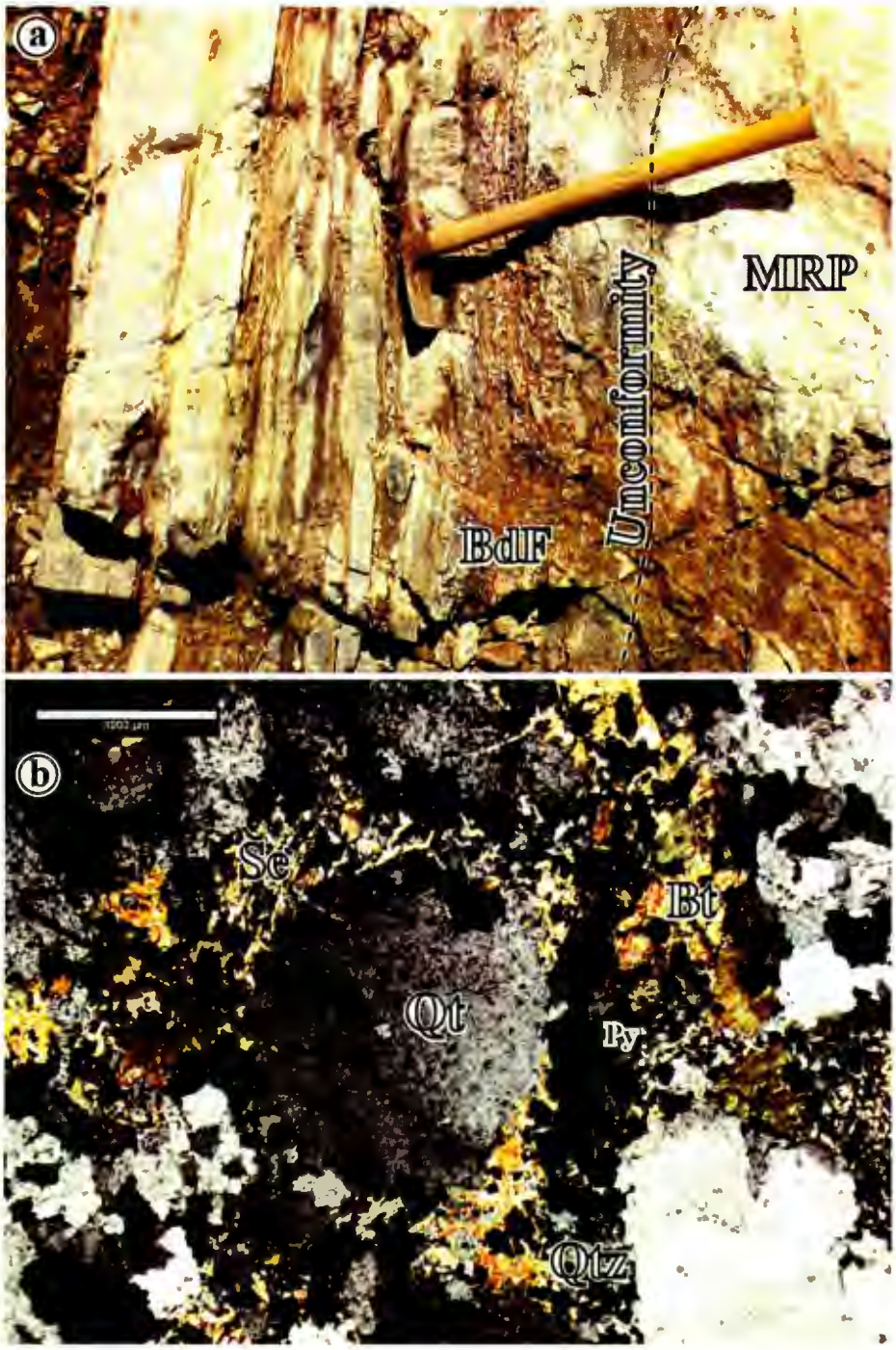

Plate 2.9: (A) Outcrop photo showing the Main River granodiorite (MRP), to the right, unconformably overlain by Bradore Formation (BdF) sedimentary rocks to the left. Alteration and conjugate joint sets crosscut the unconformity. Geotool is 1 meter in length. B) Photomicrograph of the Bradore Formation quartzite (cross-polarized light) with rounded quartz clasts (Qt) in a matrix of sericite (Se), biotite (Bt), recrystallized quartz (Qtx), and opaque pyrite (Py).

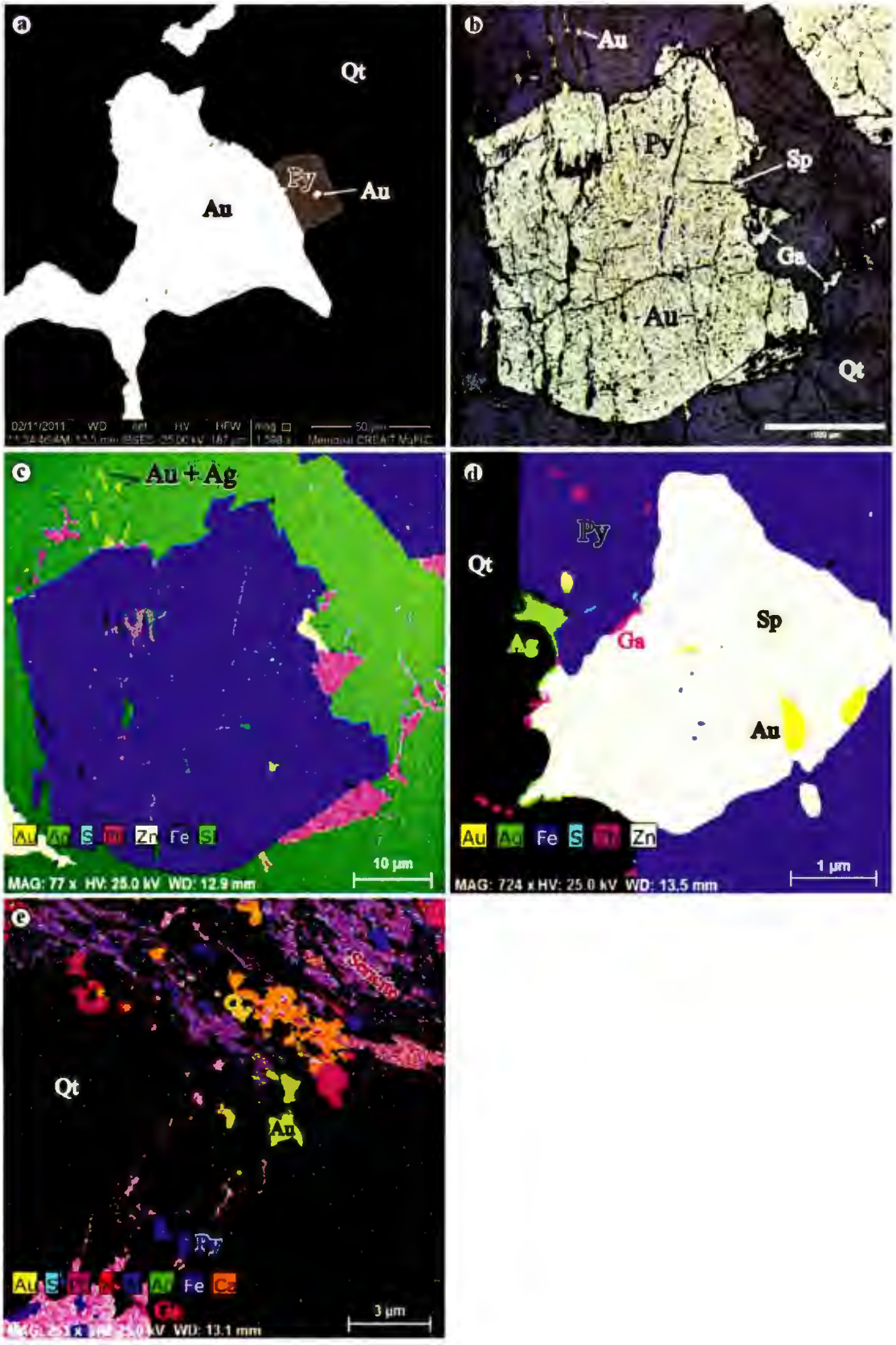
a
Qt
Py
Au
Au
b
Au
Py
Sp
Ga
Au
Qt
c
Au + Ag
Au Ag S Zr Fe Si
10 µm
MAG: 77 x HV: 25.0 kV WD: 12.9 mm
d
Py
Qt
Sp
Ga
Au
Au Ag Fe S Zn
1 µm
MAG: 724 x HV: 25.0 kV WD: 13.5 mm
e
Qt
Au
Py
Fe
3 µm
WD: 13.1 mm

Plate 2.10 (Previous Page): (A) Backscatter image of a free gold grain (white) within quartz (dark grey). Note small inclusion of gold within pyrite (light grey). (B) Reflected light photomicrograph of a fractured pyrite (Py) grain with galena (Ga) and sphalerite (Sp) occuring at the margins within quartz (Qt). Fine-grained gold occurs disseminated along fractures within the quartz, forming adjacent to, and as inclusions in, the pyrite. (C) Element map of (B) emphasizing the association between sulfide mineralogy and gold and illuminates the Ag-rich association with gold. (D) Embayed sphalerite grain (white) within pyrite (blue) which contains inclusions of gold (yellow) and is locally rimmed by what is interpreted as silver (green). An electrum grain (yellowish-green) is located adjacent to the pyrite. Note galena (pink) inclusions in pyrite, sphalerite and quartz. (E) Element map showcasing the relationships between sulfide mineralogy (galena – pink, lower left; pyrite – blue), electrum mineralization (or native silver; yellowish-green), sericite (pinkish-purple, upper right), carbonate (orange), and quartz (black).

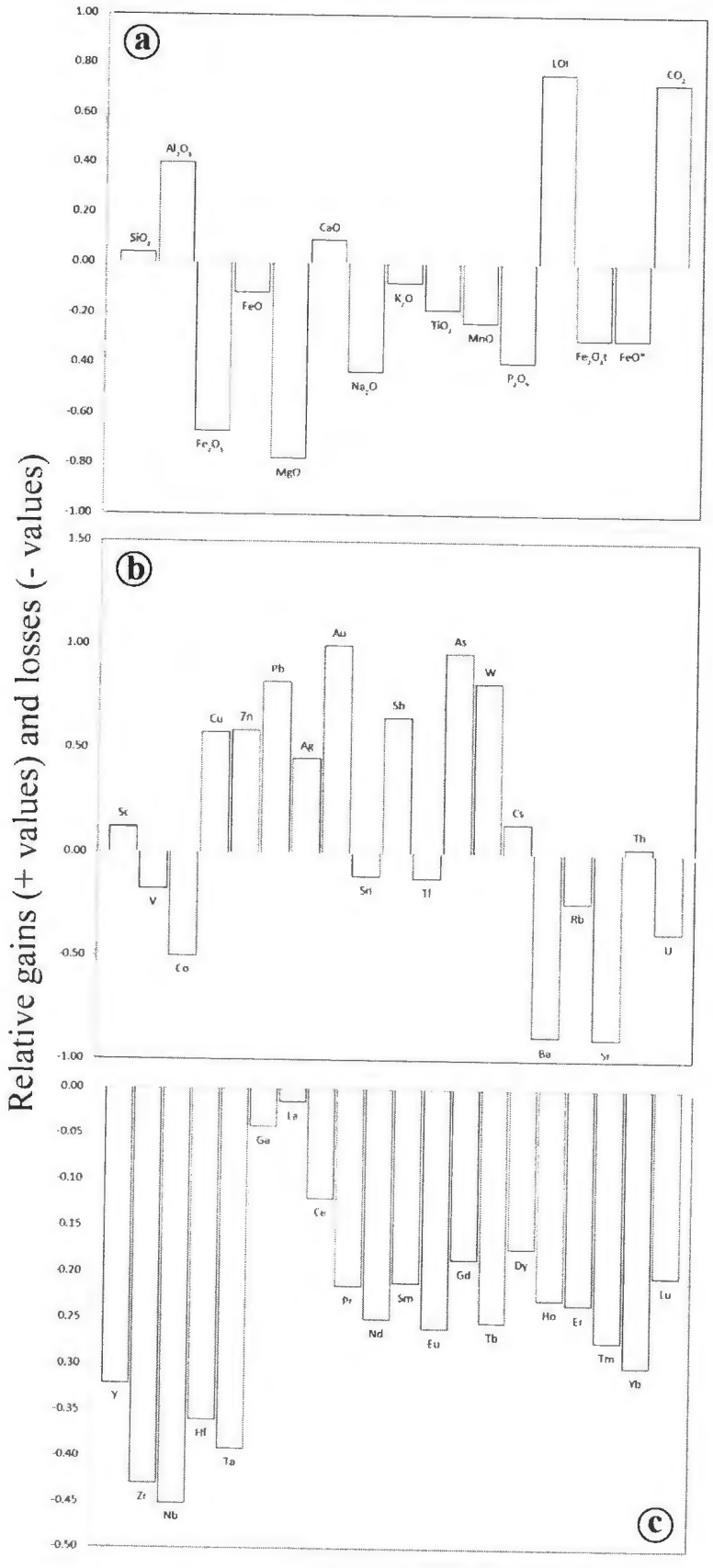

Figure 2.6: Relative elemental loss and gains in the Main River granodiorite during hydrothermal alteration at the Viking deposit. (A) Major elements and CO_2, (B) transition elements, base-metals, mineralization, and LILE, (C) HFSE and REE.

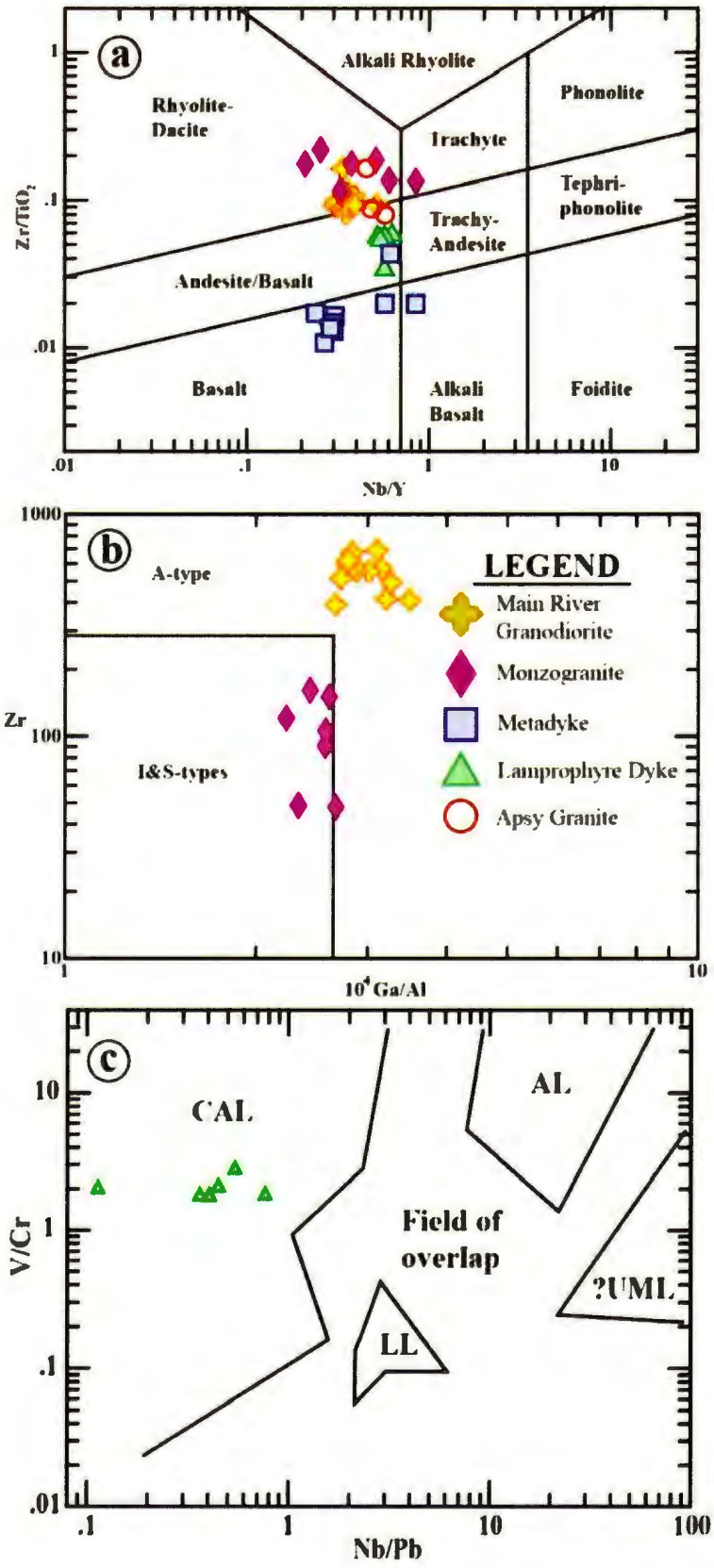

Figure 2.7: Trace element classification diagrams (A) Revised Winchester and Floyd (1977) after Pearce (1996) plot of the Viking deposit rock types and granitoid samples from the Apsy Granite. The rocks are generally subalkaline (Nb/Y<0.7) and plot as clusters except for the monzogranite sheets and metadykes. (B) Granitoid classification diagram after Whalen et al. (1987). The Main River Granodiorite contains elevated Zr and Ga/Al; characteristic of A-type granitoid geochemistry. The monzogranites contain lower, but ranging, values of Zr and Ga/Al and plot as I- and S-type granites. (C) Discrimination between the 5 lamprophyre branches of Rock (1991) using trace elements. The mesocratic dykes from the Viking deposit plot as calc-alkaline lamprophyres (CAL). Key: CAL – calc-alkaline lamprophyres, AL – alkaline lamprophyres, LL – lamproites, UML – ultramafic lamprophyres, and KIL – kimberlites. Note logarithmic scales. Fields of overlap represent areas of lower confidence classification.

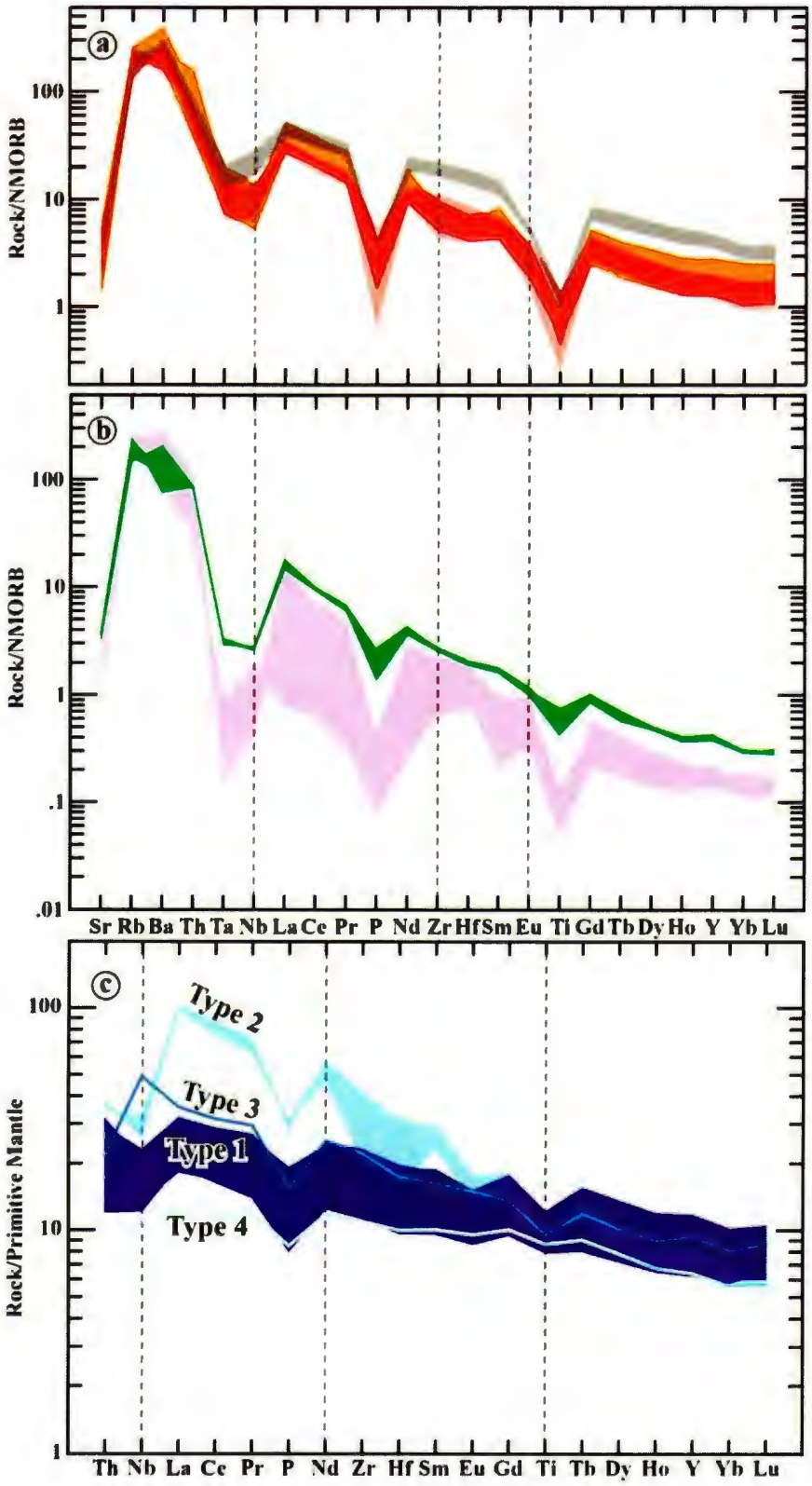

Figure 2.8: (A) Custom NMORB normalized multi-element plot (Sun and McDonough, 1989) for the Main River granodiorite (orange), Apsy Granite (red), and the Potato Hill Pluton (grey; see text for discussion). (B) Similar plot as (A) but for the monzogranite sheets (pink) and the mesocratic dykes (green). (C) Primitive mantle normalized multi-element plot for the metadykes. Type 1 is the most dominant with other types exhibiting variations in the LREE and HFSE.

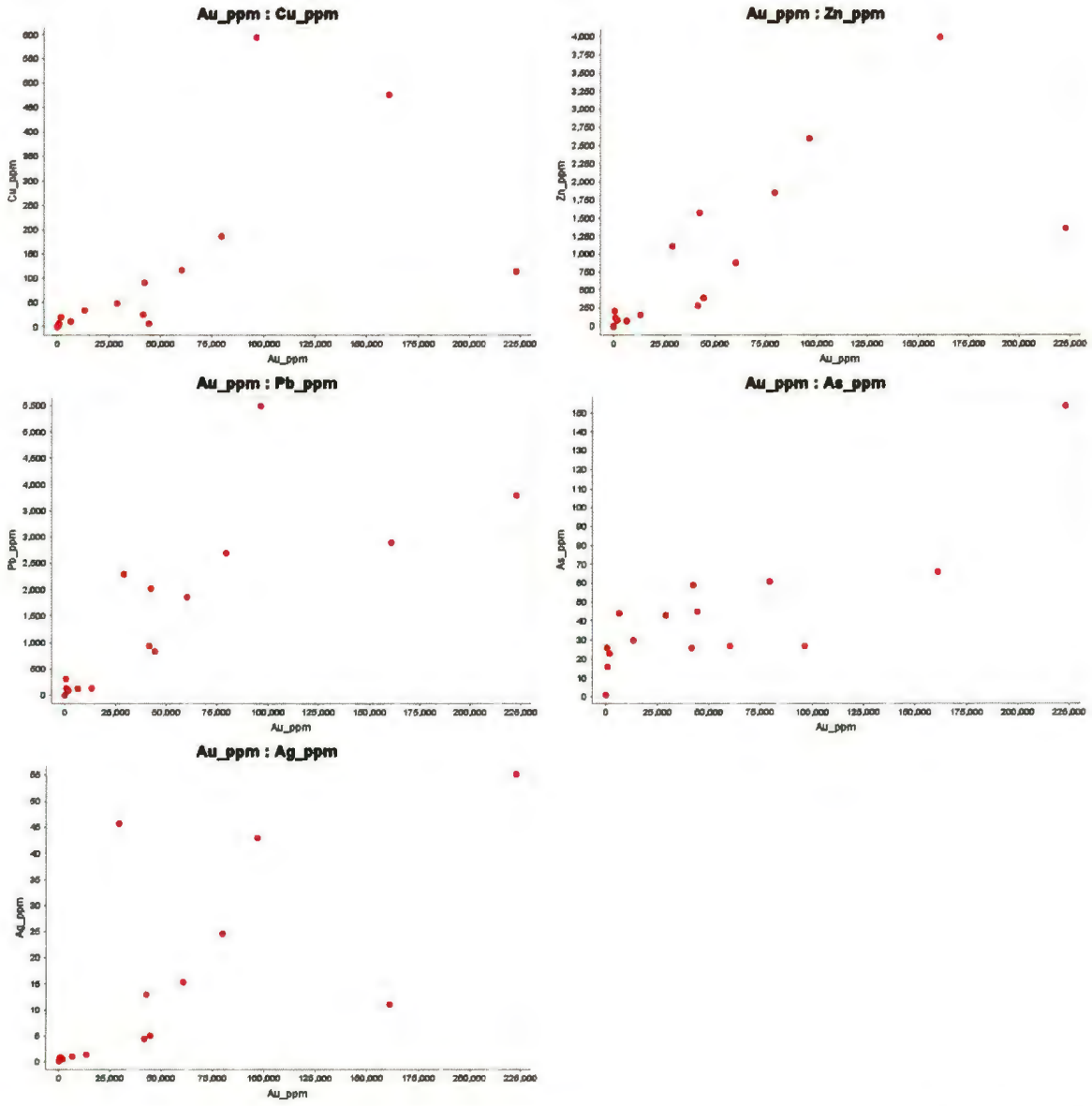

Figure 2.9: Gold correlation plots with Cu (correlation coefficient, R=0.6), Zn (R=0.7), Pb (R=0.7), Ag (R=0.6), and As (R=7).

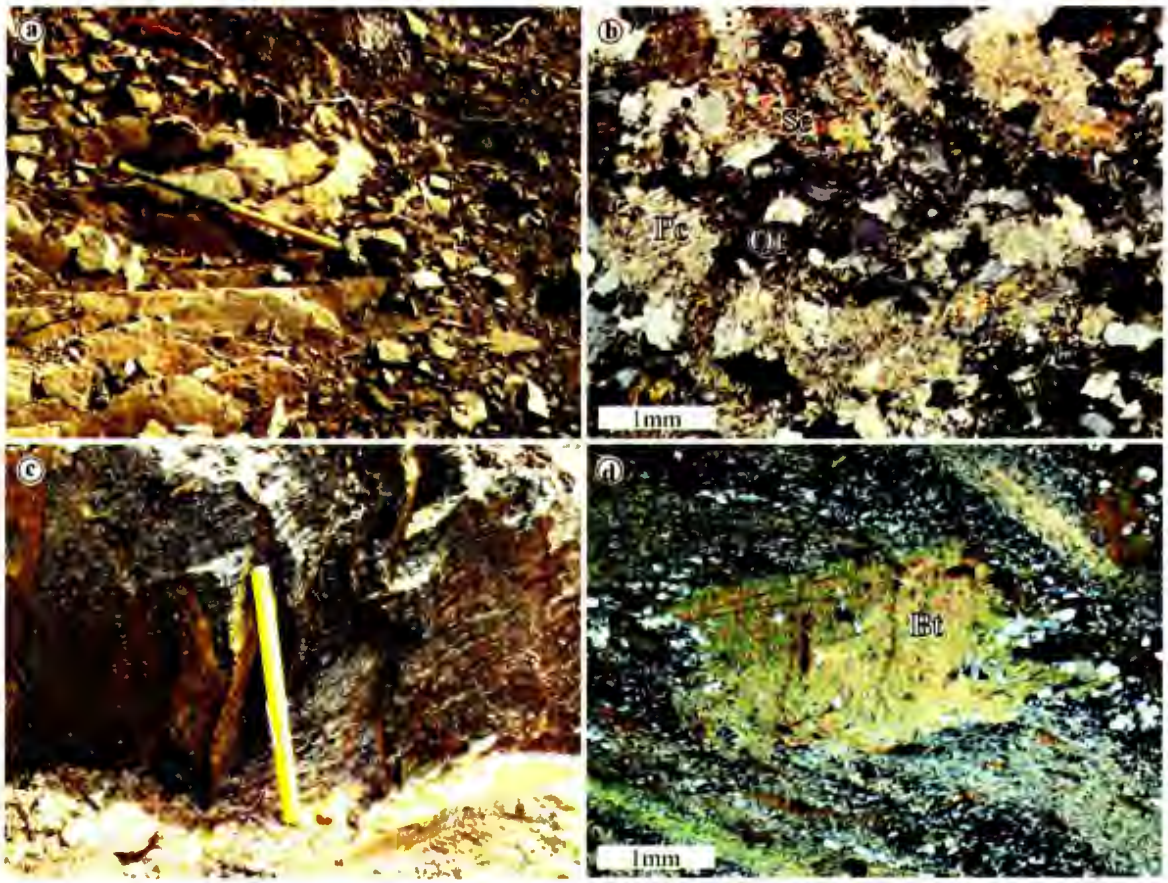

Plate 2.11: (A) Outcrop photo of the argon sample site (09MM113), a strongly sericite-altered and folded monzogranite within the Thor Trend. Sledge hammer is *ca.* 1.2 m in length. (B) Photomicrograph of the strongly sericite-altered monzogranite from (A). Feldspars are being replaced by fine-grained sericite (cross-polarized light). (C) Outcrop photo of the Forteau Formation phyllite with a shallowly east-dipping fabric and an upright foliation (following pen magnet). (D) Photomicrograph of the same phyllite displaying a rotated biotite porphyroblast with an internal strain fabric (lines running north to south through the biotite) cutting a foliation of quartz, sericite, and pyrite (cross-polarized light).

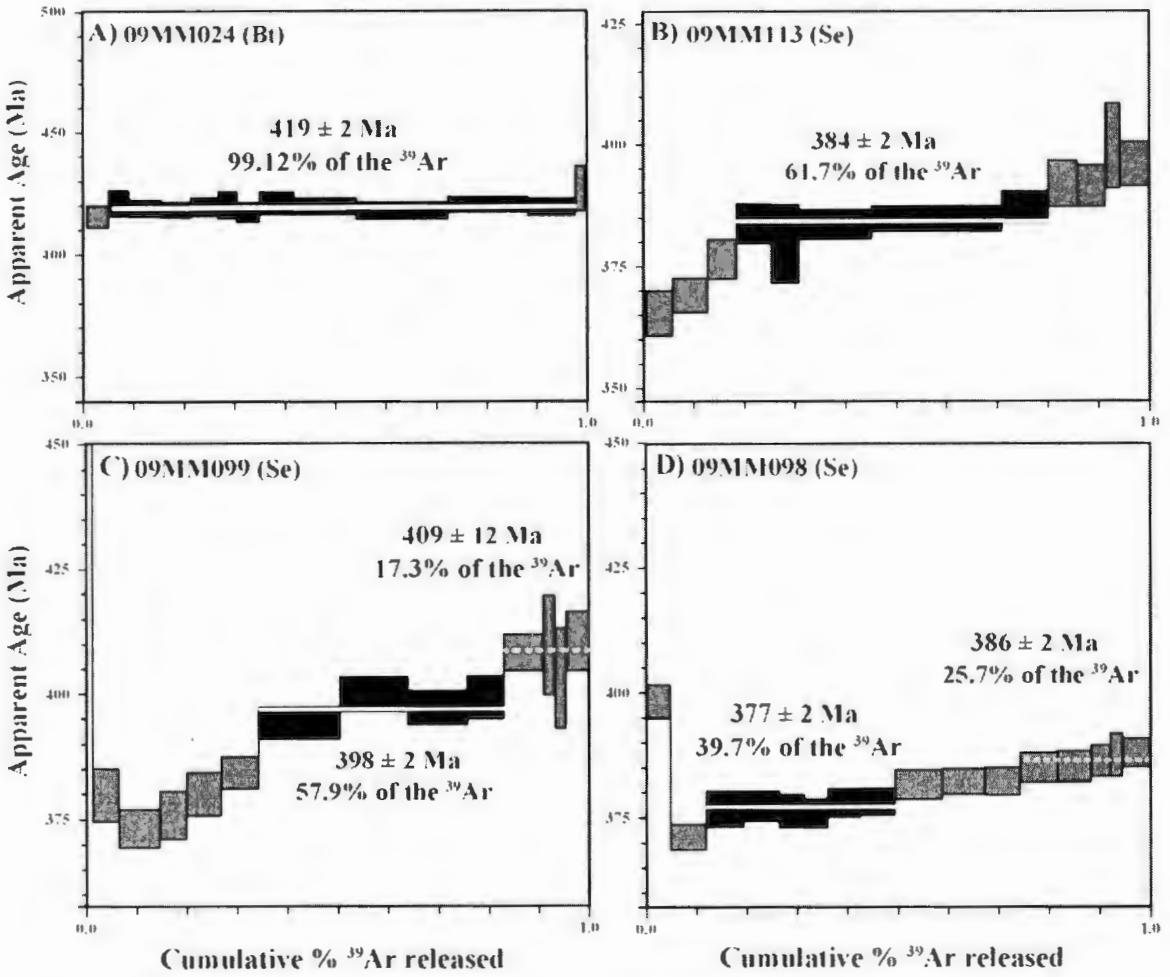

Figure 2.10: The ^{40}Ar-^{39}Ar release spectra for biotite (A) and sericite (B-D) plotted as apparent age (Ma) versus cumulative per cent ^{39}Ar released. Dashed white lines represent higher power pseudo-plateaus that may better approximate the primary argon cooling age of the sample. Solid white lines represent pseudo-plateaus that may suggest partial resetting of the ^{40}A-^{39}Ar systematics during later hydrothermal events. Gas steps used in the calculation of plateaus and inverse isotope correlation ages are black and those not used in calculations are grey.

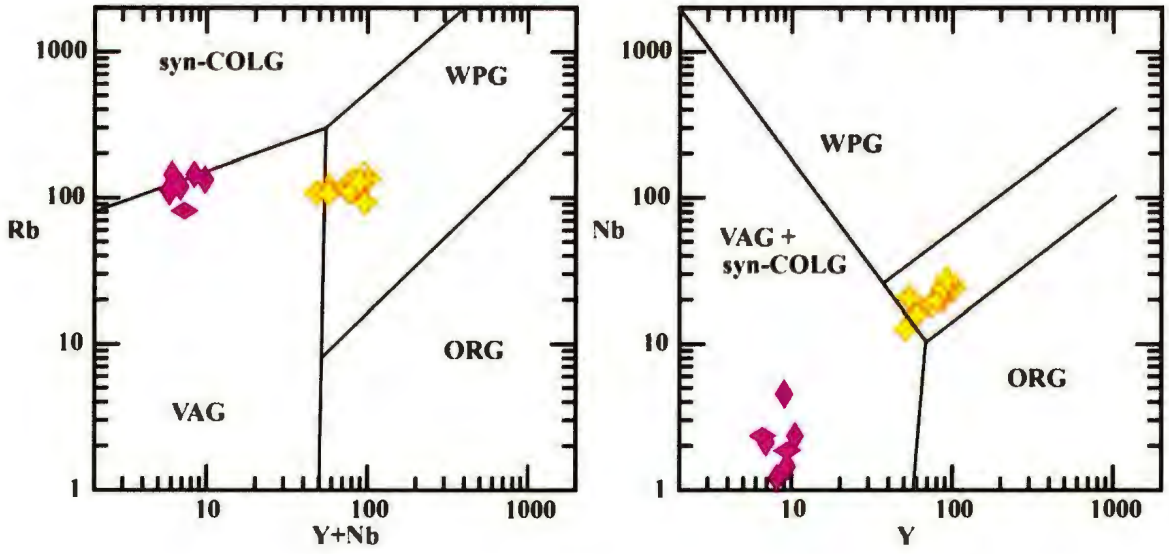

Figure 2.11: Tectonomagmatic discrimination diagrams after Pearce et al. (1984) for the granites of the Viking deposit. Since Rb is considered mobile, a more robust plot using Nb vs Y is given on the right. The Main River granodiorite exhibits within-plate to transitional trace-element geochemistry, whereas the monzogranite displays a volcanic-arc signature. Symbols as in Figure 2.7.

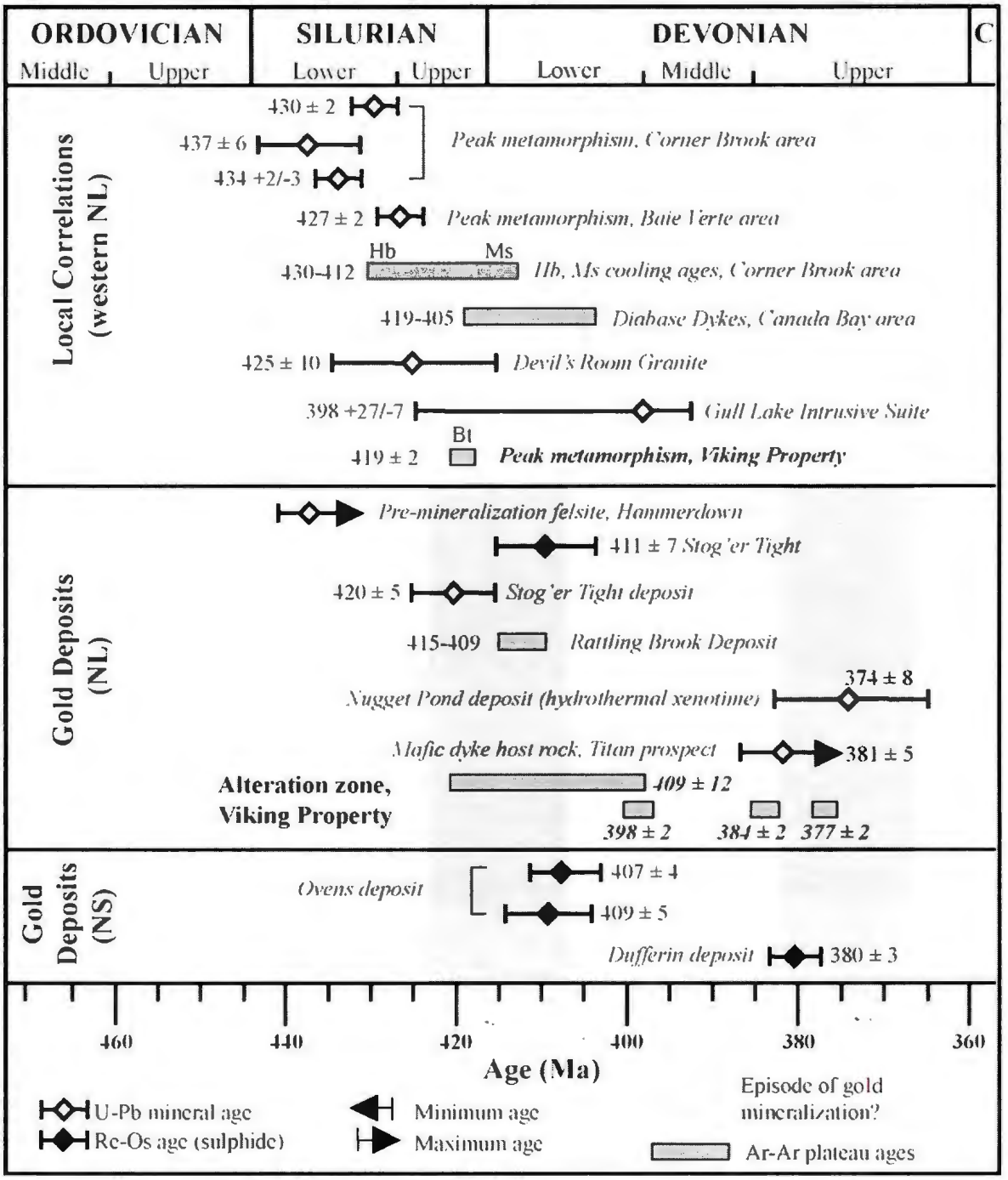

Figure 2.12: Summary chart modified after Kerr and van Breeman (2007) displaying the results of ^{40}Ar-^{39}Ar dating at the Viking deposit and its relationships with other geochronological constraints on the timing of gold deposition, metamorphism, and plutonism in the White Bay area of western Newfoundland, as well as ages for other orogenic gold deposits throughout Newfoundland and Nova Scotia.

Table 2.1: Assay results for 14 diamond-drill hole samples from the Thor vein. Gold concentration is given in parts per billion (ppb) and the remaining elements are reported in parts per million (ppm). UTM coordinates given in NAD27, zone 21 format and represent the collar locations from diamond-drill holes and not their surface projections. DL denotes the detection limit for the given element and n/a denotes not analyzed.

Sample		91254	91255	91256	91258	91260	91261	92308	92311	92312	91353	91359	91361	91383	58252
Drill Hole		08-VK-01	08-VK-01	08-VK-01	08-VK-01	08-VK-01	08-VK-01	08-VK-02	08-VK-02	08-VK-02	08-VK-03	08-VK-03	08-VK-03	08-VK-04	08-VK-05
From (m)		3.60	4.10	4.60	5.10	6.20	6.70	7.00	8.80	9.30	9.95	15.00	17.10	5.00	25.78
To (m)		4.10	4.60	5.10	5.40	6.70	7.70	7.40	9.30	9.80	10.45	15.50	17.40	5.39	26.70
Easting		500582	500582	500582	500582	500582	500582	500582	500582	500582	500582	500582	500582	500651	500582
Northing	DL	5504442	5504442	5504442	5504442	5504442	5504442	5504442	5504442	5504442	5504431	5504431	5504431	5504651	5504431
Au	5	222950	11438	11606	6523	79525	1829	12438	856	60331	589	161025	29100	13303	96575
Cu	1	114	7	25	11	187	20	91	7	117	4	477	48	34	595
Zn	1	1360	392	284	73	1855	85	1576	117	880	212	40000	1112	158	2600
Pb	2	3800	835	940	129	2700	94	2024	133	1859	315	2900	2300	134	5500
As	1	154	45	26	41	61	23	59	16	27	26	66	43	30	27
Ag	0.2	55.1	5.1	4.5	1.1	24.7	0.6	13	0.9	15.4	0.9	11.1	45.7	1.5	43
Cr	10	288	318	318	353	318	180	226	223	275	270	265	206	240	230
V	1	2	1	1	1	1	1	1	1	1	1	3	3	2	2
Co	1	3	2	1	1	3	2	2	1	1	3	4	5	2	3
Ni	1	6	5	4	5	7	3	6	4	5	5	8	11	6	6
Sn	10	10	10	10	10	10	10	10	10	10	10	10	10	10	10
Sb	6	5	5	5	5	5	5	5	5	5	5	5	5	5	5
W	10	10	10	10	10	10	10	10	10	10	10	10	10	10	10
Ba	10	10	10	10	15	10	32	11	10	10	12	12	17	14	11
Sr	1	5	1	2	3	2	9	4	2	3	5	12	35	8	5
La	10	10	10	10	10	10	10	10	10	10	10	10	10	13	10
Ce	10	22	10	14	20	37	10	24	10	30	18	126	119	43	59
Au/Ag		4	9	9	6	3	3	3	1	4	1	15	1	9	2

Table 2.2: Rock type, location (UTM, eastings and northings) and brief descriptions of the analyzed samples for ^{40}Ar-^{39}Ar thermochronology.

Sample	UTM co-ordinates[a]			Unit	Mineral	Description[b]	Integrated age (Ma)	Plateau age (Ma)
	Zone	Easting	Northing					
09MM024	21	500998	5504291	Labrador Group	Biotite	Fine-grained biotite porphyroblastic phyllite with strong upright foliation.	418.3 ± 1.5	419.4 ± 1.5
09MM113	21	500598	5504175	Main River Pluton	Muscovite	Strong sericite-pyrite-quartz altered and mineralized monzogranite in Thor Trend.	387.1 ± 1.4	384.3 ± 1.8
09MM099	21	500578	5504453	Main River Pluton	Muscovite	Strong sericite-pyrite-quartz altered and mineralized monzogranite in footwall to Thor Vein.	398 ± 1.4	398.9 ± 2.2
09MM098	21	500570	5504457	Main River Pluton	Muscovite	Strong sericite-pyrite-quartz altered and mineralized granodiorite in footwall to Thor Vein.	382.8 ± 1.1	377.1 ± 1.5

[a] - UTM co-ordinates given in NAD27 projection.

[b] - Field description supplemented by petrography.

CHAPTER 3

FLUID CHEMISTRY OF THE VIKING DEPOSIT GOLD OCCURRENCES

3.1 INTRODUCTION

This chapter presents fluid inclusion, stable and radiogenic isotope data collected from gold occurrences within the Thor trend and the Viking trend (Figure 2.2) at the Viking deposit. Fluid inclusions are believed to be the only direct evidence for the characteristics of the fluid during geological processes (van den Kerkhof and Hein, 2001). Fluid inclusion microthermometric analysis was completed on both mineralized and unmineralized quartz ± calcite veins in an attempt to constrain the characteristics of the mineralizing fluids and to determine pressure and temperature conditions at the time of fluid entrapment.

Sulfur isotope geochemistry has had a long history of application in the study of sulfide-bearing mineral deposits, beginning in the 1940s and 50s (Jensen, 1957, 1959; Kulp, *et al.*, 1956). *In-situ* SIMS analysis of sulfide $\delta^{34}S$ (pyrite, chalcopyrite and galena) within gold mineralized veins is presented in an effort to interpret a source for the sulfur. SIMS Analyses of galena for its Pb isotopic composition are presented to complement the $\delta^{34}S$ data. Model ages for galena formation using this data, and how they relate to the timing of gold mineralization at the Viking deposit (Section 2.9.3), are also discussed.

3.2 FLUID INCLUSIONS

Wilkinson (2001) states that the best evidence for a temporal genetic relationship between ore and gangue minerals is the occurrence of fine-grained ore mineral inclusions

within the gangue mineral itself. Petrographic and SEM analysis of high-grade samples from the Viking deposit (Section 2.4) indicate that gold grains are texturally and spatially associated with both the base metal sulfide assemblage and the quartz+sericite gangue (Plate 2.10). Fluid inclusions within the quartz gangue that is spatially associated with both "free" gold and gold-bearing sulfide minerals were targeted for microthermometric analysis. None of the fluid inclusions observed within the mineralized samples contained daughter ore minerals, although this relationship would also provide evidence for a temporal genetic relationship between ore and gangue minerals (Wilkinson, 2001). Microthermometric analytical procedures are outlined in Appendix A.4.

3.2.1 Fluid Inclusions Types

There are at least three types of fluid inclusions present within the mineralized and unmineralized quartz ± calcite veinlets distinguished on the basis of their inferred bulk composition and texture: (I) euhedral, mixed H_2O-CO_2 inclusions, (II) non-euhedral mixed H_2O-CO_2 inclusions, and (III) naturally decrepitated/leaked inclusions.

Type I: These inclusions are typically occurring as trails along secondary transgranular healed fractures but also occur proximal to Type II inclusions (Plate 3.1). They are small (1-5 μm) euhedral inclusions containing two liquid phases (liquid CO_2 + H_2O) and a vapour CO_2 phase at room temperature.

Type II: Are the most common fluid inclusions found within the veinlets. They are characterized by regular to irregular shapes, generally between 5 and 20 μm in size (Plate 3.2). They contain an undersaturated aqueous liquid phase and a two-phase bubble of liquid and vapour CO_2 at room temperature.

Type III: Represent secondary, naturally decrepitated inclusions which are typically 20 μm in size.

3.2.2 Microthermometry

A total of 55 fluid inclusions were analyzed, comprising 17 fluid inclusions assemblages (FIAs) from gold occurrences within the Thor and Viking trend. A fluid inclusion assemblage represents fluid inclusions of the same type that have similar Th_{TOT} (within ±10-15° homogenization temperatures) and were microthermometrically analyzed together. This indicates that the fluid inclusions represent the same trapped fluid. The procedures for calculating pressure, depth, and salinity is given in Appendix A.4.

Type I inclusions are typically more saline and have higher Th_{TOT} than those of Type II inclusions (Figure 3.1). Microthermometric analysis revealed significant variability between FIAs of Type II inclusions with respect to salinity and Th_{TOT}. The results of microthermometric analysis and pressure calculations are discussed below and the data is presented in Table D.1.

Type I inclusions were analyzed from samples taken from the Thor vein (09MM043; 3 FIA; n=8) and Valhalla mineralization (09MM167; 1 FIA; n=3), both of which are high-grade gold vein occurrences within the Thor trend. Homogenization temperatures were consistent (within ±10°C), ranging from 315-319°C for FIAs of Thor vein inclusions (FIAs 4a, 7a, and 6: Figure 3.1). Salinity calculations on these FIAs range from 8.3 to 9.4 wt% NaCl equivalent. Pressures of 1.7-2.5 kilobars (kbars) were calculated for the Type I fluid inclusions from the Thor vein which correspond to depths of 6-9 km. Type I Valhalla inclusions have a salinity of 8.3 wt% NaCl equivalent and a

Th_{TOT} of 317.6°C overlapping that of FIA 7a of the Thor vein inclusions. Pressure calculations indicate that pressures of 1.8-2.4 kbars correspond to depths of formation ranging from 6-8 km.

Mineralized Thor vein (09MM043) Type II inclusions have salinities ranging from 8.3-8.7 wt% NaCl equivalent and homogenization temperatures ranging from 280-313°C. The three analyzed FIAs (FIA 3, 4, and 7) fit into two categories. The data suggests a low temperature, low salinity FIA (FIA 7), and two overlapping higher temperature, higher salinity FIAs (FIAs 3 and 4, Figure 3.1). Pressure calculations suggest depths of formation of 6-10 km for the mineralized veins.

Analysis of Type II inclusions from the barren Thor vein (09MM105) showed that the three FIAs have identical salinity (8.7 wt% NaCl equivalent) but varying Th_{TOT} (FIAs 1, 2b, and 2c; Th_{TOT}=265-305°C). Salinity measurements for the barren Thor vein inclusions overlap those of the higher temperature and higher salinity mineralized zone Thor vein inclusions. However, their homogenization temperatures overlap (within ±15°C) with those of the lower temperature and lower salinity inclusions from the mineralized zone Thor vein. The barren Thor vein Type II inclusions returned depths of formation of 7-11 km (2.0-3.3 kbars).

Type II inclusions analyzed from high-grade mineralization to the north of the Thor vein (North Thor occurrence, 09MM108) yielded similar results to those of the high-grade Thor vein. Homogenization temperatures for FIAs 21 and 22 (265-273°C) overlap with FIA 7 (within ±15°C) of the mineralized Thor vein but salinity calculations indicate that FIA 22 has a much lower salinity (7.1 vs 8.1 wt% NaCl equivalent). FIA 22

overlaps well with the salinities of both the mineralized and barren Thor vein samples, particularly FIA 2b (Figure 3.1). Pressure calculations indicate a depth of 6-9 km (1.8-2.8 kbars) for the formation of the high-grade mineralization observed at the North Thor occurrence.

Type II inclusions from Valhalla mineralization display variability of homogenization temperatures and salinities within the FIAs. Homogenization temperatures are all within ±10°C indicating that the analyzed fluid inclusions are a part of the same FIA and likely represent the same trapped fluid. The Th_{TOT} for FIA 15 (237°C) are the lowest observed within the dataset, but the salinities overlap with those from the other gold occurrences. FIA 17 gave homogenization temperatures which were 30°C higher than those from FIA 15; however, salinities for this assemblage were only approximately 1 wt% NaCl equivalent lower. These differences may indicate that these FIAs represent discrete fluids. Pressure estimates suggest a depth of formation of 8-10 km (2.4-2.9 kbars).

Three fluid inclusion assemblages of Type II inclusions from a sample of high-grade stockwork mineralization from the Viking trend (09MM081) contain some of the least saline fluid inclusions (e.g. FIA 11 and 13), and FIA 13 displays the highest homogenization temperatures (316-320°C) recorded for the Viking deposit occurrences. There is a linear trend that can be observed from Figure 3.1 for the FIAs of this sample. With increasing salinity (from 6.2 to 8.3wt% NaCl) there is a decrease in the temperature of homogenization from 320 to less than 260°C. The Viking trend stockwork sample also

has the shallowest implied depth of formation of 4 km (4-10 km range) with equivalent pressures of 1.4-2.9 kbars.

3.3 SULFUR ISOTOPES

The $\delta^{34}S$ values of 60 *in-situ* sulfur isotope analyses conducted by SIMS are listed in Table E.1. Multiple grains of the same sulfide mineral within each sample were analyzed, in order to delineate any possibly heterogeneity. The measured $\delta^{34}S$ were all positive and averaged 7.7‰. There is a mineralogical trend, with isotopic heaviness increasing between chalcopyrite and pyrite and galena (Figure 3.2).

A total of 21 analyses were completed on pyrite grains from the Thor Trend. The average $\delta^{34}S$ for pyrite within the high-grade Thor Vein was 6.7 ± 0.2‰ (1σ) with values ranging from 4.7 to 8.2‰. Pyrite from lower grade intercepts of the Thor Vein returned $\delta^{34}S$ values between 3.2 to 10.4‰ with an average of 7.0 ± 0.3‰ (1σ) (Plate 3.3). The $\delta^{34}S$ values for high-grade mineralization north of the Thor Vein range from 2.0 to 4.2‰, averaging 2.6 ± 0.3‰ (1σ).

A total of 11 analyses were completed on galena. A range of $\delta^{34}S$ of 10.7 to 15.6‰ (average = 12.9‰) is present in the high-grade Thor Vein. Galena from mineralization north of the Thor Vein returned the highest $\delta^{34}S$ values among mineralized samples, ranging from 15.6 to 20.9‰ (average = 19.3‰; Plate 3.4).

The $\delta^{34}S$ composition of chalcopyrite grains within the Thor Vein ranged from 4.7 to 8.9‰ with an average of 7.1 ± 0.3‰ (1σ). This average overlaps with the $\delta^{34}S$ composition of pyrite observed within the same sample (09MM043). A sample of chalcopyrite from moderate to high-grade mineralization outboard of the Thor Trend was

analyzed for comparison, and returned $\delta^{34}S$ values ranging from 1.0 to 7.7‰. These chalcopyrite analyses constituted the lightest $\delta^{34}S$ compositions present in the sample set (Plate 3.5).

3.4 LEAD ISOTOPES

The Pb isotope compositions for 24 *in-situ* galena samples from gold occurrences at the Viking deposit are listed in Appendix F. The samples were selected to ascertain if there were substantial differences between the Pb isotope signatures of galena grains within a sample, and signatures from the different occurrences. A total of 7 measurements were made from the high-grade Thor vein (09MM043), 10 measurements from a lower-grade quartz vein offshoot from the Thor vein (09MM057), and 7 from the stockwork-style mineralization at the Viking trend occurrence (09MM081).

The Pb isotope data was reduced using ISOPLOT (Ludwig, 2003) which calculated model ages and preformed regressions. The Pb model age for stockwork style veining at the Viking Trend occurrence was *ca.* 483 Ma, whereas galena from the Thor Vein and its lower grade offshoots yielded model ages of *ca.* 423 and 383 Ma, respectively.

$^{206}Pb/^{204}Pb$ ratios overlap within error between samples. When error is taken into account the apparent spread between the samples with respect to ^{207}Pb is also negligible. The Pb isotope ratios have a restricted range of values, all which fall near the 0.4 b.y. isochron on Zartman and Doe's (1981) Pb-Pb growth curves (Figure 3.3). The samples plot close to the orogene growth curve suggesting they were influenced by both mantle and crustal Pb sources (Zartman and Doe, 1981).

3.5 FLUID CHEMISTRY OF WHITE BAY GOLD DEPOSITS

Fluid inclusion, as well as sulfur and lead isotope, data are available for some of the gold prospects and showings of the White Bay area (Currie, 2004). Currie (2004) compared seven auriferous showings hosted by felsic volcanic and fine-grained sedimentary rocks of the Sops Arm Group, as well as samples from the Jackson's Arm area. The main conclusions of this work is that the mineralization was structurally controlled and formed during the Silurian to Carboniferous from low salinity (<6 wt% NaCl) hydrothermal fluids at temperatures of 200 to 350°C. For the West Corner Brook prospect, the Browning Mine, and the Simms Ridge prospect, $\delta^{34}S$ ratios ranged from 0.0 to 8.8‰ falling within the $\delta^{34}S$ range of most orogenic systems (Hofstra and Cline, 2000). Sulfur isotope data for the Rattling Brook mineralization are not available.

Analysis of fluid inclusion assemblages from the Thor Vein within the Thor Trend at the Viking deposit indicates the presence of at least 3 types of inclusions. The Th_{TOT}, as well as salinities for Type I and II inclusions, overlap with those for the West Corner Brook prospect, the Browning Mine, the Simms Ridge prospect, and mineralization hosted by the Apsy Granite (Rattling Brook/Jackson's Arm area). The $\delta^{34}S$ values, for Thor Trend sulfides, also overlap those seen in the Sops Arm Group showings (-0.9 to 9.3‰).

3.6 DISCUSSION

Fluid inclusion data derived from microthermometric analysis on both gold mineralized and barren samples from the Viking deposit provide insight into the fluids responsible for the precipitation of gold-bearing quartz±calcite veins and the associated

lower-grade sericite+pyrite alteration halo. A key question in many fluid inclusion studies of orogenic gold deposits is how do the observed inclusions relate to the gold depositing event? There is a high possibility of overprinting by later, unrelated fluids in these deposits (e.g. Kerrich and Cassidy, 1994) and lower T_h inclusions are commonly paragenetically late. The purpose of collecting microthermometric data during this study was to determine the pressure and temperature conditions of the formation of these gold occurrences and to compare these data with the current understanding of orogenic gold systems.

Figure 3.4 is a compilation of homogenization temperature and salinity data from various ore deposit types (after Roedder, 1984). The homogenization temperatures and salinities determined from the Viking deposit gold occurrences overlap the field for orogenic gold deposits.

Fluid inclusion microthermometric data can also be used to identify and constrain physical processes of fluid modification. Two processes that commonly provide the necessary conditions for effective ore mineral precipitation are boiling and fluid mixing (Wilkinson, 2001). Figure 3.5 schematically shows typical trends in T_h-salinity space caused by various fluid evolution processes (Shepherd, *et al.*, 1985). Boiling results in the production of vapour which causes partitioning of salts into the liquid-like phase resulting in a more saline residual liquid (Wilkinson, 2001). Adiabatic expansion may promote a decrease in temperature. When this is applied to the Viking gold occurrence microthermometric data, similar trends can be observed for FIAs from the Viking trend, Valhalla, and North Thor samples. Higher temperature, low salinity FIAs are present and evolve towards lower temperature, higher salinity FIAs (Figure 3.1). Mineralized Thor

vein fluid assemblages show a reverse trend, with high temperature and high salinity FIAs evolving to lower temperature and lower salinity FIAs. This trend resembles the process of boiling (Figure 3.5) generating low salinity, CO_2-bearing inclusions that are present as 3 phase inclusions (Type II) in these samples (Plate 3.2). However, with the tight salinity values quantitatively distinguishing between boiling or surface dilution trends is difficult (Figure 3.5). The process of simple cooling is interpreted from the results of the barren Thor vein FIAs. These FIAs evolve from higher temperature to lower temperature without change in salinity.

Pinpointing which FIA best correlates with episodes of gold mineralization (i.e. high temperature/low salinity or low temperature/high salinity) has proven difficult. Because the microthermometric analysis was conducted in free gold-bearing quartz gangue proximal to gold-bearing sulfides, the argument could be made that these data represent the window of temperature and salinity conditions at the time of gold deposition. It is possible, however, that lower temperature FIAs represent paragenetically late episodes of fluid overprinting related to protracted hydraulic fracturing and movement along the DVFS. Type I inclusions are found as transgranular trails that indicate a paragenetically late formation, but have high homogenization temperatures and salinities for the Thor vein and Valhalla samples. This may indicate one of two scenarios, either they correspond to a later high temperature thermal event or there were errors in the determination of T_h owning to their very small size.

The pressure-temperature conditions obtained from FIAs suggest that orogenic gold formed over a wide range of depths in the crust (e.g. the crustal continuum; Groves, 1993). Results from pressure calculations completed from the Viking gold occurrences

indicate that pressures ranged from 1.4 to 3.3 kbars corresponding to depths ranging from as shallow as 4km (one measurement), to as deep as 11km, and with an average depth of 8km.

Sulfur isotope ratios suggests that the $\delta^{34}S$ values for the sulfides within the Viking gold occurrences are generally heavier than sulfur from purely magmatic origins, which are typically in the range of $0 \pm 3‰$ (Ohmoto and Rye, 1979). The results suggest there is a uniform, heavy sulfur source with an uncertain origin. Normal granitoids would be unlikely to supply such a heavy sulfur source.

Pb isotope data suggest that Pb is from an orogene-like source; however, the actual source is uncertain. Different model ages from the Viking deposit samples suggest that Pb was scavenged from multiple Pb reservoirs (i.e. different aged source rocks). Pb isotope values thus represent variable mixtures of two or more Pb sources. A spatial and textural relationship between galena and gold in mineralized samples suggests they precipitated together but their origins are unkown. Therefore, the model ages have no explicit meaning for dating these samples.

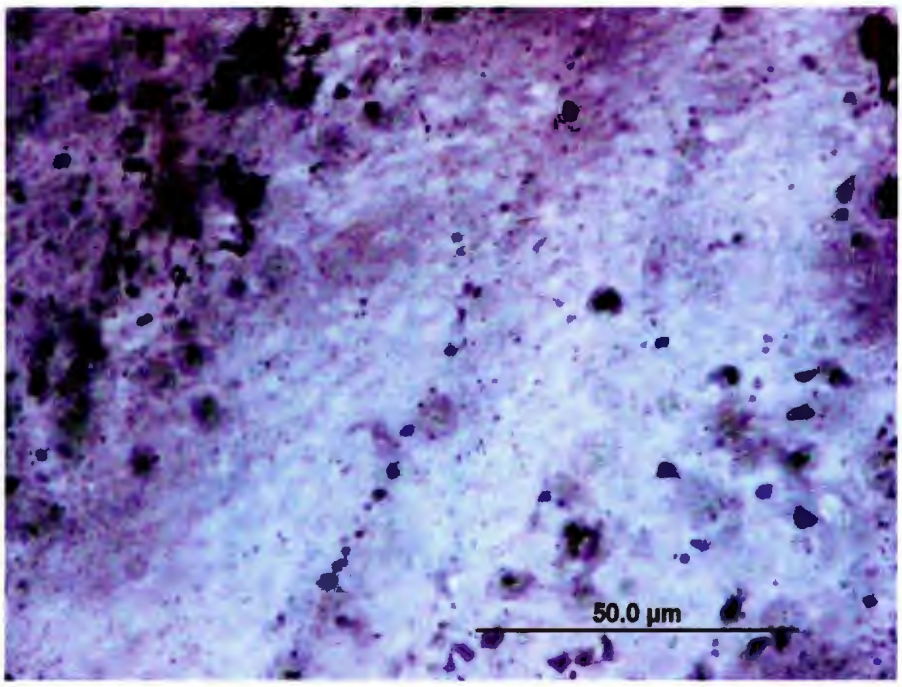

Plate 3.1 Photomicrograph of a transgranular trail (center) of Type I fluid inclusions at 6.6°C (100x magnification, 09MM043).

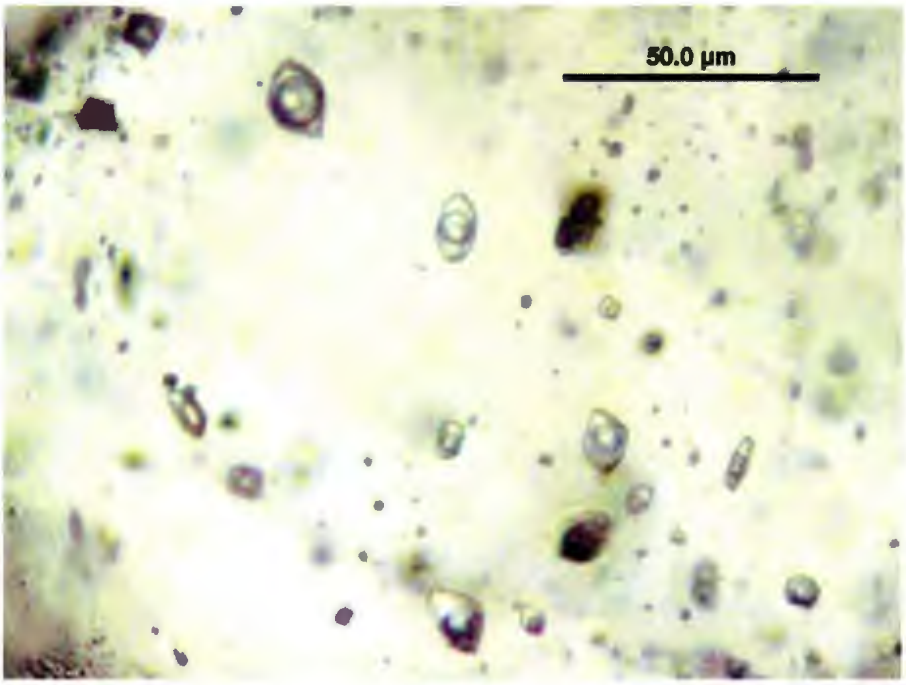

Plate 3.2 Photomicrograph of aqueous carbonic, three-phase, Type II fluid inclusions at 6.6°C from the mineralized Thor vein (09MM043, 100x magnification).

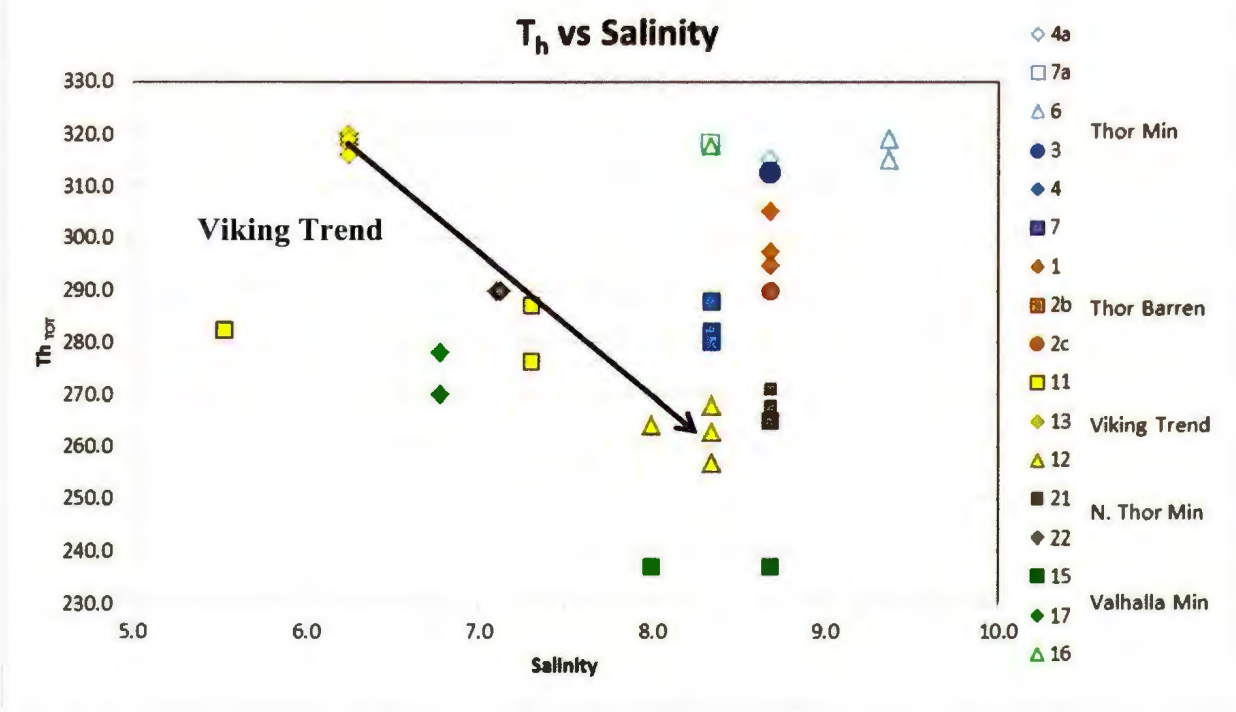

Figure 3.1: Homogenization temperature (°C) versus salinity (wt% NaCl equivalent) plot of microthermometric data for the FIAs analyzed on samples from the Viking deposit. Type I inclusions are open (e.g. 4a) and Type II inclusions are colored. Colors represent samples and shapes represent individual FIA. Viking Trend analyses indicate an interpreted boiling trend marked by black arrow. Key: blue = Thor vein mineralized (09MM043), orange = Thor vein barren (09MM105), yellow = Viking trend stockwork (09MM081), grey = North Thor mineralized (09MM108), and green = Valhalla mineralized (09MM167).

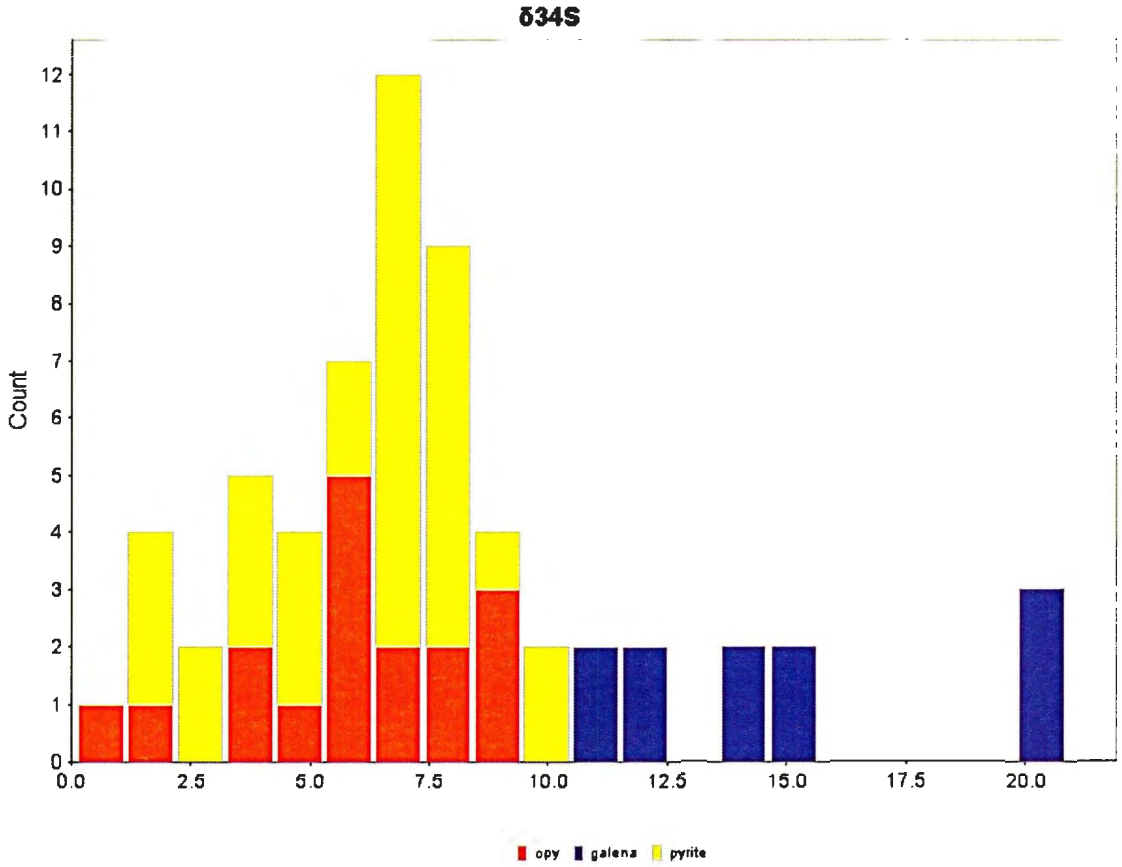

Figure 3.2: Histogram of $\delta^{34}S$ values of sulfides from the Viking deposit gold occurrences. Fractionation factors for chalcopyrite (cpy) and pyrite generally overlap but note the high and heterogeneous values for galena.

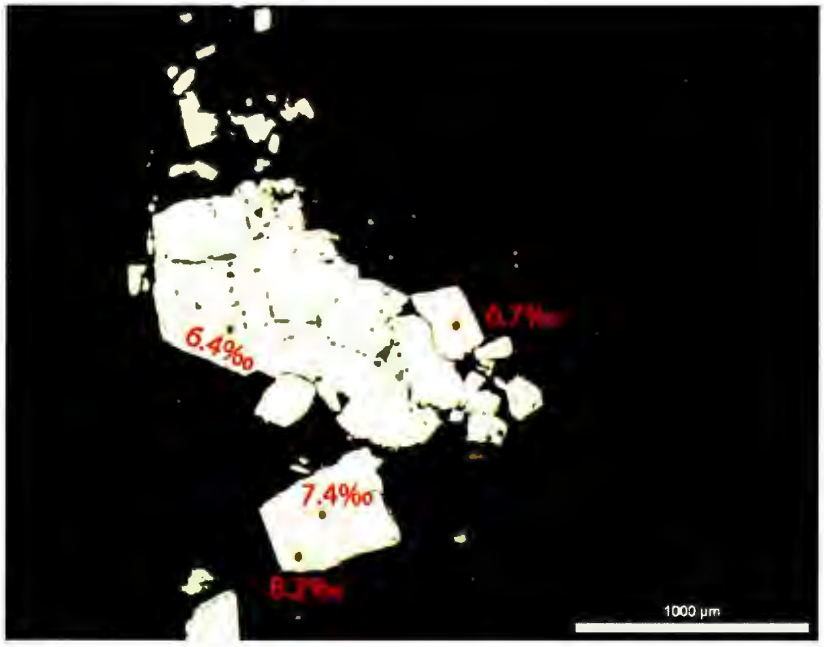

Plate 3.3: Sulfur isotope values from pyrite (dark pits) hosted by quartz (dark grey) from the Thor Vein (09MM043). Average $\delta^{34}S$ for sulfur in these samples is 6.7‰.

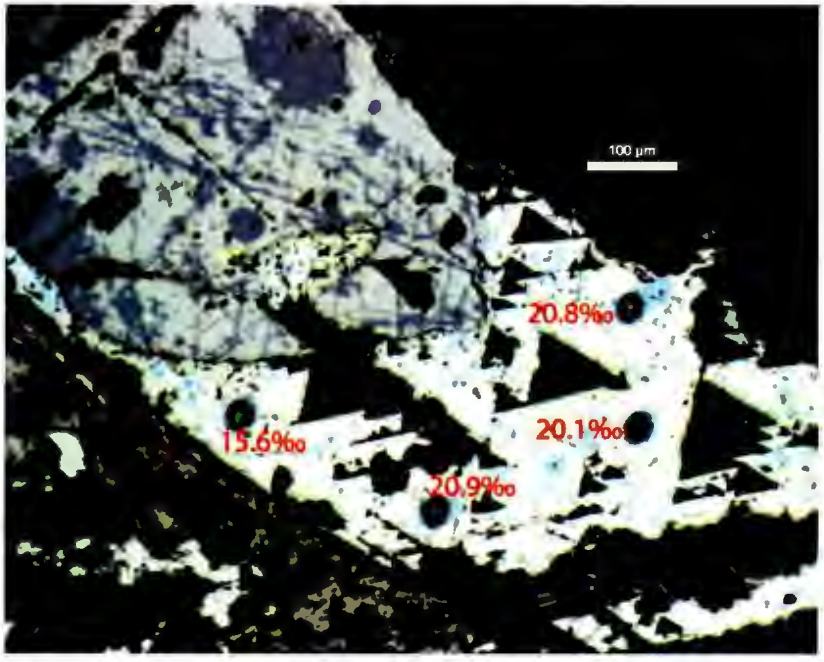

Plate 3.4: Sulfur isotope values from galena (triangle pitted) associated with sphalerite (grey, upper left) hosted by quartz (dark grey, upper right) from high-grade mineralization located north of the Thor Vein. $\delta^{34}S$ values for these galena's are the highest observed within the sample set.

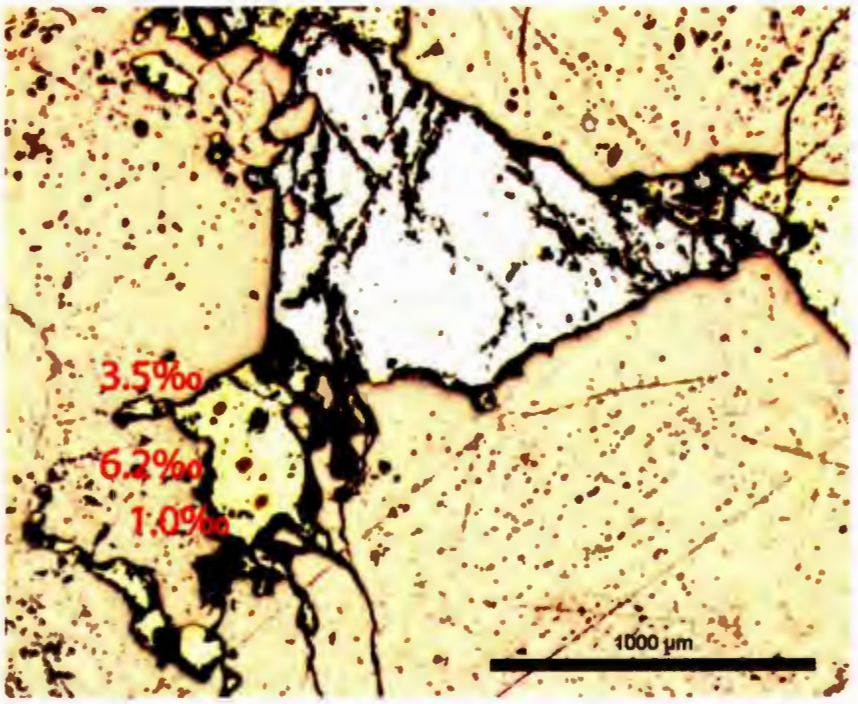

Plate 3.5: Isotopically light chalcopyrite (yellow) with galena (grey, unanalyzed) from the Viking trend. This sample has the lightest $\delta^{34}S$ compositions observed from the Viking gold occurrences.

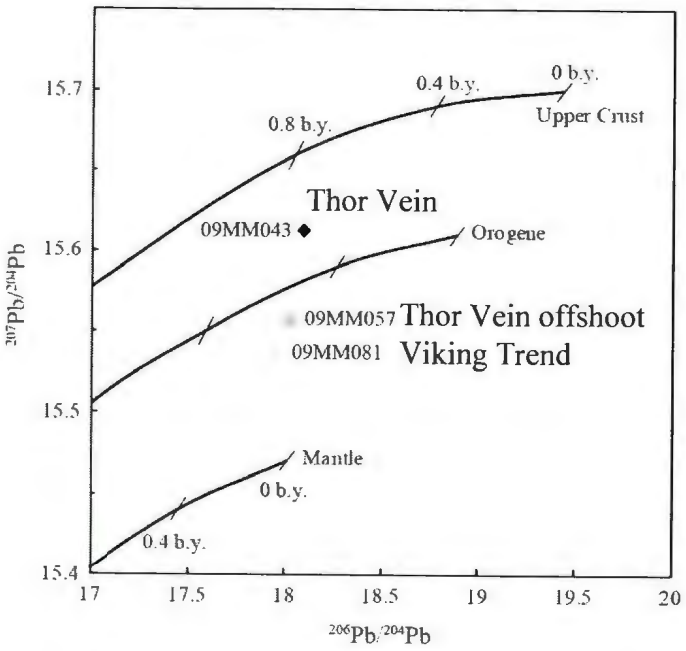

Figure 3.3: Average lead isotope compositions for Viking deposit galenas compared to growth curves summarized by Zartman and Doe (1981). Sample numbering is as follows: 09MM043 = Thor Vein; 09MM057 = Thor Vein offshoot; and 09MM081= Viking Trend.

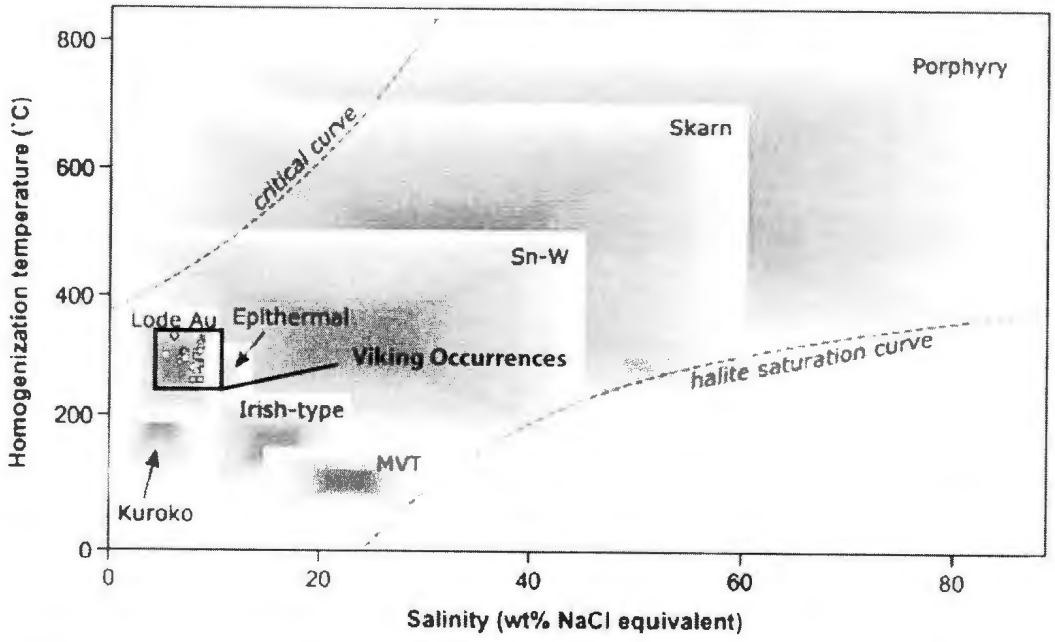

Figure 3.4: Homogenization temperature versus salinity diagram depicting typical ranges for inclusions from different ore deposit types. The Viking deposit gold occurrence microthermometry data has been overlain and highlighted in the black box. Modified after Roedder (1984).

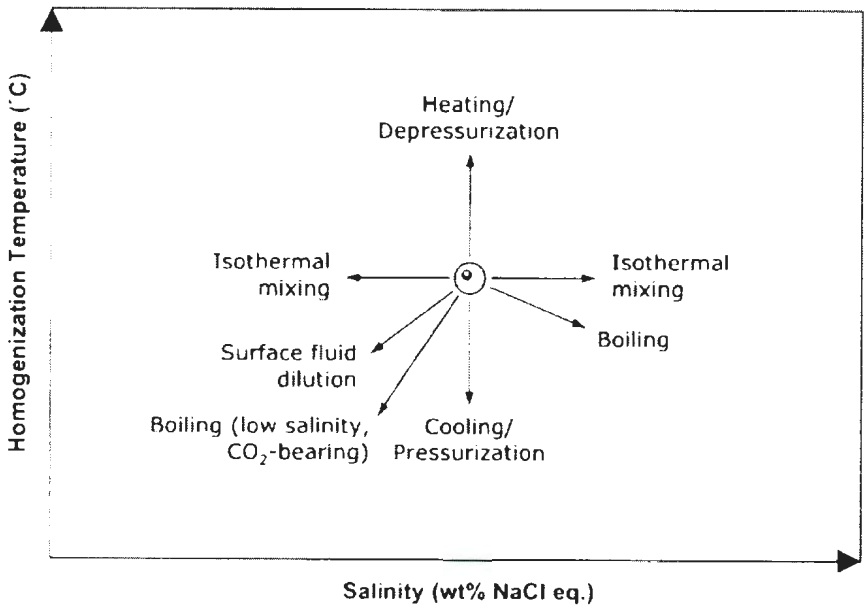

Figure 3.5: Schematic diagram showing typical trends in T_h-salinity space due to various fluid evolution processes (Shepherd *et al.*, 1985).

CHAPTER 4

CONCLUSIONS

4.1 INTRODUCTION

The ultimate aim of the research was to: document the Viking gold deposit using geology, geochemistry, and geochronology; understand the controls on mineralization; place the deposit within a spatial and temporal context with regards to other gold prospects in the region; and to create a genetic model for the mineralization.

4.2 OROGENIC GOLD MODEL

Table 4.1 outlines the major characteristics of orogenic gold deposits and compares them with features observed at the Viking deposit. It is readily apparent that the Viking deposit shares many characteristics with the orogenic gold model, as do most other White Bay occurrences in the Sops Arm Group based on the available information. Figure 4.1A schematically displays the tectonic setting of gold-rich epigenetic deposits (Goldfarb *et al.*, 2005). The Viking mineralization is associated with lower order structures proximal to a major compressional structural break (e.g. the DVFS) and is proximal to synchronous granitic plutons (e.g. Devil's Room Granite). Microthermometric analysis of mineralized samples indicates a depth of formation ranging from 4-11 km with corresponding temperatures of 237-320°C. These data would classify the mineralization as being mesozonal in the scheme of Goldfarb *et. al.* (2005) (Figure 4.1B).

4.3 RECOMMENDATIONS

This study has focused on documenting the lithogeochemistry of host rocks and determining the timing of gold mineralization at the Viking deposit. Further examination would benefit from the collection of O, C, and H stable isotope data, which may give indications on possible fluid source reservoirs. Similar deposits elsewhere in the Newfoundland Appalachians (e.g. Hammer Down, Ritcey, *et al.*, 1995) are interpreted to have fluids derived from a mixed origin but dominantly from a metamorphic reservoir. Such analysis on Viking samples would provide evidence for or against fluids which are magmatic or metamorphically (or both) derived. Since gold has been observed as inclusions within pyrite (Section 2.4), if this pyrite was to contain sufficient concentrations of Os, then acquiring a Re-Os model age might substantiate the *ca.* 409 Ma age for gold deposition as acquired by argon thermochronology (Section 2.9.3). Acquiring precise U-Pb geochronology for the monzogranite and lamprophyre dykes would better constrain the maximum age of mineralization.

4.4 CONCLUSIONS

1) Gold mineralization in the White Bay area is interpreted to have formed in response to protracted strike-slip movement along the Doucer's Valley Fault System during the Late Silurian to Early Devonian (Kerr, 2005, 2006a; Kerr and van Breemen, 2007; Kerr, *et al.*, 2006; Saunders and Tuach, 1988, 1991; Smyth and Schillereff, 1982; Tuach, 1987; Tuach and French, 1986). The highest grade mineralization appears to be hosted by east-west trending shear zones that are interpreted to be R2 shears.

2) Gold-electrum mineralization at the Viking deposit is hosted by quartz ± calcite + sulfide veins and small veinlets within the surrounding sericite-altered host rocks. The veins exhibit a simple sulfide assemblage of pyrite, galena, sphalerite, and chalcopyrite. Gold-electrum mineralization in the veins occurs as both 'free' blebs and as inclusions within sulfides that are associated with quartz.

3) The host rocks to the gold mineralization have geochemical signatures as follows: the Main River granodiorite exhibits similar chemistry to other Grenvillian granitic plutons that have intruded the external LRI, and has been crosscut by I-type monzogranites similar to the equigranular granites within the Potato Hill Pluton (Owen *et al.*, 1992). Calc-alkaline, strongly altered and mineralized, lamprophyre dykes are associated with the mineralized veins.

4) Hydrothermal alteration is most intense proximal to quartz veins and shear zones and decreases in intensity away from these shear zones (i.e. is spatially zoned). The alteration assemblage is composed of muscovite (sericite), pyrite and quartz.

5) The timing of final peak metamorphism is constrained at *ca.* 419 Ma from a ^{40}Ar-^{39}Ar cooling age of syn-late kinematic biotite porphyroblasts in the adjacent Labrador Group. This age corresponds to the waning stages of the Silurian Salinic orogeny and suggests that the gold-bearing/transporting fluids were derived via metamorphic processes (i.e. are orogenic) that were ongoing in the White Bay region through the Late Silurian.

6) Argon thermochronological analysis of sericite from a shear zone proximal to the Thor Vein yielded an age of *ca.* 409 Ma. Textural evidence suggests that gold is spatially associated with the sericite alteration, and thus *ca.* 409 Ma may also

represent the timing of gold deposition. Younger thermochronological ages are thought to represent resetting of hydrothermal sericite through the Early Devonian.

7) The presence of tensional, gold mineralized veins in competent rocks suggests depth of formation in excess of 3km. Fluid inclusion data supports this interpretation. These veins formed at pressures corresponding to 4 to 11 km depth at temperatures ranging from 237 to 320°C.

8) A lack of magmatic-related elements (e.g. Hg), along with $\delta^{34}S$ values in the mineralized zones and host rocks that are heavier than typical magmatic sulfur, argues against an intrusion-related style of mineralization.

9) Although the actual source of Pb is uncertain, Pb isotope data suggests an orogene-like source where Pb was scavenged from multiple reservoirs.

10) Fluid inclusion data suggests that boiling, and possibly mixing, accompanied by changes in temperature lead to the precipitation of gold from the ore-bearing fluid. Evidence suggests that there were multiple generations of fluids that are likely metamorphic in nature.

11) From an exploration perspective, zones of intense sericite + pyrite + quartz alteration proximal to shear zones are a primary target for identification of high-grade gold mineralization at the Viking deposit.

Table 4.1: Summary of the major characteristics of orogenic gold deposits in comparison to the main characteristics of the Viking deposit gold mineralization.

Major Characteristics of Orogenic Gold Deposits (Goldfarb et al., 2005)	**Characteristics of the Viking Gold Mineralization**
Setting:	
Related to major structural breaks	Doucer's Valley fault system
2^{nd}-3^{rd} order structures	Shearing and veining
Host Rocks:	
Mineralization occurs in all rock types	Hosted primarily by intermediate megacrystic granodiorite
Ore Mineralogy:	
Quartz ± carbonate veins	Are present as predominant host
Py, gal, cpy, sph common in veins	Typically 3-5% by volume
Anomalous Hg in deep deposits associated with sph	No Hg reported (not hypozonal)
PGE enrichments where fluids interact with mafic oceanic rocks	Unknown PGE contents
Au:Ag of 5:1 typical	Average 5:1
High Au grades associated with carbonaceous rocks	Intermediate carbonate-rich mineralized lamprophyre dykes
Alteration Mineralogy:	
Metamorphic minerals overprinted by hydrothermal alteration minerals	Observed
Alkali metasomatism: sericitization common	Most intense proximal to mineralized vein systems and shear zones
Addition of sulfur, H_2O and CO_2	Sulfides and carbonates present
Alteration halo varies in size	30-80 meter wide Thor Trend identified
Ore Geochemistry:	
Aqueous-carbonic fluid of low salinity*	Multi-phase fluid inclusions (typically 8wt% NaCl)
Formed at 250-350°C (mesozonal)	Th_{TOT} ranging from 237.0 to 325.0°C
Au carried as reduced near-neutral bisulfide complex	Inferred for Viking deposit
$\delta^{34}S$ ranges from 0-10‰ but equivocal	3.2-10.4‰ for pyrite, average 19‰ for galena
Timing of Au deposition:	
Typically late in orogenic process post-dating regional metamorphism*	Au deposited post regional metamorphism (*ca.* 419 Ma) at *ca.* 409 Ma
3 dominant periods of gold endowment worldwide	Example of Phanerozoic mineralization
Relation to magmatism:	
Intrusions nearby of roughly same age*	Intermediate Devil's Room Granite emplaced *ca.* 425
Typically felsic to intermediate composition	Ma (Heaman *et al.*, 2002)
* Characteristic not used to discriminate between orogenic and intrusion-related model	

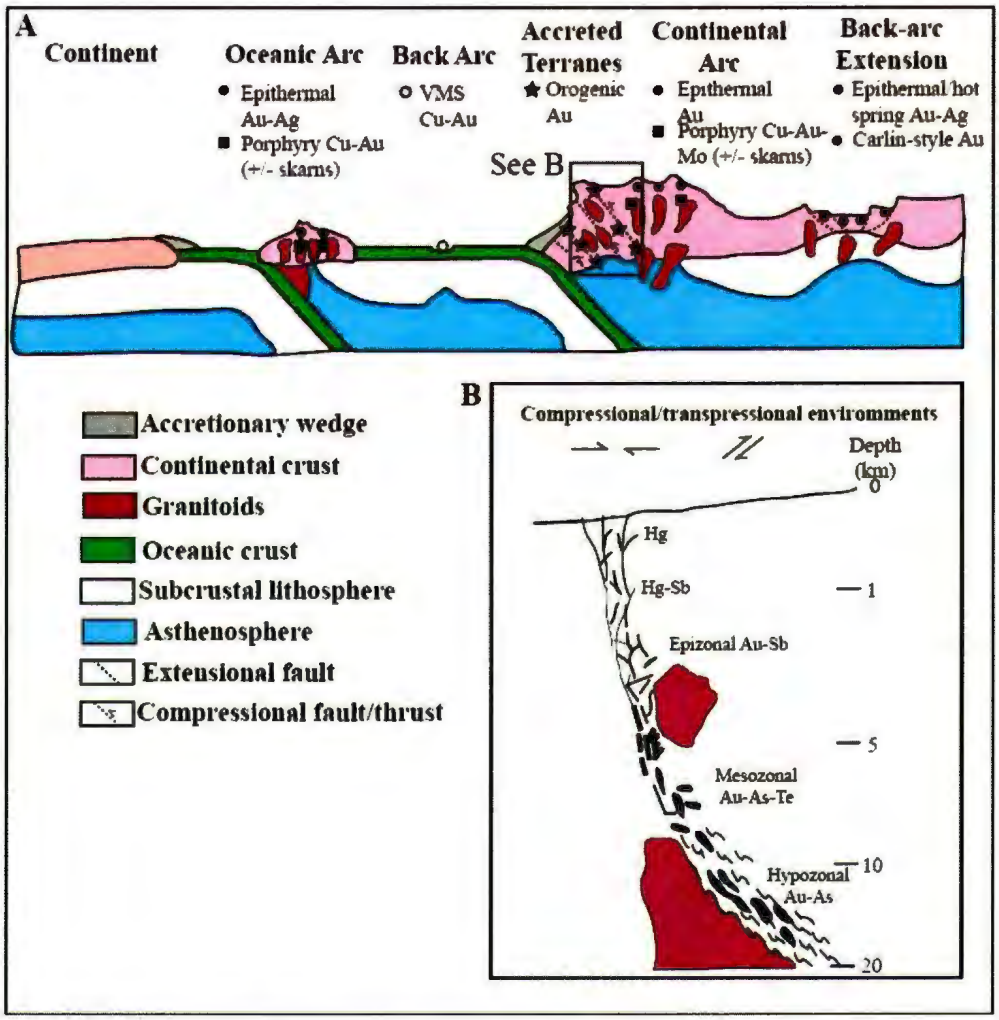

Figure 4.1: Schematic of the tectonic settings of gold-rich epigenetic mineral deposits. (A) Orogenic gold systems are emplaced proximal regional scale compressional faults within the upper crust. (B) Classification of the crustal environments of orogenic gold deposits with regard to depth of formation, structural setting and associated elements (modified from Goldfarb *et al.*, 2005). Viking deposit mineralization is classified as mesozonal (5-10 km depth) based upon microthermometric studies; however, contains little As (no data for Te).

Bibliography

Anderko, A., and Pitzer, K. S., 1993a, Equation-of-state representation of phase equilibria and volumetric properties of the system NaCl-H_2O above 573 K, Geochimica et Cosmochimica Acta, volume 57, pages 1657-1680.

Anderko, A., and Pitzer, K. S., 1993b, Phase equilibria and volumetric properties of the systems KCl-H_2O and NaCl-KCl-H_2O above 573 K: Equation of state representation, Geochimica et Cosmochimica Acta, volume 57, pages 4885-4897.

Bakker, R. J., 1997, Clathrates: Computer programs to calculate fluid inclusion V-X properties using clathrate melting temperatures, Computers & Geosciences, volume 23, pages 1-18.

Bakker, R. J., 2003, Package FLUIDS 1. Computer programs for analysis of fluid inclusion data and for modeling bulk fluid properties Chemical Geology, volume 194, pages 3-23.

Betz, F. J., 1948, Geology and mineral deposits of southern White Bay, Newfoundland Geological Survey Bulletin 24, pages 1-26.

Bursnall, J. T., 1989, Structural sequence from the southern part of the Kapuskasing structural zone in the vicinity of Ivanhoe Lake, Ontario, In Current Research Part C, Geological Survey of Canada, Paper 98-1C, pages 405-411.

Cassidy, K. F., Groves, D. I., and McNaughton, N. J., 1998, Late-Archean granitoid-hosted lode-gold deposits, Yilgarn Craton, Western Australia: Deposit characteristics, crustal architecture and implications for ore genesis, Ore Geology Reviews, volume 13, pages 65-102.

Churchill, R., and Voordouw, R., 2006, First, Second, Third, and Fourth Year Assessment Report Documenting Reconnaissance Prospecting and Compilation for Map Staked Lecenses 09287M (Wizard Property) and 08878M, 10935M, and 12734M (Viking Property), White Bay Area, Newfoundland, NTS Sheets 12H/10 and 12H/11, Assessment Report for Altius Resources Inc, pages 1-137.

Currie, J. V., 2004, Mineral exploration and metallogenic interpretation in the Sops Arm area, Newfoundland; a comparative analysis of known gold deposits, Memorial University of Newfoundland, 93 pages.

Deering, P., 1989, First and Third Year Assessment Report on the Silver Mountain Project. Licences 3612, 3158 and 3159 NTS 12H/10, 11 for Noranda Exploration Company Ltd. [012H/1093], pages 1-109.

Duan, Z., Moller, N., and Weare, J. H., 1995, Equation of state for the $NaCl-H_2O-CO_2$ system: prediction of phase equilibria and volumetric properties, Geochimica et Cosmochimica Acta, volume 59, pages 2869-2882.

Ebert, S., 2008-2011, News releases, Accessed 2011 from http://www.naminco.ca/news.php.

Ebert, S., 2010, Northern Abitibi announces 97% gold recovery from preliminary metallurgical test work at Viking, Accessed 2011 from http://www.naminco.ca/docs/NR10-10%20NAI%20Metallurgy%20Release.pdf.

Ebert, S., 2011, Northern Abitibi announces initial independent gold resource estimate for Viking, Accessed 2011 from http://www.naminco.ca/docs/NR11-3%20Resource%20Estimate%20final.pdf.

Finch, C. J., 1998, Inductively coupled plasma-emission spectrometry (ICP-ES) as the geochemical labratory, Current Research, Department of Natural Resources, volume 98-1, pages 179-183.

French, V. A., 1987, Assessment Report on 1987 exploration program licences 2831 and 2836, NTS 12H/10 and 12H/11, Silver Mountain for Noranda Exploration Company Limited. [012H-0995], pages 77.

Frost, B. R., Barnes, C. G., Collins, W. J., Arculus, R. J., Ellis, D. J., and Frost, C. D., 2001, A geochemical classification for granitic rocks, Journal of Petrology, volume 42, pages 2033-2048.

GeoREM, 2011, GeoREM - Geological and environmental reference materials online database, Accessed 2011 from http://georem.mpch-mainz.gwdg.de/.

Goldfarb, R. J., Baker, T., Dubé, B., Groves, D. I., Hart, C. J. R., and Gosselin, P., 2005, Distribution, Character, and Genesis of Gold Deposits in Metamorphic Terranes, Economic Geology 100th Anniversary Volume, volume 100, pages 407-450.

Grant, J. A., 1986, The isocon diagram - a simple solution to Gresens' equation for metasomatic alteration, Economic Geology, volume 81, pages 1976-1982.

Groves, D. I., 1993, The crustal continuum model for late-Archaean lode-gold deposits of the Yilgarn Block, Western Australia, Mineralium Deposita, volume 28, pages 366-374.

Groves, D. I., Goldfarb, R. J., Gebre-Mariam, M., Hagemann, S. G., and Robert, F., 1998, Orogenic gold deposits: A proposed classification in the context of their crustal distribution and relationship to other gold deposit types, Ore Geology Reviews, volume 13, pages 7-27.

Groves, D. I., Goldfarb, R. J., Robert, F., and Hart, C. J. R., 2003, Gold deposits in metamorphic belts: overview of current understanding,outstanding problems, future research, and exploration significance, Economic Geology, volume 98, pages 1-29.

Heaman, L. M., Erdmer, P., and Owen, J. V., 2002, U–Pb geochronologic constraints on the crustal evolution of the Long Range Inlier, Newfoundland. Canadian Journal of Earth Sciences, volume 39, pages 845-865.

Heyl, G. R., 1937, The Geology of the Sop's Arm area, White Bay, Newfoundland, Newfoundland Department of Natural Resources, Geology Section, Bulletin 8, pages 42 pages.

Hinchey, A. M., and Knight, I., 2011, Early appalachian thrusting of paleozoic metasediments within a proterozoic basement massif of the southern Long Range Inlier of Newfoundland, Geological Association of Canada Abstracts: Ottawa.

Hofstra, A. H., and Cline, J. S., 2000, Characteristics and models for Carlin-type gold deposits, Society of Economic Geologists Review, volume 13, pages 163-220.

Irvine, T. N., and Baragar, W. R. A., 1971, A guide to the chemical classification of the common volcanic rocks, Canadian Journal of Earth Sciences, volume 8, pages 523-548.

Jenner, G. A., 1996, Trace element geochemistry of igneous rocks: Geochemical nomenclature and analytical geochemistry, *in* Trace element geochemistry of volcanic rocks: Applications for massive sulfide exploration, *edited by Wyman, D. A.*, Geological Association of Canada Short Course Notes, volume 12, pages 51-77.

Jensen, M. L., 1957, Sulfur isotopes and mineral paragenesis, Economic Geology, volume 52, pages 269-281.

Jensen, M. L., 1959, Sulfur isotopes and hydrothermal mineral deposits, Economic Geology, volume 54, pages 374-394.

Kamo, S., Gower, C. F., and Krogh, T. E., 1989, A birthdate for the Iapetus ocean? A precise U-Pb zircon and baddeleyite age for the Long Range Dykes, S.E. Labrador, Geology, volume 17, pages 602-605.

Kerr, A., 2005, Geology and geochemistry of unusual gold mineralization in the Cat Arm Road area, Western White Bay: Preliminary assessment in the context of new exploration models, Current Research, Department of Natural Resources, volume 05-1, pages 173-206.

Kerr, A., 2006a, Mesothermal Gold Mineralization in the Silurian Sops Arm Group, Western Newfoundland: A Descriptive and Historical Overview, Current Research, Department of Natural Resources Geological Survey, volume 06-1, pages 61-90.

Kerr, A., 2006b, Silurian Rocks of the Sops Arm Group, Western Newfoundland: Some New Food for Future Digestion, Current Research, Department of Natural Resources Geological Survey, volume 06-1, pages 91-117.

Kerr, A., and Knight, I., 2004, Preliminary Report on the Stratigraphy and Structure of Cambrian and Ordovician Rocks in the Coney Arm Area, Western White Bay (NTS Map Area 12H/15), Current Research, Department of Natural Resources, volume 04-1, pages 127-156.

Kerr, A., and Selby, D., 2011, The timing of epigenetic gold mineralization on the Baie Verte Peninsula, Newfoundland, Canada: new evidence from Re-Os pyrite geochronology, Mineralium Deposita, volume 47, pages 325-337.

Kerr, A., and van Breemen, O., 2007, The timing of gold mineralization in White Bay, western Newfoundland: Evidence from ^{40}Ar-^{39}Ar studies of mafic dykes that predate and postdate mineralization, Atlantic Geology, volume 43, pages 148-162.

Kerr, A., van Breemen, O., and Creaser, R. A., 2006, The timing of gold mineralization at the Rattling Brook deposit, White Bay: constraints from Re-Os and 40Ar-39Ar geochronology. Current Research, Department of Natural Resources, pages 119-133.

Kerrich, R., 1993, Perspectives on genetic models for lode gold deposits, Mineralium Deposita, volume 28, pages 362-365.

Kerrich, R., and Cassidy, K. R., 1994, Temporal relationships of lode gold mineralization to accretion, magmatism, metamorphism, and deformation - Archean to present: a review, Ore Geology Reviews, volume 9, pages 263-310.

Kulp, J. L., Ault, W. U., and Feely, H. W., 1956, Sulfur isotope abundances in sulfide minerals, Economic Geology, volume 51, pages 139-149.

Ludwig, K. R., 2003, ISOPLOT 3.0: A geochronological toolkit for Microsoft Excel, Geochronology Center Special Publication, volume 4, pages 71.

Macdonald, R., Thorpe, R. S., Gaskarth, J. W., and Grindrod, A. R., 1985, Multi-component origin of Caledonian lamprophyres of northern England, Mineralogical Magazine, volume 49, pages 485-494.

Mauger, R. L., 1988, Geochemical evidence for sediment recycling from North Carolina (U.S.A.) minettes, Canadian Mineralogist, volume 26, pages 133-141.

McClay, K. R., 1987, The mapping of geological structures. Geological Society of London Handbook, Open University Press, New York, John Wiley and Sons.

McCuaig, C. T., and Kerrich, R., 1998, P--T--t--deformation--fluid characteristics of lode gold deposits: evidence from alteration systematics, Ore Geology Reviews, volume 12, pages 381-453.

McDougall, I., and Harrison, T. M., 1988, Geochronology and thermochronology by the ^{40}Ar-^{39}Ar method, Oxford Monographs on Geology and Geophysics #9, Oxford, United Kingdom, Oxford University Press, 212 p.

Minnett, M., Sandeman, H. A., and Wilton, D., 2010, Regional setting of gold mineralization at the Viking Property, southern White Bay, Newfoundland, Current Research, Department of Natural Resources, volume 10-1, pages 51-64.

Morelli, R. M., Creaser, R. A., Selby, D., Kontak, D. J., and Horne, R. J., 2005, Rhenium-Osmium Geochronology of Arsenopyrite in Meguma Group Gold Deposits, Meguma Terrane, Nova Scotia, Canada: Evidence for Multiple Gold-Mineralizing Events, Economic Geology, volume 100, pages 1229-1242.

Murray, A., 1881, Report for 1902, Geological Exploration in the District of White Bay, Geological Survey of Newfoundland, pages 485-493.

Ohmoto, H., and Rye, R. O., 1979, Isotopes of carbon and sulphur, *in* Geochemistry of hydrothermal ore deposits, *edited*: Toronoto, John Wiley and Sons, pages 509-567.

Owen, J. V., 1991, Geology of the Long Range Inlier, Newfoundland, Geological Survey of Canada Bulletin 395, pages 1-97.

Owen, J. V., and Erdmer, P., 1988, The Grenvillian Long Range Inlier of the Great Northern Peninsula, Newfoundland. Trip B7 Field Trip Guidebook, Geological Association of Canada, pages 49.

Owen, J. V., Greenough, J. D., Fryer, B. J., and Longstaffe, F. J., 1992, Petrogenesis of the Potato Hill pluton, Newfounland: transpression during the Grenvillian orogenic cycle?. Journal of the Geological Society, London, volume 149, pages 923-935.

Pearce, J. A., 1996, A user's guide to basalt discrimination diagrams, Geological Association of Canada Short Course Notes, volume 12, pages 79-113.

Pearce, J. A., Harris, N. B. W., and Tindle, A. G., 1984, Trace Element Discrimination Diagrams for the Tectonic Interpretation of Granitic Rocks, Journal of Petrology, volume 25, pages 956-983.

Reynolds. P. H., 1992, Low temperature thermochronology by the ^{40}Ar-^{39}Ar method, *in* Low Temperature Thermochronology, *edited by Zentilli. M., and Reynolds. P. H.*, Mineralogical Association of Canada, pages 3-19.

Ritcey, D. H., Wilson, M. R., and Dunning, G. R., 1995, Gold mineralization in the Paleozoic Appalachian Orogen: Constraints from geologic, U/Pb, and stable isotope studies of the Hammer Down Prospect, Newfoundland, Economic Geology, volume 90, pages 1955-1965.

Rock, N. M. S., 1991, Lamprophyres, Glasgow, UK, Blackie.

Roddick, J. C., 1983, High precision intercalibration of ^{40}Ar-^{39}Ar standards, Geochimica et Cosmochimica Acta, volume 47, pages 887-898.

Roedder. E., 1984, Fluid Inclusions, Mineralogical Society of America, 644 p.

Saunders. C. M., 1991, Mineralization in Western White Bay, Current Research, Newfoundland Department of Mines and Energy, volume 91-1, pages 335-347.

Saunders. C. M., and Smyth, W. R., 1990, Geochemical Characteristics of the Gull Lake Intrusive Suite and Devils Room Granite, Western White Bay, Newfoundland, Current Research, Newfoundland Department of Mines and Energy, volume 90-1, pages 183-199.

Saunders, C. M., and Tuach, J., 1988, K-Feldspathization, Albitization and Gold Mineralization in Granitoid Rocks: The Rattleing Brook Alteration System Western White Bay, Newfoundland, Current Research, Newfoundland and Labrador Mineral Development Division, volume 88-1, pages 307-317.

Saunders, C. M., and Tuach, J., 1991, Potassic and sodic alteration accompanying gold mineralization in the Rattling Brook deposit, western White Bay, Newfoundland Appalachians, Economic Geology, volume 86, pages 555-569.

Seal, R. R., 2006, Sulfur isotope geochemistry of sulfide minerals, Reviews in Mineralogy and Geochemistry, volume 61, pages 633-677.

Shepherd, T. J., Rankin, A. H., and Alderton, D. H. M., 1985, A practical guide to fluid inclusion studies, New York, Blackie, 239 p.

Singer, B. S., and Pringle, M. S., 1996, Age and duration of the Matuyama-Brunhes geomagnetic polarity reversal from 40Ar39Ar incremental heating analyses of lavas, Earth and Planetary Science Letters, volume 139, pages 47-61.

Smyth, W. R., and Schillereff, H. S., 1982, The Pre-Carboniferous Geology of Southwest White Bay, Current Research, Newfoundland Department of Mines and Energy, volume 82-1, pages 78-98.

Snee, L. W., Sutter, J. F., and Kelly, W. C., 1988, Thermochronology of economic mineral deposits; dating the stages of mineralization at Panasqueira, Portugal, by high-precision 40 / 39 Ar age spectrum techniques on muscovite, Economic Geology, volume 83, pages 335-354.

Snelgrove, A. K., 1935, Geology of Gold Deposits of Newfoundland, Newfoundland Department of Natural Resources, Geological Section Bulletin, pages 37-44.

Strong, D. F., and Williams, H., 1972, Early Paleozoic flood basalts of Northwestern Newfoundland: their petrology and tectonic significance., Proc. Geol. Assoc. Canada, volume 24, pages 43-54.

Sun, S., and McDonough, W. F., 1989, Chemical and isotopic systematics of oceanic basalts: implications for mantle composition and processes, *in* Magmatism in the ocean basins, *edited by Saunders, A. D., and Norry, M. J.*, Spec. Pub. Vol. Geol. Soc. Lond., No. 42, pages 313-345.

Tuach, J., 1987, Mineralized Enviroments, Metallogenesis, and the Doucers Valley Fault Complex, Western White Bay: A Philosophy for Gold Exploration in Newfoundland, Current Research, Newfoundland and Labrador Mineral Development Division, volume 87-1, pages 129-144.

Tuach, J., and French, V. A., 1986, Gold Mineralization of Possible Late Precambrian Age in the Jackson's Arm Area (12H/15), White Bay, Newfoundland, Current Research, Newfoundland Department of Mines and Energy, volume 86-1, pages 39-49.

van den Kerkhof, A. M., and Hein, U. F., 2001, Fluid inclusion petrography, Lithos, volume 55, pages 27-47.

van Staal, C. R., 2007, Pre-Carboniferous tectonic evolution and metallogeny of the Canadian Appalachians, *In* Goodfellow, W.D., ed, Mineral Deposits of Canada: A synthesis of major deposit types, district metallogeny, the evoloution of geological provinces, and exploration methods, Geological Association of Canada, Mineral Deposits Division, Special Publication No. 5, pages 783-818.

Whalen, J. B., Currie, K. L., and CHappell, B. W., 1987, A-type granites: geochemical characteristics, discrimination and petrogenesis, Contrib. Mineral. Petrol. 95, pages 407-419.

Wilkinson, J. J., 2001, Fluid inclusions in hydrothermal ore deposits, Lithos, volume 55, pages 229-272.

Williams, H., 1979, Appalachian Orogen in Canada, Canadian Journal of Earth Sciences, volume 16, pages 792-807.

Williams, H., 1995a, Introduction (Humber Zone), *in* Geology of the Appalachian-Caledonian Orogen in Canada and Greenland, *edited by Williams, H.*, Geological Survey of Canada, Geology of Canada, pages 47-49.

Williams, H., 1995b, Introduction: Chapter 1, *in* Geology of the Appalachian-Caledonian Orogen in Canada and Greenland, *edited by Williams, H.*, Geological Survey of Canada, Geology of Canada, pages 1-19.

Williams, H., and Stevens, R. K., 1974, The Ancient Continental Margin of Eastern North America, *in* The Geology of Continental Margins, *edited by Burk, C. A., and Drake, C. C.*: New York, Springer-Verlag, pages 781-796.

Winchester, J. A., and Floyd, P. A., 1977, Geochemical discrimination of different magma series and their differentiation products using immobile elements, Chemical Geology, volume 20, pages 325-343.

Wyman, D. A., and Kerrich, R., 1989, Archean lamprophyre dykes of the Superior Province, Canada: Distribution, petrology, and geochemical characteristics, Journal of Geophysical Research, volume 94, pages 4667-4696.

Zartman, R. E., and Doe, B. R., 1981, Plumbotectonics--the model, Tectonophysics, volume 75, pages 135-162.

APPENDIX A

ANALYTICAL METHODS

A.1 SCANNING ELECTRON MICROSCOPY

Standard thin sections were coated in carbon before being mounted on a stage which is then placed into the FEI Quanta 400 SEM in the Bureau Center at Memorial University of Newfoundland. The sections are held under a vacuum at 25.0 kV where a fine beam of electrons is focused on the sample surface. The beam then rasters in a rectangular pattern and the intensities of the signals created are mapped as variations in brightness corresponding to an elements atomic number. Semi-quantitative maps (e.g. Plate 2.10 C) were processed using in house software and saved as jpeg images.

A.2 LITHOGEOCHEMISTRY

Lithogeochemical samples collected during traverses and from diamond drill core include altered host rocks adjacent to, and within, mineralized zones as well as unaltered samples collected remote from mineralization. As such, the whole-rock compositions of many host rocks collected for this study were probably modified by post-crystallization hydrothermal fluid-rock interaction to some extent. Samples of plutons exposed elsewhere in the region were also analyzed for comparison with the Main River Pluton. A total of 48 samples were analyzed from both bedrock exposures and drill core; the lithogeochemical data are presented in Table B.1.

Major elements were determined by ICP-OES at the Geochemical Laboratory of the Department of Natural Resources, Howley Building (Higgins Line, St. John's NL), following analytical methods described in (Finch, 1998). Pulverization of the samples

was completed using an alumina zirconia swing mill. Fluoride was determined by ion specific electrode, also at the Howley Building. High-field-strength elements (HFSE; Y, Zr, Nb, Hf, Ta, and Ga), large-ion-lithophile elements (LILE; Cs, Ba, Rb, Sr, Th, and U), transition elements (V, Cr, Co, Ni), base metals (Cu, Zn, and Pb), volatile elements (Sn, Sb, Tl, and As), and rare-earth elements (REE; La-Lu) were determined by lithium metaborate/tetraborate fusion ICP-MS at Activation Laboratories in Ancaster, Ontario, using the methods documented on their website (http://www.actlabs.com). Gold and Sc were analyzed at Becquerel Laboratories by Neutron Activation Analysis (following their analytical procedure at http://www.becquerellabs.com).

Assay data of mineralized quartz vein material from the Thor vein were obtained from the Northern Abitibi Mining Corporation database to complement the lithogeochemical database from this study and those results are presented in Table 2.1. Gold (as well as Cu, Zn, Pb, As, Ag, Cr, V, Co, Ni, Sn, Sb, W, Ba, Sr, La and Ce) contents were determined by standard fire assay ICP methods at Eastern Analytical, Springdale, Newfoundland, and samples with greater than 5 g/t gold were re-assayed using a metallic sieve procedure to reduce the nugget effect created by free gold particles in the samples.

A.3 ARGON THERMOCHRONOLOGY

The ^{40}Ar-^{39}Ar laser step-heating data were obtained at Queen's University ^{40}Ar-^{39}Ar Thermochronology Laboratory. All weathering surfaces were removed and a fist-sized whole-rock portion of each specimen was carefully milled by mortar and pestle. The crushed material was then sieved to a -40+60 mesh (0.422–0.251 mm) size fraction. The

grain separates were ultrasonically agitated in a dilute (2.5 %) solution of reagent grade HNO_3. The samples were frequently cleaned in de-ionized water, dried, and then processed through a Frantz isodynamic magnetic separator after a hand magnet was passed over the crushed material. Approximately 500 mg of high purity biotite and sericite concentrate were packed in aluminum foil and stacked sequentially and interspersed with reference flux monitors of known age (Hb3gr: 1072 Ma; Roddick, 1983). These were evenly spaced with the unknowns, to enable precise determination of the irradiation parameter, "J", throughout the irradiation tube. Unknowns and flux monitors were irradiated with fast neutrons in position 5C for 40 hours (3 MWH) at the McMaster University Reactor, McMaster University, Hamilton, Ontario.

Total-gas, integrated ages (equivalent to a K-Ar age: IA), plateau ages (PA) and inverse isotope-correlation ages (CA) are reported. Traditionally, a plateau is defined by three contiguous steps overlapping in error and comprising greater than or equal to 50% of the ^{39}Ar released, and reasonably low excess scatter (mean square of the weighted deviates (MSWD) < 2.2; McDougall and Harrison, 1988; Singer and Pringle, 1996; Snee *et al.*, 1988). These criteria were not satisfied by all of the gas release spectra for the samples under investigation. The gas steps used in the calculation of the plateau ages, as well as the inverse isotope-correlation ages, are marked by asterisks in Table C.1 and are filled black boxes in Figure 2.10. The approximate argon closure temperatures for sericite (muscovite: *ca.* 350°C) and biotite (*ca.* 280°C) were applied to these minerals and are used to aid in the interpretation of the cooling history of the host rocks (McDougall and Harrison, 1988; Reynolds, 1992) (McDougall and Harrison, 1988; Reynolds, 1992). All age calculations used the ^{40}Ar-^{39}Ar age spectrum module of Ludwig (2003).

A.4 FLUID INCLUSION ANALYSIS

Fluid inclusion analysis was completed in house at the fluid inclusion laboratory in the Inco Innovation Centre, Memorial University of Newfoundland. The analyses were completed on a Linkam THMSG600 heating freezing stage, mounted on an Olympus BX51 microscope outfitted for use with reflected- and transmitted-visible and ultraviolet light using 4x, 10x, 40x and 100x Olympus long-working distance objective lenses. This system allows phase transitions to be observed in fluid inclusions over the temperature range of -193 to 600°C. Digital images of fluid inclusions are captured using an Olympus DP71 camera. Rock thin sections and doubly polished fluid inclusion wafers were prepared at Memorial University using standard techniques.

The fluid inclusions were first observed at a temperature of 15°C to observe their morphology, relation to host mineral, and degree of fill. This enabled groups of fluid inclusions with similar properties, or fluid inclusion assemblages (FIA), to be targeted for microthermometric analysis. The FIA was then cooled at a rate of 40°C per minute to -100°C which caused the freezing of all phases in the inclusions. The FIA is then heated at 30°C/min to -60°C and through to -55°C at a slower rate of 3°C/min. The melting of CO_2 phases (Tm_{CO2}) occurs roughly at -56.6°C and a slow heating rate promotes a more accurate temporal observation of this temperature, to within ±0.1°C. Heating continues through 0°C where at approximately +6.6°C, the clathrate phase melts (Tm_{clath}) and the vapour CO_2 bubble within each fluid inclusion in the FIA moves freely. At temperatures of approximately 20 to 25°C, homogenization of the vapour and liquid CO_2 phase occurs (Th_{CO2}). How the vapour and liquid phase interact upon reaching Th_{CO2} gives information

on the CO_2/H_2O ratio of the inclusions; if the H_2O phase disappears upon Th_{CO2} then there is a high CO_2/H_2O ratio and if the CO_2 phase disappears then there is a low ratio (Shepherd *et al.*, 1985). The final step is to heat the FIA to the temperature at which all phases in the inclusion homogenize (Th_{TOT}).

Calculation of salinity and density of the fluid inclusions was completed using the computer package "Clathrates" created by Bakker (1997). The program "Q2" in this package used the measured Tm_{Clath}, Th_{CO2}, and the mode of homogenization of the CO_2 phase to calculate salinity and density using the algorithms of Duan *et al.* (1995). The program "Loner 15" within the "Fluids" package of Bakker (2003) was used to calculate pressure. Bulk fluid properties (xCO_2, xH_2O, xNaCl, xKCl) are calculated in the Q2 program and are used to calculate pressure, along with Th_{TOT} and the fluid inclusions molar volume (also calculated in Q2). These calculations are completed within a H_2O-CO_2 fluid system (Anderko and Pitzer, 1993a, b; Duan *et al.*, 1995). Pressure is given in MPa and bars which is converted to depth in kilometers.

A.5 STABLE AND RADIOGENIC ISOTOPE ANALYSIS

Stable isotope analysis for sulfur and radiogenic isotope analysis for lead was completed by *in-situ* microanalysis of sulfide minerals using the secondary ion mass spectrometer (SIMS) located in the Inco Innovation Centre at Memorial University of Newfoundland. A focused beam of charged Cs sputters the sample surface and secondary ions are measured using a mass spectrometer (Seal, 2006). Spatial resolution is typically better than 20 μm with an analytical uncertainty ranging from ±0.2 to 0.5‰. Sulfide

minerals analyzed were a part of the mineralization assemblage of the high-grade veins and are associated with gold.

A total of 12 mounts were prepared from high-grade zones that contained sulfide minerals amendable to *in-situ* analysis. Samples were placed face-down inside a 2.5 cm diameter metal ring (i.e. the mount) and this assembly is attached to a piece of double-sided tape on a glass plate. A solution of epoxy is prepared using 100 parts resin to 39 parts hardener which is poured into the metal ring under a fume hood. The epoxy is stirred to remove any air bubbles trapped around the rock sample. After the epoxy has solidified after a period of about 24 hours the mount is removed from the double-sided tape and placed in the Struers Tegra Force 5 polishing system. Polishing was completed 6 mounts at a time using the "fine-sulfides" program on the Struers. The mounts were washed in an ultra-sonic agitator between steps to remove any free grit and excess material. One mount at a time can be placed into the mass spectrometer for analysis.

APPENDIX B

LITHOGEOCHEMICAL DATA

B.1 INTRODUCTION

This appendix will present and discuss the precision and accuracy for the data, includes a table of the entire lithogeochemical dataset (Table B.1), and a table of the mass gain/loss calculation (Table B.2). Classification of precision and accuracy is taken from Jenner (1996) and is as follows: excellent (0-3%), very good (3-7%), good (7-10%), and poor (>10%). All data used to calculate precision and accuracy is in the digital appendix.

Major and trace element precision was determined using duplicate analysis of unknown samples (i.e. samples from the dataset of this study). Precision (a measure of analytical reproducibility) was calculated as relative standard deviation (RSD) = $[(X_1 - X_2)/((X_1 + X_2)/2)]*100$, where X_1 is the original analysis and X_2 is the duplicate analysis. Duplicate analysis of samples 09MM006 (diorite), 09MM111 (monzogranite), and 09MM054 (granodiorite) were used to calculate major element precision. Duplicate analysis of samples 09MM006, 09MM111, 09MM057 (granodiorite), 09MM065 (diorite), and 09MM113 (monzogranite) were used to calculate trace element precision.

Analytical accuracy is a measure of correctness or how close an analysis is to the "true" or "accepted" value. It is typically measured using international geochemical reference materials but can also be measured using internal "secondary standards" that are developed by analytical companies. These materials are typically chosen to best represent the composition of the unknown sample (i.e., are matrix matched). It may be reported as a percent difference to the "true" value, relative difference (RD) = $((X_{lab} -$

$X_{accepted})/X_{accepted})*100$, where X_{lab} is the lab analysis of a standard and $X_{accepted}$ is the "true" or "accepted" value. The standards which were analyzed to calculate major element accuracy include FK-N, AND-1, and VS-N following methods of Finch (1998). Standards SY-4 (diorite gneiss) and WGB-1 (gabbro) were used to calculate trace element accuracy. Trace element standard data was acquired from the GeoREM online database (GeoREM, 2011).

B.2 PRECISION AND ACCURACY

B.2.1 Major Element Precision

Precision is dominantly excellent (0-3%) to very good (3-7%) for the major elements of the samples analyzed (Figure B.1). Poor precision (>10%) was obtained only for CaO, MnO, P_2O_5 and LOI.

B.2.2 Major Element Accuracy

Major element accuracy for standards AND-1 and VS-N were predominantly excellent to very good. Standard FK-N was the only standard to return poor precision for TiO_2, Fe_2O_3, MnO, MgO, and P_2O_5 (Figure B.2).

B.2.1 Trace Element Precision

Trace element precision is somewhat variable ranging from excellent to good with poor precision dominated by the duplicate analysis for sample 09MM113 (monzogranite). The average RSD is primarily very good (Figure B.3). Transition and volatile elements have typically excellent to very good precision and base metal elements generally have very good to good precision. Only Cs, of the LFSE, has poor precision for one sample; however, there is a wide range of precision for the HFSE (e.g. Y, Zr, Ta). The REEs have

typically excellent to good precision, dominated by very good precision with one sample (09MM113) returning poor precision.

B.2.2 Trace Element Accuracy

Standards SY-4 (n=5) and WGB-1 (n=3) show variation in their trace element accuracies with few trace elements for SY-4 having excellent a and no trace elements of WGB-1 having excellent precision (Figure B.4). WGB-1 contains very low concentrations of trace elements and requires low detection limits to produce excellent accuracy. The accuracy for SY-4 over numerous analyses is dominantly very good.

B.3 LITHOGEOCHEMICAL DATA

Table B.1 reports geochemical data for samples taken from the Main River Pluton as well as other granitic plutons in the White Bay area. All oxides are in weight % and trace elements are in ppm (gold in ppb). $Fe_2O_3^T$ denotes total iron as ferric iron and FeO* is the total iron as ferrous iron. Mg# = (molecular MgO/(molecular MgO+FeO^T)), Fe# = FeO*/FeO*+MgO, and modified alkali-lime index (MALI) (Frost et al., 2001), $_{CN}$ Chondrite Normalized (Sun and McDonough, 1989). N/A denotes not analyzed. Values which are one half of the detection limit signify that the analysis was below detection limit for the given element and is used to define a background for comparison with other samples.

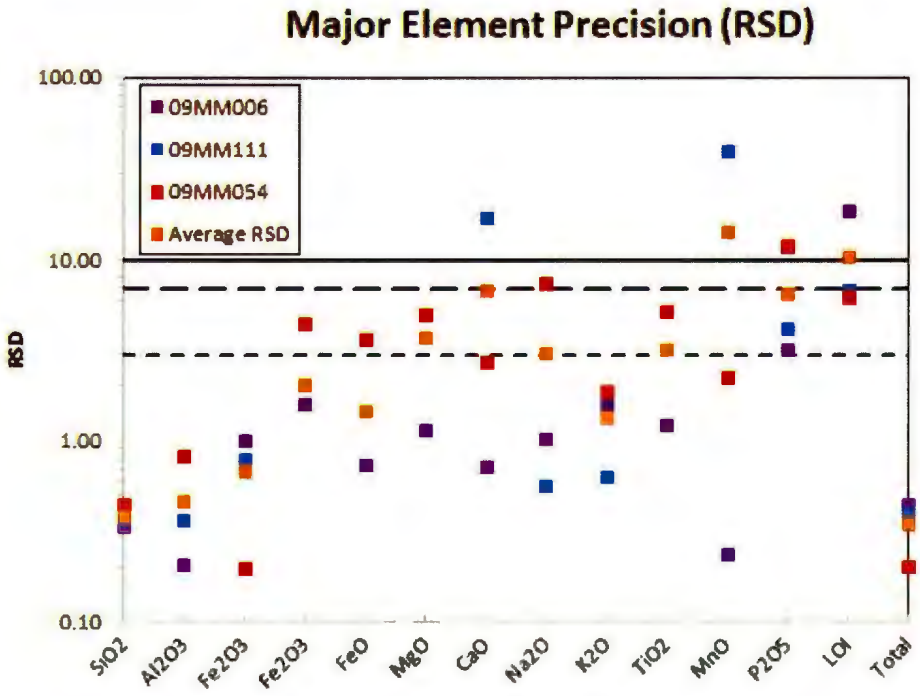

Figure B.1: Major element precision (RSD) for three duplicate analysis of unknown samples. The precision is better than 7% for the majority of analyses. Excellent precision <3% RSD (short dashed line), very good precision is 3-7% RSD (between short and long dashed lines), good precision is 7-10% RSD (between long dashed line and solid line), and poor precision is >10% RSD (above solid line).

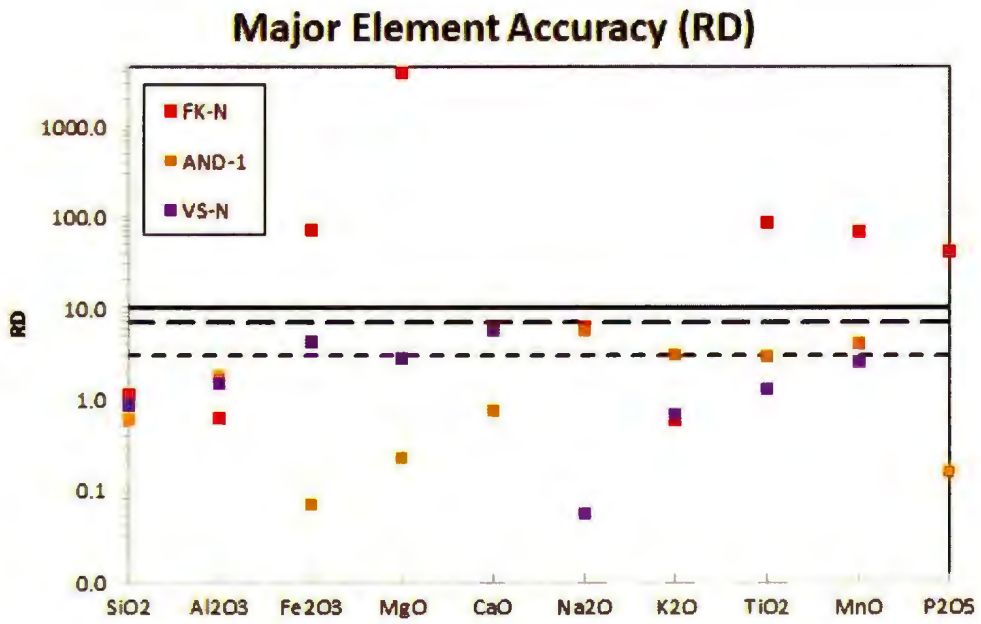

Figure B.2: Major element accuracy (RD) based upon analysis of 3 international reference materials. Poor accuracy (<10% RD) is reported only for FK-N. Excellent accuracy <3% RSD (short dashed line), very good accuracy is 3-7% RSD (between short and long dashed lines), good accuracy is 7-10% RSD (between long dashed line and solid line), and poor accuracy is >10% RSD (above solid line).

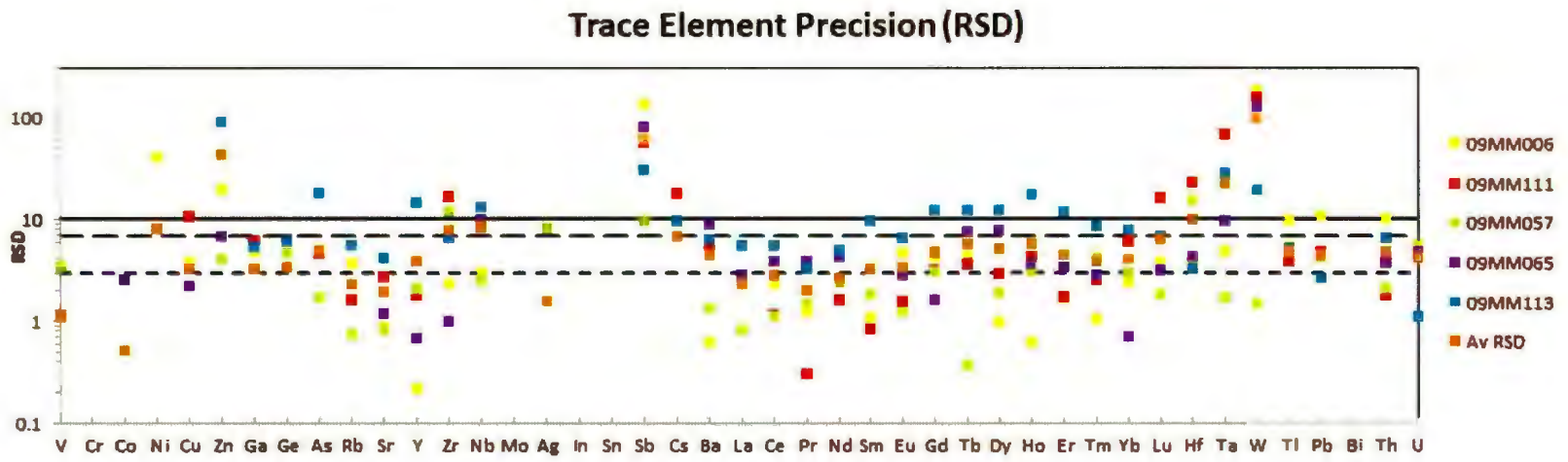

Figure B.3: Trace element precision for duplicates of five analyses of samples from the Viking deposit.

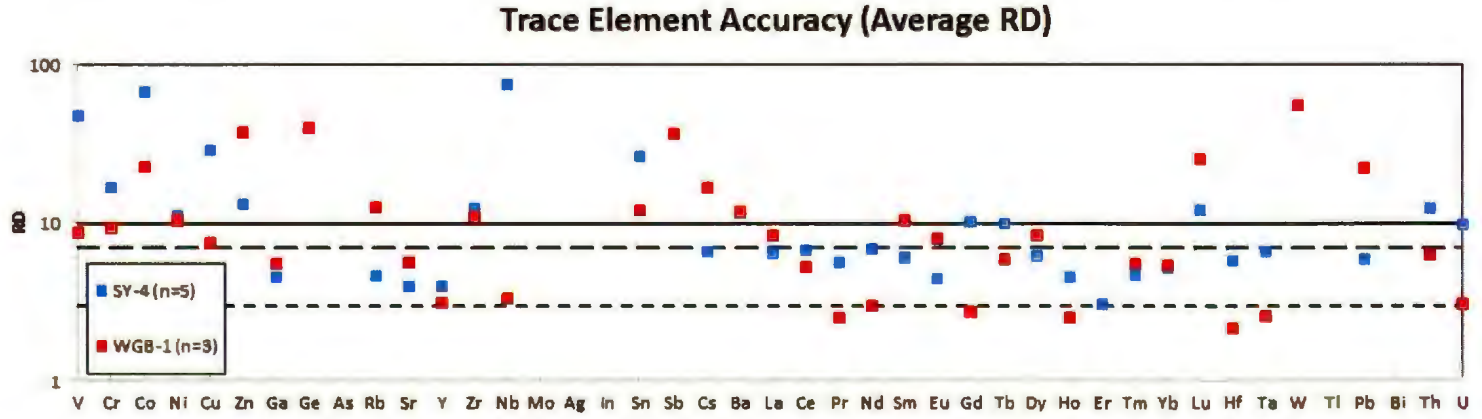

Figure B.4: Trace element accuracy for multiple analyses of standards SY-4 and WGB-1.

Table B.1 (Next Page): Lithogeochemical compositions for the rock types at the Viking deposit and surrounding granitic plutons. All oxides are in weight % and trace elements are in ppm (gold in ppb). $Fe_2O_3^T$- total iron as ferric iron, FeO* - total iron as ferrous iron, Mg# = 100*(molecular MgO/(molecular MgO+FeO^T)), Fe# = 100*(FeO*/FeO*+MgO), MALI – modified alkali-lime index (Frost *et al.*, 2001), $_{CN}$ Chondrite Normalized (Sun and McDonough, 1989). N/A denotes not analyzed.

Sample		09MM034	09MM042	09MM054	09MM056	09MM057	09MM058	09MM063
Rock Type		AG'	AG'	AG'	AG'	AG'	AG'	AG'
Easting		501425	500582	500651	500651	500651	500651	500582
Northing		5505328	5504442	5504651	5504651	5504651	5504651	5504431
Drill Hole			08-VK-01	08-VK-04	08-VK-04	08-VK-04	08-VK-04	08-VK-05
From			58.75	23.26	45	48.23	52.1	34.45
To	DL		59.15	23.78	45.8	48.95	52.28	34.85
SiO_2	0.02	69.13	61.16	70.74	65.19	59.25	59.74	59.57
Al_2O_3	0.01	14.84	16.65	10.80	12.95	16.17	15.60	16.28
Fe_2O_3	0.01	2.96	2.22	1.33	1.10	1.73	1.16	2.44
FeO	0.01	0.38	2.71	1.56	2.77	2.91	2.46	3.16
MgO	0.01	0.88	1.64	0.50	1.02	1.22	0.94	1.52
CaO	0.01	0.28	3.14	3.38	2.91	3.72	3.87	3.22
Na_2O	0.01	3.11	4.31	1.08	3.07	3.90	4.01	4.43
K_2O	0.01	5.54	4.75	4.00	4.10	4.90	4.62	3.43
TiO_2	0.001	0.702	0.995	0.687	0.768	1.045	0.865	1.136
MnO	0.01	0.028	0.088	0.051	0.068	0.086	0.082	0.063
P_2O_5	0.001	0.214	0.336	0.194	0.217	0.307	0.245	0.340
LOI	0.01	1.39	1.08	4.19	4.74	4.11	5.20	2.46
Total	n/a	99.43	99.08	98.50	98.90	99.36	98.78	98.05
Fe_2O_3t	n/a	3.38	5.23	3.07	4.18	4.96	3.89	5.95
FeO*	n/a	3.04	4.71	2.76	3.76	4.47	3.50	5.36
CO_2	0.01	0.09	0.19	n/a	n/a	n/a	n/a	n/a
Mg#	n/a	31.59	35.78	22.53	30.26	30.55	30.01	31.22
Fe#	n/a	0.30	0.62	0.76	0.73	0.70	0.72	0.68
MALI	n/a	8.37	5.92	1.70	4.25	5.08	4.76	4.64
Sc	0.1	4.6	n/a	n/a	n/a	n/a	n/a	n/a
V	5	41	60	47	45	59	53	62
Cr	20	10	10	10	10	10	10	10
Co	1	6	9	6	6	7	5	8
Ni	20	10	10	10	10	10	10	10
Cu	10	5	20	70	50	40	30	10
Zn	30	30	110	210	520	240	100	100
Pb	5	15	29	329	259	48	18	12
Au	2	2	1	n/a	n/a	n/a	n/a	n/a
Ag	0.5	0.8	1.5	3.7	3	2.5	1.8	1.9
Sn	1	3	5	3	4	6	5	4
Sb	0.2	0.1	0.4	1.1	1.4	1	1.1	0.2
W	0.5	6.4	2.9	21.4	14.7	13.8	13.5	0.25
F	5	592	1362	1155	1071	1238	1032	1554
S	0.01	0.01	0.12	n/a	n/a	n/a	n/a	n/a
Tl	0.05	0.72	1.02	0.71	0.85	1.13	0.95	0.87
As	5	2.5	2.5	65	46	120	42	2.5
Cs	0.1	1.6	0.9	0.9	1	1.4	0.9	2
Ba	3	1710	2500	1050	1270	1520	1460	1380
Rb	1	120	145	108	107	135	119	109
Sr	2	165	573	116	363	373	358	390
Th	0.05	7.32	11.1	5.19	7.85	19.4	13.4	8.89
U	0.01	1.49	3.38	1.46	2.24	3.47	2.63	2.05
Y	0.5	38.1	70.2	36.2	42.3	78	56.2	57.2
Zr	1	390	674	409	415	571	492	553

Sample		09MM034	09MM042	09MM054	09MM056	09MM057	09MM058	09MM063
Rock Type		AG[1]	AG[1]	AG[1]	AG[1]	AG[1]	AG[1]	AG[1]
Easting		501425	500582	500651	500651	500651	500651	500582
Northing		5505328	5504442	5504651	5504651	5504651	5504651	5504431
Drill Hole			08-VK-01	08-VK-04	08-VK-04	08-VK-04	08-VK-04	08-VK-05
From			58.75	23.26	45	48.23	52.1	34.45
To	DL		59.15	23.78	45.8	48.95	52.28	34.85
Nb	**0.2**	19.7	25.2	12.2	15.2	23.9	18.2	20.1
Hf	**0.1**	8.8	13.9	8.7	8.9	12.6	10.7	11.9
Ta	**0.01**	1.78	1.85	1.01	1.15	1.79	1.37	1.69
Ga	**1**	21	25	20	22	27	27	26
Ge	**0.5**	1.3	1.5	2.3	2.2	2.1	2.1	1.6
La	**0.05**	72	93.1	68.8	74.3	123	101	110
Ce	**0.05**	165	221	156	167	270	217	250
Pr	**0.01**	21.5	30.2	19.3	20.6	33.6	26	31
Nd	**0.05**	74.4	114	70.7	75.9	124	94.3	113
Sm	**0.01**	11.3	19	11.7	12.8	22.2	16.1	18.9
Eu	**0.005**	1.97	3.24	2.09	2.23	3.22	2.75	3.08
Gd	**0.01**	8.99	15.7	9.32	10.6	19.7	13.4	15
Tb	**0.01**	1.32	2.28	1.23	1.42	2.76	1.87	1.98
Dy	**0.01**	6.93	12.4	7.06	8.22	16	11	11.3
Ho	**0.01**	1.33	2.41	1.31	1.54	2.95	2.05	2.07
Er	**0.01**	3.94	7.06	3.84	4.48	8.52	6.06	6.11
Tm	**0.005**	0.581	1.03	0.537	0.643	1.19	0.866	0.849
Yb	**0.01**	3.75	6.33	3.25	3.92	7.07	5.24	5.08
Lu	**0.002**	0.556	0.925	0.502	0.631	1.11	0.834	0.805
$(La/Yb)_{CN}$	**n/a**	13.8	10.5	15.2	13.6	12.5	13.8	15.5
$(La/Sm)_{CN}$	**n/a**	4.11	3.16	3.80	3.75	3.58	4.05	3.76
$(Gd/Yb)_{CN}$	**n/a**	1.98	2.05	2.37	2.24	2.31	2.12	2.44

Sample	09MM098	09MM102	09MM107	09MM112	09MM115	09MM160	09MM006
Rock Type	AG'	AG'	AG'	AG'	AG'	AG'	Diorite
Easting	500570	500591	500557	500619	500620	499856	499867
Northing	5504457	5504374	5504529	5504180	5504020	5504741	5504137
Drill Hole							
From							
To							
SiO_2	62.20	62.03	61.43	61.92	60.79	64.70	49.31
Al_2O_3	15.74	15.24	16.42	16.30	16.19	14.57	12.65
Fe_2O_3	2.04	1.26	2.50	2.67	2.27	2.14	4.90
FeO	2.79	1.36	2.81	2.46	3.09	2.23	10.07
MgO	1.38	0.78	1.72	1.39	1.62	1.38	4.63
CaO	1.90	4.95	2.79	2.19	3.51	2.57	7.95
Na_2O	4.45	3.91	4.34	4.17	4.11	3.93	2.90
K_2O	4.93	3.47	4.45	4.80	3.81	4.71	1.09
TiO_2	0.946	0.594	1.071	1.073	1.087	0.916	2.644
MnO	0.071	0.065	0.075	0.075	0.065	0.065	0.234
P_2O_5	0.333	0.185	0.355	0.363	0.378	0.315	0.282
LOI	1.73	5.29	0.87	1.53	1.17	0.59	0.72
Total	98.51	99.14	98.84	98.94	98.08	98.11	97.38
Fe_2O_3t	5.14	2.78	5.63	5.41	5.70	4.62	16.09
FeO*	4.63	2.50	5.06	4.87	5.13	4.16	14.48
CO_2	0.61	0.94	0.03	0.34	0.02	0.04	0.06
Mg#	32.37	33.47	35.24	31.35	33.60	34.73	33.89
Fe#	0.67	0.63	0.62	0.64	0.66	0.62	0.69
MALI	7.49	2.42	6.00	6.77	4.40	6.07	-3.96
Sc	9.0	7.1	13.0	9.0	10.0	7.2	38.5
V	59	54	64	59	60	48	449
Cr	10	10	10	10	10	10	10
Co	9	8	9	9	11	8	46
Ni	10	10	10	10	10	10	60
Cu	10	20	5	20	70	5	270
Zn	90	70	120	280	80	110	170
Pb	26	15	24	48	23	22	10
Au	6	1	1	1	1	1	1
Ag	1.1	1.1	1.3	1.1	1.1	0.9	0.25
Sn	4	4	7	5	4	4	2
Sb	0.6	0.7	2.5	1.2	1.2	0.1	5.4
W	3.5	3.1	1.1	17.7	2.4	2.2	4.2
F	1273	1060	1526	1497	1117	237	306
S	0.09	0.005	0.05	0.12	0.12	0.02	0.07
Tl	0.97	0.74	1.06	0.94	0.73	0.78	0.1
As	12	2.5	2.5	2.5	2.5	2.5	2.5
Cs	3.8	3.4	1.1	2.2	1.2	0.4	0.4
Ba	2520	1920	2280	2230	2150	1990	329
Rb	133	111	147	130	93	118	28
Sr	475	389	504	497	578	554	232
Th	8.51	7.29	10.8	9.15	7.56	13.3	2.31
U	1.95	2.02	3.65	2.56	1.4	1.58	0.64
Y	62.4	58.9	80.2	66.6	70.3	64.7	45.7
Zr	552	583	689	599	624	514	219

Sample	09MM098	09MM102	09MM107	09MM112	09MM115	09MM160	09MM006
Rock Type	AG[1]	AG[1]	AG[1]	AG[1]	AG[1]	AG[1]	Diorite
Easting	500570	500591	500557	500619	500620	499856	499867
Northing	5504457	5504374	5504529	5504180	5504020	5504741	5504137
Drill Hole							
From							
To							
Nb	19.3	19.8	31.4	23.2	26.5	25.5	13.6
Hf	11.6	12.1	14.6	12.1	13	11.3	5
Ta	1.65	1.62	2.6	1.96	1.99	2.65	0.86
Ga	24	23	27	24	24	21	21
Ge	1.4	1.2	1.5	1.5	1.4	1.4	1.7
La	105	91.9	99.2	106	110	127	16.7
Ce	221	216	250	241	261	279	39.4
Pr	31.7	29.8	33.6	33.2	36.7	35.4	5.7
Nd	117	113	125	122	137	123	25.7
Sm	19.4	18.5	21	20.3	22.6	19.3	6.52
Eu	3.34	3.22	3.39	3.45	3.78	3.14	2.18
Gd	15.7	15.2	17.6	16.4	18.2	15.5	8.62
Tb	2.23	2.19	2.6	2.33	2.6	2.23	1.43
Dy	11.7	11.6	14	12.4	13.7	12.1	8.24
Ho	2.17	2.16	2.74	2.29	2.6	2.27	1.63
Er	6.18	6.19	8.17	6.64	7.38	6.73	4.63
Tm	0.86	0.882	1.26	0.942	1.03	1.02	0.675
Yb	5.04	5.21	7.93	5.74	6.2	6.29	4.29
Lu	0.725	0.715	1.16	0.82	0.852	0.902	0.67
$(La/Yb)_{CN}$	14.9	12.7	9.0	13.2	12.7	14.5	2.8
$(La/Sm)_{CN}$	3.49	3.21	3.05	3.37	3.14	4.25	1.65
$(Gd/Yb)_{CN}$	2.58	2.41	1.84	2.36	2.43	2.04	1.66

Sample	09MM010	09MM011	09MM012	09MM016	09MM064	09MM065	09MM066
Rock Type	Diorite	Diorite	Diorite	Diorite	Diorite	Diorite	Diorite
Easting	497753	498076	497585	497380	500582	500582	500582
Northing	5506016	5506597	5506680	5505719	5504431	5504431	5504431
Drill Hole					08-VK-05	08-VK-05	08-VK-05
From					41	53.94	68.05
To					41.33	54.42	68.55
SiO_2	47.91	49.76	55.23	54.59	48.59	47.41	51.12
Al_2O_3	11.44	14.35	16.48	15.87	12.29	12.25	12.69
Fe_2O_3	5.53	2.78	3.01	2.54	6.25	7.19	5.38
FeO	9.52	9.39	5.05	5.93	8.44	7.93	9.40
MgO	6.18	5.63	3.16	4.61	4.31	4.47	4.34
CaO	9.38	9.68	5.72	6.12	7.94	9.34	7.45
Na_2O	2.44	2.50	4.01	3.63	2.40	2.36	3.28
K_2O	1.31	0.90	2.56	2.33	2.00	0.48	1.18
TiO_2	2.080	1.954	1.827	1.870	2.554	2.533	2.576
MnO	0.332	0.202	0.107	0.098	0.231	0.233	0.237
P_2O_5	0.329	0.211	0.599	0.655	0.310	0.295	0.354
LOI	1.00	0.95	0.77	0.91	1.76	2.83	1.06
Total	97.45	98.32	98.52	99.16	97.07	97.34	99.08
Fe_2O_3t	16.11	13.21	8.62	9.14	15.62	16.00	15.82
FeO*	14.50	11.89	7.76	8.22	14.06	14.40	14.24
CO_2	0.02	0.06	0.1	0.09	0.83	1.38	0.42
Mg#	40.59	43.17	39.50	47.33	32.96	33.22	32.84
Fe#	0.61	0.63	0.62	0.56	0.66	0.64	0.68
MALI	-5.63	-6.28	0.86	-0.16	-3.54	-6.50	-2.99
Sc	31.4	36.5	16.0	15.0	38.1	39.6	38.4
V	268	336	140	120	423	439	402
Cr	30	70	10	30	10	10	10
Co	40	42	25	31	39	39	41
Ni	40	60	30	50	40	40	40
Cu	220	210	30	20	310	450	270
Zn	210	120	130	110	420	140	140
Pb	8	2.5	14	10	10	12	10
Au	1	1	1	1	7	1	1
Ag	0.25	0.25	1	0.25	0.6	0.25	0.25
Sn	4	2	3	3	2	2	2
Sb	0.1	1.4	0.1	0.1	0.5	0.5	0.2
W	0.25	1	0.25	0.25	2.5	0.25	0.25
F	1578	176	1128	1564	595	257	363
S	0.35	0.03	0.11	0.15	0.09	0.1	0.13
Tl	0.25	0.25	0.41	0.66	0.46	0.25	0.08
As	2.5	2.5	2.5	2.5	2.5	2.5	2.5
Cs	0.05	0.5	0.4	0.7	2.2	0.1	0.6
Ba	401	211	1140	838	577	144	384
Rb	13	21	73	107	66	7	28
Sr	343	258	749	771	238	249	211
Th	1.85	1.39	2.96	3.22	2.42	2.16	2.61
U	0.85	0.39	0.72	0.7	0.77	0.62	0.76
Y	42.6	32	37.6	31.5	48.1	43.5	52.3
Zr	250	160	463	227	239	198	257

Sample	09MM010	09MM011	09MM012	09MM016	09MM064	09MM065	09MM066
Rock Type	Diorite	Diorite	Diorite	Diorite	Diorite	Diorite	Diorite
Easting	497753	498076	497585	497380	500582	500582	500582
Northing	5506016	5506597	5506680	5505719	5504431	5504431	5504431
Drill Hole					08-VK-05	08-VK-05	08-VK-05
From					41	53.94	68.05
To					41.33	54.42	68.55
Nb	35	9.6	23.2	18.7	14.2	13.1	14.8
Hf	5.4	3.8	9.7	5	5.4	4.7	5.7
Ta	0.89	1.49	1.3	1.06	0.91	0.83	0.99
Ga	23	19	26	21	21	21	21
Ge	2.4	1.8	1.4	1.4	1.9	1.9	1.7
La	24.5	12.6	70.2	66.4	19.9	17.5	21
Ce	56	30.1	152	134	45.1	40.5	47.4
Pr	8.15	4.52	20	17.2	6.41	5.84	6.78
Nd	34.1	20.9	77.4	63.4	28.5	25.9	30.6
Sm	7.27	5.24	13	10.4	7.3	6.49	7.86
Eu	2.53	1.8	2.97	2.27	2.38	2.14	2.54
Gd	8.09	6.81	10.7	8.93	9.52	8.53	10.3
Tb	1.29	1.07	1.46	1.18	1.52	1.44	1.62
Dy	7.53	6.21	7.43	6.1	8.93	8.55	9.4
Ho	1.48	1.21	1.3	1.1	1.78	1.67	1.88
Er	4.34	3.41	3.65	3.03	5.02	4.69	5.44
Tm	0.634	0.483	0.504	0.434	0.716	0.673	0.782
Yb	4.02	2.98	3.07	2.76	4.52	4.29	4.97
Lu	0.639	0.448	0.459	0.416	0.712	0.664	0.769
$(La/Yb)_{CN}$	4.4	3.0	16.4	17.3	3.2	2.9	3.0
$(La/Sm)_{CN}$	2.18	1.55	3.49	4.12	1.76	1.74	1.72
$(Gd/Yb)_{CN}$	1.66	1.89	2.88	2.68	1.74	1.64	1.71

Sample	09MM068	09MM086	09MM091	09MM110	09MM119	09MM137	HS09-1A
Rock Type	Diorite	Diorite	Diorite	Diorite	Diorite	Diorite	Dyke
Easting	500867	499323	500627	500509	500734	500388	515143
Northing	5504418	5504316	5504286	5504380	5504423	5503275	5534772
Drill Hole							
From							
To							
SiO_2	51.09	47.18	50.73	50.82	50.29	49.46	46.61
Al_2O_3	13.25	14.37	12.60	12.74	12.71	13.21	14.18
Fe_2O_3	6.56	3.10	4.95	4.63	6.25	4.04	5.40
FeO	7.85	8.84	9.12	10.06	8.48	9.38	7.11
MgO	4.60	6.70	4.08	4.02	4.27	5.20	6.49
CaO	7.08	10.59	8.18	8.13	7.70	8.23	10.10
Na_2O	3.04	2.40	3.09	2.71	2.96	3.05	1.06
K_2O	1.46	0.38	0.83	0.84	1.11	0.92	1.44
TiO_2	2.537	1.887	2.487	2.612	2.597	2.051	1.725
MnO	0.235	0.202	0.226	0.238	0.225	0.219	0.192
P_2O_5	0.355	0.181	0.410	0.368	0.320	0.257	0.172
LOI	1.15	1.77	1.17	0.62	1.29	1.02	2.74
Total	99.20	97.60	97.87	97.79	98.21	97.04	97.22
Fe_2O_3t	15.28	12.91	15.09	15.81	15.67	14.46	13.29
FeO*	13.75	11.62	13.58	14.23	14.11	13.01	11.96
CO_2	0.05	0.22	0.31	0.01	0.36	0.03	n/a
Mg#	34.92	48.03	32.51	31.18	32.67	39.08	46.54
Fe#	0.63	0.57	0.69	0.71	0.67	0.64	0.52
MALI	-2.59	-7.81	-4.26	-4.58	-3.64	-4.26	-7.60
Sc	37.4	41.7	38.3	37.1	36.3	40.6	n/a
V	388	308	393	357	376	348	275
Cr	10	130	10	10	10	30	100
Co	41	47	40	40	38	42	29
Ni	30	80	30	30	30	40	70
Cu	280	230	270	240	260	220	280
Zn	130	80	140	130	130	120	130
Pb	13	6	11	7	9	6	25
Au	1	5	8	1	1	4	n/a
Ag	0.25	0.25	0.5	0.25	0.25	0.25	0.25
Sn	2	0.5	2	2	2	1	0.5
Sb	2.5	1.2	0.1	0.6	0.9	0.8	0.1
W	0.25	1.5	5.1	2.1	2.4	4.3	0.25
F	282	155	266	319	204	1551	245
S	0.04	0.02	0.04	0.2	0.06	0.06	n/a
Tl	0.08	0.25	0.25	0.25	0.12	0.07	0.23
As	2.5	12	2.5	2.5	2.5	2.5	2.5
Cs	0.3	0.3	0.5	0.2	1.2	0.3	0.9
Ba	462	62	233	232	306	313	141
Rb	26	5	16	14	25	18	34
Sr	283	261	231	235	225	254	455
Th	2.49	0.68	2.67	2.48	2.32	1.48	1.03
U	0.76	0.16	0.77	0.77	0.7	0.44	0.4
Y	50.4	29.1	53.6	53.6	49.1	36	28.5
Zr	246	123	258	259	230	168	127

Sample	09MM068	09MM086	09MM091	09MM110	09MM119	09MM137	HS09-1A
Rock Type	Diorite	Diorite	Diorite	Diorite	Diorite	Diorite	Dyke
Easting	500867	499323	500627	500509	500734	500388	515143
Northing	5504418	5504316	5504286	5504380	5504423	5503275	5534772
Drill Hole							
From							
To							
Nb	14.4	7.8	12.8	16.4	14.6	10.4	8.7
Hf	5.6	3.1	6.1	5.9	5.3	4	3
Ta	0.94	0.55	0.97	1.01	0.98	0.63	0.55
Ga	21	18	20	21	20	19	19
Ge	1.8	1.8	1.6	1.7	1.7	1.7	2.2
La	19.9	8.51	21.2	22	19.6	15.3	13.3
Ce	45.7	21.2	49.4	51.1	45.7	35.1	29.2
Pr	6.7	3.34	7.14	7.45	6.61	5.05	3.88
Nd	29.7	16	32.6	33.3	29.6	22.9	17
Sm	7.57	4.48	8.14	8.35	7.46	5.76	4.28
Eu	2.44	1.61	2.52	2.55	2.42	1.93	1.46
Gd	9.62	6.01	10.6	10.4	9.6	7.51	5.68
Tb	1.56	0.98	1.68	1.68	1.5	1.21	0.87
Dy	9.11	5.79	9.99	9.9	8.96	6.99	5.34
Ho	1.8	1.11	1.95	1.96	1.82	1.39	1.07
Er	5.13	3.09	5.6	5.57	5.23	3.91	3.15
Tm	0.743	0.439	0.796	0.826	0.742	0.563	0.447
Yb	4.79	2.76	5.03	4.97	4.63	3.53	2.87
Lu	0.747	0.421	0.777	0.774	0.707	0.531	0.474
$(La/Yb)_{CN}$	3.0	2.2	3.0	3.2	3.0	3.1	3.3
$(La/Sm)_{CN}$	1.70	1.23	1.68	1.70	1.70	1.71	2.01
$(Gd/Yb)_{CN}$	1.66	1.80	1.74	1.73	1.72	1.76	1.64

Sample	09MM041	09MM046	09MM062	09MM103	09MM106	HS09-59C	09MM051
Rock Type	Dyke	Dyke	Dyke	Dyke	Dyke	Dyke	Mzg[2]
Easting	500582	500582	500582	500584	500554	500582	499657
Northing	5504442	5504431	5504431	5504443	5504539	5504566	5503874
Drill Hole	08-VK-01	08-VK-03	08-VK-05				
From	77.6	18.2	25.75				
To	77.83	18.5	26.1				
SiO_2	63.31	63.58	61.26	61.65	63.13	61.24	75.21
Al_2O_3	15.58	14.01	15.31	16.19	15.49	15.23	14.12
Fe_2O_3	1.60	0.69	0.97	2.50	1.74	1.68	0.63
FeO	1.90	2.42	2.27	2.28	1.65	1.70	0.01
MgO	2.05	1.76	1.63	1.40	1.84	1.68	0.12
CaO	3.64	3.65	3.44	2.57	3.37	3.80	0.25
Na_2O	3.73	2.77	2.91	4.91	4.10	3.43	4.57
K_2O	3.03	3.65	4.01	3.43	2.96	3.36	4.44
TiO_2	0.608	0.536	0.568	0.954	0.604	0.595	0.059
MnO	0.048	0.058	0.058	0.053	0.043	0.050	0.004
P_2O_5	0.192	0.161	0.175	0.310	0.187	0.170	0.009
LOI	4.47	6.06	6.13	2.36	4.50	6.46	0.39
Total	100.17	99.35	98.73	98.61	99.60	99.40	99.82
Fe_2O_3t	3.72	3.38	3.50	5.03	3.57	3.58	0.64
FeO*	3.34	3.04	3.15	4.53	3.21	3.22	0.57
CO_2	2.49	4.77	n/a	2.43	3.74	n/a	0.03
Mg#	49.52	48.15	45.45	33.22	47.87	45.50	25.62
Fe#	0.48	0.58	0.58	0.62	0.47	0.50	0.07
MALI	3.13	2.77	3.47	5.77	3.68	3.00	8.76
Sc	6.9	6.5	n/a	8.3	6.7	n/a	0.7
V	62	60	55	55	53	53	2.5
Cr	30	30	20	30	30	30	10
Co	10	9	7	10	9	7	0.5
Ni	20	20	20	10	20	30	10
Cu	20	5	5	10	10	20	5
Zn	50	40	50	70	60	60	120
Pb	14	58	11	8	16	14	42
Au	1	32	n/a	1	1	n/a	1
Ag	0.25	0.25	0.7	0.25	0.25	0.6	0.25
Sn	1	2	1	1	1	0.5	0.5
Sb	0.1	2.2	0.7	2	1.2	1.1	0.1
W	2.6	8.8	5.9	1.9	0.9	0.7	1.1
F	527	1274	1490	744	599	452	80
S	0.07	0.39	n/a	0.05	0.12	n/a	0.005
Tl	0.37	0.66	0.89	0.4	0.7	0.66	0.86
As	2.5	21	14	2.5	12	2.5	2.5
Cs	1.8	1.4	1.7	1.8	2.1	1.4	0.1
Ba	718	632	469	1300	797	1100	548
Rb	89	134	136	82	126	97	134
Sr	347	341	292	357	332	266	104
Th	10.5	9.84	10.2	10.4	10.3	9.46	3.53
U	2.43	2.29	2.47	2.23	2.21	2.13	5.15
Y	12.1	10.5	10.5	11.2	12	9.5	5.3
Zr	204	186	191	192	193	176	48

Sample	09MM041	09MM046	09MM062	09MM103	09MM106	HS09-59C	09MM051
Rock Type	Dyke	Dyke	Dyke	Dyke	Dyke	Dyke	Mzg[2]
Easting	500582	500582	500582	500584	500554	500582	499657
Northing	5504442	5504431	5504431	5504443	5504539	5504566	5503874
Drill Hole	08-VK-01	08-VK-03	08-VK-05				
From	77.6	18.2	25.75				
To	77.83	18.5	26.1				
Nb	6.3	6.6	6	6.4	6.5	5.4	4.5
Hf	4.3	3.9	4.2	4.2	4.3	3.9	1.9
Ta	0.44	0.38	0.4	0.42	0.41	0.37	0.13
Ga	21	23	22	20	19	19	20
Ge	1	1.8	2.1	1	1	1	1
La	39.2	36.6	38.9	44.2	42.3	37.3	1.94
Ce	73.9	68.9	74	74.8	75.6	70.2	4.51
Pr	8.58	7.93	7.91	9.11	8.89	7.47	0.44
Nd	30.3	27.4	27	31.8	30.8	25.7	1.8
Sm	4.81	4.24	4.22	4.74	4.55	4.01	0.52
Eu	1.23	1.05	1.01	1.16	1.16	1.03	0.336
Gd	3.8	3.41	3.13	3.71	3.69	3.12	0.73
Tb	0.48	0.43	0.38	0.46	0.46	0.37	0.14
Dy	2.35	2.17	2.15	2.34	2.33	1.97	1
Ho	0.42	0.38	0.37	0.41	0.41	0.36	0.22
Er	1.09	1.04	1.05	1.13	1.11	1.01	0.65
Tm	0.152	0.144	0.145	0.155	0.151	0.134	0.094
Yb	0.95	0.88	0.9	0.9	0.91	0.82	0.57
Lu	0.136	0.127	0.143	0.131	0.135	0.123	0.078
$(La/Yb)_{CN}$	29.6	29.8	31.0	35.2	33.3	32.6	2.4
$(La/Sm)_{CN}$	5.26	5.57	5.95	6.02	6.00	6.00	2.41
$(Gd/Yb)_{CN}$	3.31	3.21	2.88	3.41	3.35	3.15	1.06

Sample	09MM055	09MM099	09MM109	09MM111	09MM113	09MM114	09MM120
Rock Type	Mzg[2]	Mzg[2]	Mzg[2]	Mzg[2]	Mzg[2]	Mzg[2]	Apsy
Easting	500651	500578	500553	500521	500598	500545	514355
Northing	5504651	5504453	5504528	5504452	5504175	5504137	5532860
Drill Hole	08-VK-04						
From	29.8						
To	30.4						
SiO_2	72.83	72.08	74.91	74.35	74.44	71.53	61.55
Al_2O_3	13.94	13.96	13.77	13.53	13.92	14.47	15.55
Fe_2O_3	n/a	0.34	0.47	n/a	0.66	0.52	2.42
FeO	n/a	0.87	0.18	n/a	0.37	0.80	3.03
MgO	0.53	0.32	0.14	0.13	0.18	0.32	1.84
CaO	0.78	0.77	0.15	0.13	0.09	0.97	2.53
Na_2O	3.14	3.84	4.24	3.40	3.07	3.66	3.40
K_2O	6.10	4.90	4.83	5.53	5.96	5.34	4.21
TiO_2	0.086	0.144	0.070	0.091	0.099	0.183	1.168
MnO	0.010	0.014	0.006	0.004	0.005	0.023	0.062
P_2O_5	0.023	0.031	0.009	0.031	0.023	0.051	0.394
LOI	1.23	0.71	0.60	0.90	0.88	0.65	1.72
Total	98.67	97.99	99.39	98.10	99.70	98.51	97.88
Fe_2O_3t	0.93	1.31	0.68	0.71	1.08	1.41	5.79
FeO*	n/a	1.18	0.61	n/a	0.97	1.27	5.21
CO_2	0.56	1.66	0.03	0.04	0.02	0.03	0.17
Mg#	50.16	30.15	26.28	25.37	22.60	28.45	36.20
Fe#		0.73	0.58		0.68	0.72	0.62
MALI	8.45	7.97	8.92	8.81	8.93	8.02	5.08
Sc	0.70	0.6	1.0	0.6	0.9	1.2	13.0
V	2.5	7	2.5	2.5	2.5	7	58
Cr	10	10	10	10	10	10	10
Co	0.5	0.5	0.5	0.5	0.5	0.5	9
Ni	10	10	10	10	10	10	10
Cu	10	5	5	90	10	5	10
Zn	15	15	15	15	15	30	100
Pb	43	29	27	62	37	36	27
Au	190	1	28	647	59	1	1
Ag	0.25	0.25	0.25	0.25	0.25	0.25	1.1
Sn	8	0.5	0.5	0.5	0.5	0.5	2
Sb	0.1	0.1	0.1	0.5	1.7	0.8	1.5
W	2.2	0.25	0.25	62.3	9.8	4.2	8.5
F	275	160	115	303	375	251	769
S	0.28	0.02	0.01	0.24	0.04	0.03	0.02
Tl	0.69	0.65	0.5	0.76	0.97	0.96	0.53
As	32	2.5	2.5	21	5	2.5	2.5
Cs	0.5	0.4	0.2	0.5	1	0.4	0.9
Ba	995	1300	727	934	1010	1790	1650
Rb	113	111	82	120	146	146	94
Sr	180	287	135	108	96	361	282
Th	10.7	3.15	5.21	8.93	9.65	14	4.71
U	17.7	1.25	4.16	10	5.37	1.55	2.03
Y	4.8	3.9	5.5	5.5	6.1	3.8	45.6
Zr	91	162	49	121	106	151	619

Sample	09MM055	09MM099	09MM109	09MM111	09MM113	09MM114	09MM120
Rock Type	Mzg[2]	Mzg[2]	Mzg[2]	Mzg[2]	Mzg[2]	Mzg[2]	Apsy
Easting	500651	500578	500553	500521	500598	500545	514355
Northing	5504651	5504453	5504528	5504452	5504175	5504137	5532860
Drill Hole	08-VK-04						
From	29.8						
To	30.4						
Nb	1	2	1.8	1.4	2.3	2.3	22
Hf	2.5	4.2	1.5	3.4	3	3.7	13
Ta	0.02	0.08	0.05	0.02	0.03	0.03	1.3
Ga	19	18	17	16	19	20	25
Ge	1.3	1	1	1.5	1.7	1	1.5
La	15	12.2	5.06	14.6	14.6	37.3	66.3
Ce	28.4	24.6	9.61	26.2	23.7	56.8	137
Pr	3.55	2.11	1.09	3.24	2.76	6.59	17.8
Nd	13.6	7.14	4.19	12.1	9.61	21.6	70.7
Sm	2.72	1.08	0.99	2.36	1.76	2.67	12.8
Eu	0.742	0.605	0.464	0.625	0.618	0.951	3.45
Gd	2.23	0.82	1.26	2.21	1.7	1.53	12.2
Tb	0.25	0.11	0.21	0.28	0.25	0.15	1.73
Dy	1.14	0.63	1.26	1.39	1.32	0.67	9.03
Ho	0.18	0.12	0.24	0.24	0.23	0.12	1.66
Er	0.41	0.36	0.64	0.58	0.59	0.3	4.67
Tm	0.055	0.06	0.089	0.08	0.079	0.045	0.665
Yb	0.34	0.45	0.55	0.51	0.51	0.33	4.12
Lu	0.051	0.08	0.08	0.079	0.073	0.059	0.629
$(La/Yb)_{CN}$	31.6	19.4	6.6	20.5	20.5	81.1	11.5
$(La/Sm)_{CN}$	3.56	7.29	3.30	3.99	5.36	9.02	3.34
$(Gd/Yb)_{CN}$	5.43	1.51	1.90	3.58	2.76	3.84	2.45

Sample	09MM121	09MM122	09MM125	09MM126	HS09-107	HS09-108
Rock Type	Apsy	Apsy	DRG[3]	DRG[3]	GLIS[4]	GLIS[5]
Easting	513356	511797	505431	505741	500586	500567
Northing	5530438	5526194	5514440	5513849	5495501	5494834
Drill Hole						
From						
To						
SiO_2	58.47	72.95	71.77	71.27	64.74	60.96
Al_2O_3	14.65	13.02	14.35	14.43	16.05	15.73
Fe_2O_3	3.43	1.24	0.64	0.70	1.36	3.06
FeO	4.38	1.33	0.82	0.90	2.81	3.52
MgO	1.89	0.65	0.59	0.85	0.86	1.28
CaO	4.48	1.03	1.62	0.89	2.00	2.92
Na_2O	3.74	3.09	4.00	4.14	4.59	4.03
K_2O	3.28	5.65	4.23	4.43	4.88	4.00
TiO_2	1.712	0.333	0.260	0.290	0.768	1.132
MnO	0.138	0.024	0.035	0.036	0.115	0.173
P_2O_5	0.634	0.077	0.104	0.099	0.180	0.302
LOI	1.42	1.32	0.52	1.04	0.58	0.76
Total	98.23	100.71	98.94	99.08	98.94	97.88
Fe_2O_3t	8.30	2.71	1.55	1.70	4.49	6.97
FeO*	7.47	2.44	1.40	1.53	4.04	6.27
CO_2	0.09	0.67	0.005	0.12	0.03	n/a
Mg#	28.84	29.96	40.46	47.19	25.46	24.64
Fe#	0.70	0.67	0.58	0.51	0.77	0.73
MALI	2.54	7.71	6.62	7.68	7.47	5.11
Sc	16.0	4.3	3.4	3.4	12.0	n/a
V	69	8	20	21	23	39
Cr	10	10	10	10	10	10
Co	13	2	3	3	4	5
Ni	10	10	10	10	10	10
Cu	5	5	5	5	5	5
Zn	160	15	30	15	90	100
Pb	21	15	45	29	32	13
Au	1	1	1	1	1	n/a
Ag	1.5	0.5	0.25	0.25	1.5	2.7
Sn	2	0.5	1	0.5	2	2
Sb	0.1	0.5	1.2	0.4	0.1	0.1
W	3.1	1	7.8	1.2	2.6	0.25
F	1155	351	578	311	462	360
S	0.07	0.01	0.005	0.005	0.005	n/a
Tl	0.49	0.79	1.04	0.94	0.5	0.51
As	2.5	2.5	2.5	2.5	2.5	2.5
Cs	1	0.4	7.2	5.7	2.2	1.9
Ba	1810	902	533	444	1960	1290
Rb	78	145	202	182	106	78
Sr	464	166	304	246	168	183
Th	7.03	9.7	22.7	19.5	8.24	6.8
U	3.23	2.75	7.56	5.64	1.9	2.01
Y	56	33.7	8	7.4	45.9	41.8
Zr	826	330	157	133	764	726

Sample	09MM121	09MM122	09MM125	09MM126	HS09-107	HS09-108
Rock Type	Apsy	Apsy	DRG[3]	DRG[3]	GLIS[4]	GLIS[5]
Easting	513356	511797	505431	505741	500586	500567
Northing	5530438	5526194	5514440	5513849	5495501	5494834
Drill Hole						
From						
To						
Nb	32.2	15.3	17.1	11.6	23.2	19.3
Hf	18.2	8.2	4.3	3.4	14.3	13.5
Ta	1.84	0.85	1.83	1.23	1.43	1.25
Ga	24	20	22	20	21	21
Ge	1.7	1.4	1.4	1.3	1.7	1.9
La	87.7	79.8	37.6	25.2	42.3	45
Ce	181	158	68.1	48	88.6	93.9
Pr	24.5	19.2	7.29	5.32	11.7	11.6
Nd	95.7	68.1	22.8	17.7	45.9	45.8
Sm	17.6	11.5	3.24	2.66	9.03	9.04
Eu	4.18	1.58	0.652	0.624	3.27	3.6
Gd	16.7	9.78	2.4	2.15	9.79	9.77
Tb	2.33	1.4	0.31	0.28	1.48	1.36
Dy	12	7.32	1.5	1.44	8.56	7.97
Ho	2.18	1.3	0.27	0.26	1.71	1.55
Er	6	3.46	0.77	0.72	4.87	4.63
Tm	0.849	0.475	0.112	0.105	0.713	0.676
Yb	5.3	2.88	0.73	0.69	4.46	4.27
Lu	0.807	0.439	0.116	0.107	0.673	0.65
$(La/Yb)_{CN}$	11.9	19.9	36.9	26.2	6.8	7.6
$(La/Sm)_{CN}$	3.22	4.48	7.49	6.12	3.02	3.21
$(Gd/Yb)_{CN}$	2.61	2.81	2.72	2.58	1.82	1.89

Table B.2: Mass gain and loss calculation after Grant (1986) for the most altered sample 09MM058 (C^o) and the least altered sample 09MM042 (C^a).

		C^o	C^a	$\Delta C_i/C_i^o$			C^o	C^a	$\Delta C_i/C_i^o$
Majors	SiO2/20	3.06	3.19	0.04	**REE's**	La/100	0.93	0.92	-0.01
(%)	Al2O3/3	2.78	4.63	0.40	**(ppm)**	Ce/100	2.12	1.89	-0.12
	Fe2O3	2.22	1.33	-0.67		Pr	30.20	24.88	-0.21
	FeO	2.71	2.42	-0.12		Nd/100	1.14	0.91	-0.25
	MgO	1.64	0.92	-0.78		Sm	19.00	15.70	-0.21
	CaO	3.14	3.47	0.09		Eu	3.24	2.57	-0.26
	Na2O	4.31	3.01	-0.43		Gd	15.70	13.26	-0.18
	K2O	4.75	4.40	-0.08		Tb	2.28	1.82	-0.25
	TiO2	0.99	0.84	-0.18		Dy	12.40	10.57	-0.17
	MnO	0.09	0.07	-0.23		Ho	2.41	1.96	-0.23
	P2O5	0.34	0.24	-0.39		Er	7.06	5.73	-0.23
	LOI	1.08	4.56	0.76		Tm	1.03	0.81	-0.27
	Fe2O3t	5.23	4.03	-0.30		Yb	6.33	4.87	-0.30
	FeO*	4.71	3.62	-0.30		Lu	0.93	0.77	-0.20
	CO2	0.19	0.70	0.73					
Traces	Sc	7.20	8.18	0.12					
(ppm)	V	60.00	51.00	-0.18					
Au (ppb)	Cr	10.00	10.00	0.00					
	Co	9.00	6.00	-0.50					
	Cu	20.00	47.50	0.58					
	Zn/100	1.10	2.68	0.59					
	Pb/100	0.29	1.64	0.82					
	Au/1000	0.01	3.13	1.00					
	Ag	1.50	2.75	0.45					
	Sn	5.00	4.50	-0.11					
	Sb	0.40	1.15	0.65					
	Tl	1.02	0.91	-0.12					
	As	2.50	68.25	0.96					
	W	2.90	15.85	0.82					
	Cs	0.90	1.05	0.14					
	Ba/1000	2.50	1.33	-0.89					
	Rb/150	0.97	0.78	-0.24					
	Sr/100	5.73	3.03	-0.89					
	Th	11.10	11.46	0.03					
	U	3.38	2.45	-0.38					
	Y	70.20	53.18	-0.32					
	Zr/100	6.74	4.72	-0.43					
	Nb/5	5.04	3.48	-0.45					
	Hf	13.90	10.23	-0.36					
	Ta	1.85	1.33	-0.39					
	Ga/5	5.00	4.80	-0.04					
	Ge	1.50	2.18	0.31					

APPENDIX C

ARGON THERMOCHRONOLOGICAL DATA

Table C.1 (Below): ^{40}Ar-^{39}Ar analytical data. Asterisks denote steps excluded from plateau and inverse-correlation age calculations. J-values were determined through interpolation. [a]: As measured by laser in % of full nominal power (10W), [b]: Fraction 39Ar as percent of total run, c - Errors are analytical only and do not reflect error in irradiation parameter J, d - Nominal J-value, referenced to PP-20 (Hb3gr) = 1072 Ma (Roddick, 1983), * - Step not included in plateau or inverse isotope correlation age determination. All uncertainties quoted at 2σ level.

Power[a]	$^{36}Ar/^{39}Ar$	$^{40}Ar/^{39}Ar$	% ^{40}Ar ATM	$*^{40}Ar/^{39}Ar$	Ca/K	f_{39}[b] (%)	Apparent Age Ma[c]
09MM024 Biotite; J[d] = 0.016889 ± 0.000034							
* 1.8	0.001453 ± 0.001191	0.063083 ± 0.003169	42.83	9.05 ± 5.62	0.000	0.11	256.6 ± 148.6
* 2.0	0.000789 ± 0.000295	0.083174 ± 0.00152	23.24	9.22 ± 1.06	0.012	0.67	261.1 ± 28.1
* 2.2	0.000114 ± 0.000032	0.062978 ± 0.000468	3.37	15.34 ± 0.19	0.007	4.32	415.7 ± 4.5
2.3	0.00004 ± 0.000035	0.063514 ± 0.000583	1.18	15.56 ± 0.22	0.000	4.01	420.9 ± 5.2
2.4	0.000044 ± 0.000024	0.063788 ± 0.000391	1.29	15.47 ± 0.15	0.010	6.37	418.9 ± 3.6
2.5	0.000026 ± 0.000021	0.06425 ± 0.000381	0.76	15.45 ± 0.13	0.015	5.89	418.2 ± 3.2
2.6	0.000011 ± 0.000026	0.064294 ± 0.000433	0.33	15.5 ± 0.16	0.000	5.53	419.5 ± 3.8
2.7	0.000015 ± 0.00004	0.064085 ± 0.000554	0.45	15.53 ± 0.23	0.000	3.55	420.3 ± 5.5
2.9	0.000044 ± 0.000026	0.064051 ± 0.000442	1.31	15.41 ± 0.16	0.015	4.53	417.3 ± 3.9
3.1	0.000015 ± 0.000027	0.063963 ± 0.000555	0.44	15.57 ± 0.18	0.032	6.83	421.1 ± 4.4
3.3	0.000003 ± 0.000022	0.064443 ± 0.000422	0.08	15.51 ± 0.14	0.015	12.44	419.6 ± 3.5
3.5	0.000011 ± 0.000017	0.064554 ± 0.000488	0.34	15.44 ± 0.14	0.016	18.13	418 ± 3.4
3.7	0.00001 ± 0.000018	0.064148 ± 0.000427	0.30	15.54 ± 0.13	0.014	15.96	420.5 ± 3.2
3.9	0.000004 ± 0.000019	0.06445 ± 0.000473	0.13	15.5 ± 0.14	0.017	9.42	419.4 ± 3.5
* 4.2	0.000023 ± 0.000074	0.06282 ± 0.000724	0.68	15.81 ± 0.39	0.091	1.90	427 ± 9.5
* 4.8	0.00005 ± 0.000427	0.058005 ± 0.001718	1.46	16.99 ± 2.25	0.311	0.25	455.1 ± 53.2
* 6.0	0.00051 ± 0.000996	0.049528 ± 0.00214	15.05	17.15 ± 6.02	0.000	0.10	458.8 ± 142.1
09MM113 Sericite; J[d] = 0.016896 ± 0.000034							
* 1.8	0.000324 ± 0.00013	0.025772 ± 0.000707	9.51	35.11 ± 1.79	0.0490	0.64	840.2 ± 34.3
* 2.0	0.000039 ± .000036	0.074391 ± 0.000704	1.15	13.29 ± 0.19	0.0050	5.2	365.4 ± 4.7
* 2.2	0.000011 ± 0.000026	0.074199 ± 0.000549	0.32	13.43 ± 0.14	0.0130	6.9	369 ± 3.6
* 2.3	0.000009 ± 0.000031	0.072614 ± 0.000572	0.27	13.73 ± 0.17	0.0000	5.8	376.5 ± 4.2
2.5	0.000024 ± 0.000029	0.070769 ± 0.000559	0.72	14.03 ± 0.16	0.0250	6.79	383.7 ± 4.1
2.7	0.000036 ± 0.000072	0.071382 ± 0.000647	1.06	13.86 ± 0.33	0.0230	5.57	379.6 ± 8
2.9	0.000026 ± 0.00002	0.070763 ± 0.000413	0.77	14.02 ± 0.12	0.0090	14.37	383.6 ± 2.9
3.0	0.000018 ± 0.000017	0.070702 ± 0.000394	0.54	14.07 ± 0.11	0.0180	25.73	384.7 ± 2.6
3.1	0.000013 ± 0.000022	0.070304 ± 0.000444	0.38	14.17 ± 0.13	0.0170	9.25	387.2 ± 3.2
* 3.2	0.000033 ± 0.000032	0.068929 ± 0.00065	0.97	14.37 ± 0.19	0.0060	5.67	392.1 ± 4.8
* 3.3	0.000037 ± 0.000029	0.068981 ± 0.000595	1.09	14.34 ± 0.18	0.0200	5.52	391.4 ± 4.3
* 3.6	0.000056 ± 0.000068	0.066985 ± 0.000902	1.64	14.68 ± 0.36	0.1140	2.84	399.8 ± 8.8
* 6.0	0.000036 ± 0.000034	0.06811 ± 0.000525	1.06	14.53 ± 0.19	0.0100	5.72	396 ± 4.6

Power[a]	$^{36}Ar/^{39}Ar$	$^{40}Ar/^{39}Ar$	% ^{40}Ar ATM	$*^{40}Ar/^{39}Ar$	Ca/K	f_{39}[b] (%)	Apparent Age Ma[c]
09MM099 Sericite; J[d] = 0.016829 ± 0.000034							
* 1.8	0.000317 ± 0.000092	0.022979 ± 0.000517	9.32	39.46 ± 1.49	0.179	0.84	921.5 ± 27.2
* 2.0	0.000047 ± 0.000042	0.071070 ± 0.000672	1.40	13.87 ± 0.22	0.030	5.28	379.8 ± 5.4
* 2.2	0.000022 ± 0.000026	0.073014 ± 0.000590	0.65	13.61 ± 0.15	0.020	8.11	373.2 ± 3.8
* 2.3	0.000022 ± 0.000039	0.072458 ± 0.000597	0.65	13.71 ± 0.20	0.037	5.32	375.8 ± 4.9
* 2.5	0.000039 ± 0.000031	0.071194 ± 0.000614	1.16	13.88 ± 0.18	0.050	6.82	380.1 ± 4.4
* 2.7	0.000038 ± 0.000025	0.070340 ± 0.000411	1.13	14.06 ± 0.13	0.044	7.57	384.3 ± 3.3
* 2.8	0.000027 ± 0.000020	0.068624 ± 0.000460	0.79	14.46 ± 0.13	0.039	16.19	394.2 ± 3.2
* 2.9	0.000035 ± 0.000021	0.067323 ± 0.000490	1.04	14.70 ± 0.14	0.039	13.45	400.1 ± 3.5
* 3.0	0.000025 ± 0.000020	0.068043 ± 0.000482	0.75	14.59 ± 0.14	0.032	11.83	397.4 ± 3.3
* 3.1	0.000034 ± 0.000029	0.067488 ± 0.000535	1.00	14.67 ± 0.17	0.041	7.34	399.4 ± 4.2
3.2	0.000054 ± 0.000024	0.065466 ± 0.000465	1.57	15.03 ± 0.15	0.067	7.95	408.3 ± 3.7
3.3	0.000104 ± 0.000080	0.064199 ± 0.000762	3.05	15.10 ± 0.41	0.102	2.30	409.9 ± 10.0
3.6	0.000078 ± 0.000082	0.065899 ± 0.000832	2.29	14.83 ± 0.41	0.096	2.22	403.2 ± 10.1
6.0	0.000058 ± 0.000044	0.064951 ± 0.000627	1.72	15.13 ± 0.25	0.060	4.78	410.6 ± 6.0
09MM098 Sericite; J[d] = 0.016894 ± 0.000034							
* 1.6	0.000798 ± 0.000509	0.015801 ± 0.000966	23.48	48.42 ± 10.11	0.118	0.04	1078.3 ± 169.6
* 1.9	0.000244 ± 0.000114	0.021300 ± 0.000582	7.11	43.61 ± 2.00	0.169	0.18	995.8 ± 35.1
* 2.1	0.000052 ± 0.000020	0.067359 ± 0.000489	1.52	14.62 ± 0.14	0.503	4.56	398.2 ± 3.4
* 2.3	0.000026 ± 0.000017	0.073414 ± 0.000424	0.76	13.52 ± 0.11	0.641	7.14	371.1 ± 2.6
2.5	0.000015 ± 0.000020	0.072440 ± 0.000624	0.44	13.74 ± 0.15	0.162	7.50	376.7 ± 3.6
2.7	0.000015 ± 0.000020	0.072317 ± 0.000502	0.44	13.77 ± 0.13	0.063	7.07	377.3 ± 3.1
2.8	0.000011 ± 0.000024	0.072598 ± 0.000497	0.34	13.73 ± 0.14	0.042	4.99	376.3 ± 3.4
2.9	0.000018 ± 0.000020	0.072562 ± 0.000464	0.54	13.71 ± 0.12	0.056	4.58	375.8 ± 3.0
3.0	0.000010 ± 0.000016	0.072288 ± 0.000478	0.30	13.79 ± 0.11	0.040	6.66	377.9 ± 2.8
3.1	0.000016 ± 0.000015	0.072103 ± 0.000481	0.48	13.80 ± 0.11	0.046	6.76	378.1 ± 2.7
* 3.2	0.000014 ± 0.000017	0.071447 ± 0.000503	0.40	13.94 ± 0.12	0.026	9.37	381.5 ± 3.0
* 3.3	0.000009 ± 0.000014	0.071406 ± 0.000454	0.26	13.97 ± 0.11	0.033	8.48	382.2 ± 2.6
* 3.4	0.000020 ± 0.000018	0.071183 ± 0.000425	0.57	13.97 ± 0.11	0.027	7.03	382.2 ± 2.8
* 3.5	0.000008 ± 0.000017	0.070833 ± 0.000512	0.24	14.08 ± 0.13	0.060	7.45	385.1 ± 3.1
* 3.7	0.000013 ± 0.000019	0.070691 ± 0.000485	0.37	14.09 ± 0.13	0.099	6.64	385.3 ± 3.1
* 3.9	0.000016 ± 0.000019	0.070413 ± 0.000485	0.47	14.14 ± 0.13	0.103	3.81	386.3 ± 3.1
* 4.2	0.000011 ± 0.000034	0.070265 ± 0.000529	0.31	14.19 ± 0.18	0.086	2.45	387.6 ± 4.4
* 6.0	0.000017 ± 0.000018	0.070057 ± 0.000434	0.50	14.20 ± 0.12	0.065	5.30	388.0 ± 2.9

APPENDIX D

MICROTHERMOMETRIC DATA

Table D.1: Microthermometric data for the Viking deposit gold occurrences. Key: Thor vein mineralized (09MM043), Thor vein barren (09MM105), Viking trend stockwork (09MM081), North Thor mineralized (09MM108), and Valhalla mineralized (09MM167). Th_{TOT}, Th_{CO2}, Tm_{clath}, and Tm_{CO2} are given in degrees Celsius. Pressure of formation given in Kbars and depths in kilometers. Homogenization to a particular phase is given in the phase column (v=vapor, l=liquid, and d=decrepitated).

Sample	Type	FIA	#	F	Tm_{CO2}	Tm_{Clath}	Th_{CO2}	Th_{TOT}	phase	salinity	x CO_2	ρ (g/cc)	Kbar	Depth
Vein High-grade														
09MM043	1	4a	1	0.5	-56.8	6.6	25.3	315.0	v	8.7	0.25	0.84	2.04	7
09MM043	1	4a	2	0.5	-56.8	6.6	24.2	315.0	v	8.7	0.26	0.85	2.13	7
09MM043	1	7a	1	0.6	-57.5	6.8	22.4	318.0	v	8.3	0.20	0.89	2.58	9
09MM043	1	7a	2	0.5	-57.5	6.8	21.1	318.0	v	8.3	0.26	0.87	2.38	8
09MM043	1	6	1	0.5	-57.7	6.2	28.6	319.0	v	9.4	0.23	0.81	1.71	6
09MM043	1	6	2	0.5	-57.7	6.2	26.7	319.0	v	9.4	0.24	0.83	1.92	6
09MM043	1	6	3	0.5	-57.7	6.2	25.0	315.0	v	9.4	0.25	0.84	2.07	7
09MM043	1	6	4	0.5	-57.7	6.2	24.1	315.0	v	9.4	0.26	0.85	2.14	7
09MM043	2	3	1	0.7	-56.8	6.6	29.4	312.5	v	8.7	0.12	0.87	2.26	8
09MM043	2	3	2	0.7	-56.8	6.6	28.0	312.5	v	8.7	0.13	0.88	2.35	8
09MM043	2	3	3	0.65	-56.8	6.6	29.0	312.5	v	8.7	0.15	0.86	2.03	7
09MM043	2	4	1	0.5	-56.8	6.6	28.0	312.0	v	8.7	0.24	0.82	1.70	6
09MM043	2	4	2	0.5	-56.8	6.6	28.0	312.0	v	8.7	0.24	0.82	1.75	6
09MM043	2	4	3	0.5	-56.8	6.6	24.2	312.0	v	8.7	0.26	0.85	2.12	7
09MM043	2	7	1	0.6	-57.5	6.8	19.5	282.2	d	8.3	0.20	0.90	2.71	9
09MM043	2	7	2	0.7	-57.5	6.8	17.7	287.9	d	8.3	0.15	0.93	3.08	10
09MM043	2	7	3	0.5	-57.5	6.8	19.0	280.0	d	8.3	0.27	0.88	2.45	8
Thor Vein Barren														
09MM105	2	1	1	0.5	-56.3	6.6	25.6	295.0	v	8.7	0.25	0.84	2.54	8
09MM105	2	1	2	0.55	-56.3	6.6	23.5	305.2	v	8.7	0.22	0.87	2.30	8
09MM105	2	1	3	0.6	-56.3	6.6	25.6	297.5	v	8.7	0.19	0.87	2.23	7
09MM105	2	2b	1	0.65	-56.6	6.6	14.0	265.0	d	8.7	0.18	0.93	3.32	11
09MM105	2	2b	2	0.5	-56.6	6.6	13.5	265.0	v	8.7	0.28	0.91	2.85	9
09MM105	2	2c	1	0.65	-56.9	6.6	26.2	290.0	v	8.7	0.16	0.88	2.30	8
09MM105	2	2c	2	0.55	-56.9	6.6	25.5	290.0	v	8.7	0.22	0.86	2.13	7
09MM105	2	2c	3	0.5	-56.9	6.6	24.4	290.0	v	8.7	0.25	0.85	2.07	7
Viking Trend														
09MM081	2	11	1	0.75	-58.6	8.4	30.0	282.3	l	5.5	0.10	0.89	2.14	7
09MM081	2	11	2	0.75	-58.6	8.4	29.5	282.3	l	5.5	0.11	0.90	2.24	7
09MM081	2	11	3	0.65	-58.6	7.4	30.0	287.0	l	7.3	0.14	0.85	1.77	6
09MM081	2	11	4	0.6	-58.6	7.4	30.0	276.4	v	7.3	0.17	0.83	1.67	6
09MM081	2	13	1	0.5	-57	8.0	26.8	318.0	d	6.2	0.25	0.83	1.89	6

Table D.1 Continued.

Sample		FIA	#	F	Tm_{CO2}	Tm_{Clath}	Th_{CO2}	Th_{TOT}	phase	salinity	x CO_2	ρ (g/cc)	Kbar	Depth
09MM081	2	13	2	0.6	-57	8.0	25.5	316.0	v	6.2	0.19	0.87	2.29	8
09MM081	2	13	3	0.6	-57	8.0	26.4	320.0	v	6.2	0.19	0.87	2.23	7
09MM081	2	13	4	0.7	-57	8.0	23.5	319.0	v	6.2	0.14	0.91	2.86	10
09MM081	2	12	1	0.55	-58.8	6.8	24.0	256.8	v	8.3	0.22	0.87	2.40	8
09MM081	2	12	2	0.7	-58.8	6.8	30.6	262.9	l	8.3	0.12	0.85	1.92	6
09MM081	2	12	3	0.65	-58.8	6.8	26.3	256.8	v	8.3	0.16	0.88	2.52	8
09MM081	2	12	4	0.6	-58.8	6.8	28.0	256.8	v	8.3	0.18	0.85	2.18	7
09MM081	2	12	5	0.5	-58.8	6.8	30.6	268.0	l	8.3	0.21	0.77	1.35	4
09MM081	2	12	6	0.55	-58.8	7	28.0	264.2	v	8.0	0.21	0.84	1.94	6
North Thor Mineralized														
09MM108	2	21	1	0.5	-58.4	6.6	26.4	271.0	v	8.7	0.25	0.83	1.93	6
09MM108	2	21	2	0.55	-58.4	6.6	27.8	265.0	l	8.7	0.21	0.84	1.99	7
09MM108	2	21	3	0.5	-58.4	6.6	27.8	267.8	v	8.7	0.24	0.82	1.81	6
09MM108	2	22	1	0.55	-57.8	6.8	9.7	290.0	v	7.1	0.28	0.91	2.80	9
09MM108	2	22	2	0.5	-57.8	7.5	12.7	290.0	v	7.1	0.28	0.91	2.80	9
09MM108	2	22	3	0.5	-57.8	7.5	12.7	290.0	v	7.1	0.28	0.91	2.80	9
09MM108	2	22	4	0.5	-57.8	7.5	12.7	290.0	v	7.1	0.28	0.91	2.80	9
Valhalla Mineralization														
09MM167	2	15	1	0.5	-55.9	6.6	19.7	237.0	v	8.7	0.27	0.88	2.74	9
09MM167	2	15	2	0.5	-55.9	7.0	17.5	237.0	v	8.0	0.27	0.89	2.81	9
09MM167	2	15	3	0.5	-55.9	7.0	16.1	237.0	v	8.0	0.28	0.90	2.89	10
09MM167	2	17	1	0.5	-56.9	7.7	19.0	278.1	v	6.8	0.27	0.89	2.40	8
09MM167	2	17	2	0.6	-56.9	7.7	19.2	270.0	v	6.8	0.20	0.90	2.71	9
09MM167	2	17	3	0.6	-56.9	7.7	21.3	270.0	v	6.8	0.23	0.88	2.42	8
09MM167	1	16	1	0.55	-56.9	6.8	22.8	317.6	v	8.3	0.23	0.87	2.40	8
09MM167	1	16	2	0.6	-56.9	6.8	29.3	317.6	v	8.3	0.17	0.84	1.86	6
09MM167	1	16	2	0.55	-56.9	6.8	28.6	317.6	v	8.3	0.20	0.83	1.83	6

APPENDIX E

STABLE ISOTOPE DATA

Table E.1: *In-situ* SIMS sulfur isotope data for the different gold occurrences of the Viking deposit. Analysis of $\delta^{34}S$ is given in per mil (‰) referenced against the Vienna Canyon Diablo Troilite (VCDT) with the corresponding 1 sigma (σ) error.

Analysis	Location	Mineral	$\delta^{34}S$	1σ	Analysis	Location	Mineral	$\delta^{34}S$	1σ
043-2A-1	Thor Vein	pyr	6.4	0.2	081-2-3	Viking Trend	cpy	6.0	0.2
043-2A-2	Thor Vein	pyr	6.7	0.4	081-2-4	Viking Trend	cpy	3.4	0.3
043-2A-3	Thor Vein	pyr	7.4	0.2	081-2-5	Viking Trend	cpy	1.9	0.3
043-2A-4	Thor Vein	pyr	8.2	0.2	081-2-6	Viking Trend	cpy	5.8	0.4
043-2C-1	Thor Vein	pyr	7.5	0.2	081-2-7	Viking Trend	cpy	1.0	0.3
043-2C-2	Thor Vein	pyr	7.4	0.3	081-2-8	Viking Trend	cpy	6.2	0.4
043-2C-3	Thor Vein	pyr	6.8	0.2	081-2-9	Viking Trend	cpy	3.5	0.2
043-2C-4	Thor Vein	pyr	6.5	0.3	043-2c-1	Thor Vein	gal	11.5	0.4
043-2C-5	Thor Vein	pyr	6.8	0.2	043-2c-2	Thor Vein	gal	10.7	0.2
043-2C-6	Thor Vein	pyr	5.0	0.2	056-1-1	Thor Vein	gal	14.0	0.2
043-2C-7	Thor Vein	pyr	7.4	0.2	056-1-2	Thor Vein	gal	14.4	0.3
043-2C-8	Thor Vein	pyr	6.5	0.2	056-1-3	Thor Vein	gal	12.3	0.3
043-2C-9	Thor Vein	pyr	7.1	0.2	056-1-4	Thor Vein	gal	11.8	0.3
043-2C-10	Thor Vein	pyr	4.7	0.2	056-1-5	Thor Vein	gal	15.6	0.2
043-2C-11	Thor Vein	pyr	6.3	0.2	108-1-1	North Thor	gal	20.8	0.3
108-1-1	North Thor	pyr	3.0	0.2	108-1-2	North Thor	gal	20.1	0.3
108-1-2	North Thor	pyr	2.1	0.3	108-1-3	North Thor	gal	20.9	0.3
108-1-3	North Thor	pyr	2.1	0.2	108-1-4	North Thor	gal	15.6	0.2
108-1-4	North Thor	pyr	3.7	0.4	056-1-1	Thor Vein	pyr	8.3	0.3
108-1-5	North Thor	pyr	2.0	0.2	056-1-2	Thor Vein	pyr	4.1	0.3
108-1-6	North Thor	pyr	4.2	0.3	056-1-3	Thor Vein	pyr	8.5	0.3
043-2B-1	Thor Vein	cpy	8.4	0.3	056-1-4	Thor Vein	pyr	3.2	0.4
043-2B-2	Thor Vein	cpy	5.4	0.2	056-1-5	Thor Vein	pyr	8.0	0.3
043-2B-3	Thor Vein	cpy	8.8	0.2	056-1-6	Thor Vein	pyr	4.5	0.3
043-2B-4	Thor Vein	cpy	6.7	0.4	056-1-7	Thor Vein	pyr	5.4	0.3
043-2B-5	Thor Vein	cpy	8.9	0.3	056-1-8	Thor Vein	pyr	7.4	0.4
043-2B-6	Thor Vein	cpy	5.3	0.3	056-1-9	Thor Vein	pyr	6.5	0.4
043-2B-7	Thor Vein	cpy	8.2	0.2	056-1-10	Thor Vein	pyr	10.4	0.3
043-2B-8	Thor Vein	cpy	4.7	0.2	056-1-11	Thor Vein	pyr	8.0	0.3
081-2-1	Viking Trend	cpy	6.7	0.3	056-1-12	Thor Vein	pyr	9.5	0.3

APPENDIX F

RADIOGENIC LEAD DATA

Table F.1: Pb isotope data acquired from *in-situ* SIMS analysis of galena from the Viking deposit. Errors given as 2σ (ERR). Average sample Pb compositions are highlighted in grey. Key: Gold mineralized Thor vein = 09MM043, mineralized Thor vein offshoot = 09MM057, and Viking Trend stockwork = 09MM081.

	$^{206}Pb/^{204}Pb$	ERR	$^{207}Pb/^{204}Pb$	ERR	$^{208}Pb/^{204}Pb$	ERR
09MM043-1	18.056	0.094	15.563	0.107	37.638	0.121
09MM043-2	18.110	0.077	15.630	0.095	37.864	0.130
09MM043-3	18.099	0.084	15.631	0.101	37.815	0.124
09MM043-4	18.048	0.091	15.596	0.105	37.764	0.132
09MM043-5	18.109	0.081	15.636	0.108	37.842	0.156
09MM043-6	18.104	0.039	15.626	0.088	37.846	0.119
09MM043-7	18.084	0.053	15.569	0.066	37.564	0.077
09MM043 Ave	18.087	0.074	15.607	0.096	37.762	0.122
09MM057-1	18.012	0.101	15.522	0.132	37.448	0.166
09MM057-2	18.033	0.146	15.563	0.166	37.514	0.194
09MM057-3	18.010	0.106	15.517	0.123	37.436	0.173
09MM057-4	18.048	0.073	15.571	0.109	37.601	0.131
09MM057-5	18.043	0.098	15.562	0.122	37.482	0.208
09MM057-6	18.048	0.146	15.508	0.188	37.418	0.239
09MM057-7	18.049	0.134	15.551	0.177	37.481	0.252
09MM057-1	18.061	0.106	15.633	0.131	37.827	0.151
09MM057-12	18.017	0.086	15.550	0.095	37.580	0.125
09MM057-13	18.031	0.094	15.558	0.120	37.583	0.170
09MM057 Ave	18.035	0.109	15.553	0.136	37.537	0.181
09MM081-1	17.930	0.104	15.502	0.125	37.467	0.154
09MM081-2	17.904	0.058	15.520	0.075	37.553	0.082
09MM081-3	17.931	0.068	15.594	0.101	37.820	0.121
09MM081-4	17.949	0.060	15.591	0.081	37.861	0.120
09MM081-5	17.932	0.065	15.525	0.078	37.527	0.079
09MM081-6	17.892	0.149	15.513	0.165	37.544	0.183
09MM081-7	17.900	0.085	15.526	0.102	37.499	0.139
09MM081 Ave	17.920	0.084	15.539	0.104	37.610	0.125